MERGING BLACK HOLE BINARIES IN GASEOUS ENVIRONMENTS: SIMULATIONS IN GENERAL-RELATIVISTIC MAGNETOHYDRODYNAMICS

BY

BRIAN D. FARRIS

DISSERTATION

Submitted in partial fulfillment of the requirements
for the degree of Doctor of Philosophy in Physics
in the Graduate College of the
University of Illinois at Urbana-Champaign, 2012

Urbana, Illinois

Doctoral Committee:

Professor Charles F. Gammie, Chair
Professor Stuart L. Shapiro, Director of Research
Associate Professor Brian D. Fields
Professor Jon J. Thaler

Abstract

Merging supermassive black hole-black hole (BHBH) binaries produced in galaxy mergers are promising sources of detectable gravitational waves. If such a merger takes place in a gaseous environment, there is a possibility of a simultaneous detection of electromagnetic and gravitational radiation, as the stirring, shock heating and accretion of the gas may produce variability and enhancements in the electromagnetic flux. This can provide a wealth of opportunities to study gravitational physics, accretion physics, and cosmology. We investigate this scenario by performing fully general relativistic, (magneto)hydrodynamic simulations of merging, equal-mass, nonspinning BHBH binaries embedded in gaseous environments. We evolve the metric using the Baumgarte-Shapiro-Shibata-Nakamura (BSSN) formulation with standard moving puncture gauge conditions and handle the magnetohydrodynamics via a high-resolution shock-capturing (HRSC) scheme. In the limit of negligible gas angular momentum, we consider both "binary Bondi accretion" in which the binary is at rest relative to the ambient gas cloud, as well as "binary Bondi-Hoyle-Lyttleton accretion" in which the binary moves relative to the gas cloud. The gas cloud is assumed to be homogeneous far from the binary and governed by a Γ-law equation of state. During the binary inspiral, we find evidence for significant enhancements in both the accretion rate and luminosity over values for a single black hole of the same mass as the binary. We also consider disk-like accretion flows with significant gas angular momentum. In this case, we track the inspiral starting from a binary separation of $10M$, where M is the total binary mass. Disks are allowed to relax in the "early inspiral" epoch to provide quasistationary initial data. We then evolve the spacetime metric and matter during the "late inspiral and merger" epochs. The later simulations are designed to track BHBH inspiral following disk-binary decoupling, through merger and ringdown. Finally, we present results from the first fully general relativistic magnetohydrodynamic (MHD) simulations of an equal-mass BHBH embedded in a magnetized circumbinary accretion disk. Prior to decoupling, we find that the competition between the binary tidal torques and the effective viscous torque due to MHD turbulence depletes the disk interior to the binary orbit but induces a two-stream accretion flow onto the BHs and a mildly relativistic polar outflow. Following decoupling we find that the accretion rate is reduced, while the electromagnetic luminosity peaks near merger due to shock heating.

Acknowledgments

The author would like to thank his advisor, S.L. Shapiro, and colleagues, especially Y.T. Liu, Z. Etienne, V. Paschalidis, R. Gold, and T. Baumgarte, for their invaluable insight, guidance, and hard work. In addition, he would like to thank his family and his wife, Shabnam Javdani, for their encouragement and support. Finally, he thanks H. Pfeiffer for providing his code for generating conformal-thin-sandwich BHBH initial data. This paper was supported in part by NSF Grant PHY-0963136, and NASA grant NNX11AE11G. My personal support has been primarily through a Carver Fellowship and the NASA Earth and Space Science Fellowship (NASA grant NNX09AO64H). This work used the Extreme Science and Engineering Discovery Environment (XSEDE), which is supported by NSF grant number OCI-1053575.

Table of Contents

List of Abbreviations

ADM	Arnowitt-Deser-Misner
AGN	Active Galactiv Nuclei
AH	Apparent Horizon
AMR	Adaptive Mesh Refinement
BH	Black Hole
BHBH	Black Hole-Black Hole binary
BHL	Bondi-Hoyle-Lyttleton
BHNS	Black Hole-Neutron Star binary
BSSN	Baumgarte-Shapiro-Shibata-Nakamura
CTS	Conformal Thin Sandwich
EM	Electro-Magnetic
EOS	Equation of State
GR	General Relativity
GW	Gravitational Wave
HRSC	High-Resolution Shock-Capturing
ISCO	Innermost Stable Circular Orbit
LISA	Laser Interferometer Space Antenna
LSST	Large Synoptic Survey Telescope
MHD	Magneto-Hydro-Dynamics
NASA	National Aeronautics and Space Administration
SMBH	Super-Massive Black Hole
VLDI	Very Long Baseline Interferometry

Chapter 1

Introduction

All bulge galaxies (including the Milky Way) are believed to contain a central supermassive black hole (SMBH) with a mass M between $10^4 M_\odot$ and $10^9 M_\odot$ [1, 2, 3]. It is also believed that galaxy mergers commonly lead to the formation of a massive black hole binary (BHBH) system in the merged remnants [4, 5]. In the standard picture, the BHBH binary separation decreases, first through dynamical friction due to distant stellar encounters, then through gravitational slingshot interactions in which nearby stars are ejected at velocities comparable to the binary's orbital velocity, and finally through the emission of gravitational radiation, leading to coalescence of the binary [6]. These low-frequency gravitational waves will be detectable by LISA-like instruments and will contain a wealth of information about the inspiral. The gaseous accretion flow that forms around the binary can be a source of electromagnetic radiation as well. Following the detection of gravitational waves from a BHBH merger, electromagnetic "afterglow" radiation can provide confirmation of the coalescence [7, 8, 9, 10, 11, 12, 13]. The timescale during which detectable "afterglow" radiation rises to its maximum is governed by viscous diffusion of gas close to the remnant due to turbulent viscosity induced by B-fields. This timescale ranges from several years to hundreds of decades in the case of supermassive BHBH systems.

There also exists the possibility of detecting electromagnetic "precursor" radiation prior to the merger and before the maximum gravitational wave emission [14, 15]. If the merger takes place in a hot gas cloud in which the distant gas is nearly homogeneous and either at rest with respect to the binary ("binary Bondi" accretion) or moving ("binary Bondi-Hoyle-Lyttleton" accretion), then the luminosity will peak at the end of the binary inspiral phase immediately prior to the final plunge [16]. At this stage shock heating of the gas and turbulent magnetic field amplification are strongest. The peak luminosity lasts for $\delta t \sim M_6$ hours prior to merger and then plummets sharply following the coalescence. Here M_6 is the binary mass in units of $10^6 M_\odot$. If, instead, the accretion takes place via a geometrically-thin, optically-thick Keplerian disk around the binary ("binary Shakura-Sunyaev" accretion), there may be a late-time precursor brightening from tidal and viscous (or turbulent magnetic) dissipation in the inner disk. Each of these scenarios raises the exciting possibility of a simultaneous detection of electromagnetic and gravitational waves from a BHBH merger.

This picture is loosely supported by a number of observed AGNs that may be harboring BHBH binaries. Very-long baseline interferometry (VLBI) observations of the elliptical galaxy 0402+379 have discovered two radio sources at a projected separation of only 7 pc. The existence of jets, as well as variability associated with BH activity, indicate that the system may be a BHBH binary [17, 18, 19]. Another candidate is OJ 287, a BL Lac object whose light curve shows variability with a period of ~ 12 yr. It is believed that this may be a massive BHBH binary around which the smaller BH orbits with a period of 12 yr, penetrating the disk of the primary and giving rise to the observed variability [20, 21, 22]. It has been proposed that the quasar SDSS 092712.65+294344 may be either a binary system [23, 24], or a recoiling BH that is the product of a binary merger [25]. Such suggestions are supported by a systematic shift of 2650 km s^{-1} in the emission lines. Another candidate is quasar SDSS J153636.22+044127.0, in which two broad-line emission systems are observed, separated in velocity by 3500 km s^{-1}. This observation has been interpreted as a BHBH binary system in which each object has its own emission system [26]. Recently, the first triple AGN system, SDSS J1027+1749, has been discovered [27]. This galaxy contains three emission-line nuclei corresponding to a supermassive black hole triple with kpc-scale separations.

Information from a simultaneous detection of electromagnetic and gravitational waves may be useful for studying fundamental aspects of gravitational physics. For example, in some modified gravity scenarios, the propagation velocity for gravitons may differ from that of photons [28, 29]. Additionally, the measurement of the luminosity distance from the gravitational wave signal at an accuracy of $1\% - 10\%$, coupled with the redshift information from the electromagnetic detection, could serve as a cosmological "standard siren" of unprecedented accuracy (better than $\sim 1\%$) [30]. Such detections may also combine accurate measurements of BH spins and masses obtained from gravitational wave signals with electromagnetic observations to probe BH accretion physics in great detail [31]. It has even been proposed that simultaneous detections of electromagnetic and gravitational waves may provide a means of witnessing the birth of a quasar [32].

Several mechanisms for electromagnetic emission from accretion disks around merging BHBH binaries have been proposed. In the case of equal mass BHBH binaries, the inner edge of the accretion disk is identified as the radius at which the viscous torque on the gas balances the gravitational torque from binary. This radius is between 1.5 and 2 times the orbital separation [33, 34, 35, 36] and encompasses a hollow region in the disk. Late in the inspiral the BHBH binary decouples from the disk and coalesces. For a binary of mass $M \approx 10^6 M_\odot$ accreting at 10% of the Eddington rate, the subsequent evolution of this disk, which is optically thick, gives rise to a source that initially peaks in the UV band and then hardens to extreme ultraviolet and soft x-ray emission at late times [7, 12, 13]. Additionally, there is a sudden change in the mass of the binary during the final stage of the merger, as gravitational waves carry away a few percent of

the mass. The abrupt change in the potential creates waves in the disk which may grow into shocks and increase the luminosity of the disk in a unique way [10, 11, 37], giving rise to a detectable prompt x-ray signal. Another possibility is that the merged BH remnant may experience a recoil velocity which can, in principle, be as high as several thousand km s^{-1} [38], although it is likely to be much lower (< 200 km/s) in most galaxy mergers [39]. This recoiling BH may "shake" or penetrate the disk, creating shocks which could give rise to a transient signal.

Various methods have been used to model plausible sources of electromagnetic emission from BH mergers. In one approach, the dynamics of the inspiral is ignored, focusing on the effect of BH kicks and/or BH mass loss on the hydrodynamical flow [40, 37, 9, 41, 42, 8, 11, 10, 43]. In another approach, the behavior of the gas is modeled by following the motion of collisionless "particle tracers" on geodesics [44]. Other approaches involve vacuum and/or force-free calculations to investigate the role that magnetic fields may play in producing detectable electromagnetic emission when the density near the binary at merger is very low [45, 46]. Only recently have fully relativistic, hydrodynamical simulations of BHBH binary inspiral and merger in a gaseous environment been performed [16, 47, 48, 49].

Here, we present a study of BHBH binary mergers in the presence of a circumbinary accretion flow. Modeling such systems requires fully general-relativistic dynamical simulations. The development of stable algorithms to integrate Einstein's field equations of general relativity numerically in $3 + 1$ dimensions, such as the Baumgarte-Shapiro-Shibata-Nakamura (BSSN) formalism [50, 51] and the generalized harmonic approach [52, 53, 54], together with the identification of suitable gauge conditions, has enabled several pioneering simulations that demonstrate how to track the late inspiral, plunge and merger of a BHBH binary in vacuum [55, 56, 57]. More refined follow-up simulations of these strong-field, late phases, joined onto analytic, post-Newtonian calculations of the early inspiral epoch [58], are now capable of producing accurate gravitational waveforms for merging BHBH binaries with companions spanning a range of mass ratios and spins (see e.g. [59] and references therein).

With the problem of gravitational wave emission from a vacuum BHBH binary inspiral well in hand, it is now important to turn to the problem of electromagnetic emission from BHBH binary coalescence in an astrophysically realistic gaseous environment.

When gas accretes onto a SMBH in the center of a galaxy the specific angular momentum of the gas $\tilde{L}$ may, in many cases, be much larger than that of a circular orbit near the horizon, $\tilde{L} \sim 2Mc$ [60] leading to a disk-like accretion flow. For this reason, simulations to date have focused on disk-like accretion. However, it has been argued that for *hot* flows, in which the gas is near the galaxy virial temperature, the gas is supported by pressure against free infall and the flow may well be described by the spherical "Bondi" accretion model

[6]. In this so-called "cooling-flow model of quasar fueling", intergalactic gas during the early stages of galaxy formation is accelerated toward the center of dark matter halos and is shock-heated to the virial temperature. This gas accretes then onto the growing SMBH at nearly the Eddington rate. For a $10^6 M_\odot$ BH, the gas is expected to have a density $n \sim 10$ cm^{-3} and temperature $T \sim 10^6$ K $- 10^8$ K [6, 61].

Classical "Bondi accretion" refers to spherically symmetric, steady-state accretion of an adiabatic gas onto a stationary star. The gas is assumed to be homogeneous and at rest far from the star and flow adiabatically with a Γ-law equation of state (EOS). The problem was first studied in Newtonian gravitation for a point mass by Bondi [62], and later extended to accretion onto a BH in full general-relativity [63, 64, 65]. Accretion onto a star moving with constant velocity through a cloud which is asymptotically uniform and at rest was first studied qualitatively in Newtonian gravity by Hoyle and Lyttleton [66] and later extended by Bondi and Hoyle [67]. The general-relativistic version for accretion onto a single BH has been studied via numerical simulations [68, 69, 70, 71]. We refer to this scenario as the "Bondi-Hoyle-Lyttleton accretion" (BHL) problem.

We probe the *hot* flow limit by assuming zero net angular momentum and restricting our attention to simulations in which the binary is placed in a gas cloud which has constant density and temperature at infinity. As in the classic Bondi and Bondi-Hoyle-Lyttleton accretion problems, we assume that the mass of the cloud is small compared to the mass of the binaries. We treat two cases: one in which the gas is asymptotically at rest (binary Bondi accretion), the other where the gas is moving with constant velocity with respect to the BHBH center of mass (binary BHL accretion). Bondi and BHL accretion onto single BHs represent classic problems which are well understood. We seek to use this understanding as a foundation for tackling the problem of accretion onto a merging BHBH binary. The initial conditions of the gas during the merger of two supermassive BHs in realistic astrophysical environments is still an open question and subject to uncertainties in cosmological structure and galaxy formation scenarios, and in our understanding of the formation history and role of massive BHs in this process. The binary Bondi and BHL problems provide excellent settings in which to begin a rigorous probe of the binary accretion problem.

We also extend this work by considering disk-like binary accretion as well. Disk accretion onto a BHBH binary has been studied previously in the Newtonian, geometrically thin-disk limit, both analytically [72, 73, 14, 12, 15, 74] and numerically [8, 10, 11, 36]. We extend this work first by performing fully relativistic hydrodynamcal simulations in 3+1 dimensions. We restrict our attention to a circumbinary disk residing in the orbital plane of two nonspinning, equal-mass, binary black holes. The black holes are initially in a quasistationary, nearly circular orbit and represent a solution to the conformal thin-sandwich (CTS) initial-value equations (see, e.g. [75, 76, 77] and references therein). The mass of the disk is assumed to be small

in comparison to the total black hole mass. Initially, we explore the response of the disk to the binary on a *dynamical* timescale and thus ignore the secular motion of gas in the disk due to viscosity or turbulent magnetic fields. We treat the gas as a perfect fluid described by a Γ-law equation of state (EOS) and handle shocks by high-resolution, shock-capturing (HRSC) techniques. We study the response of the disk to tidal torques during the early and late inspiral phases, as well as during the merger and post-merger epochs. The inspiral and merger are followed by solving the BSSN field equations [50, 51] with moving puncture gauge conditions [57, 56]. We are particularly interested in the evolution of the hollow region in the disk about the binary [33, 34, 35, 36] and the extent to which gas penetrates the hollow and accretes onto the black holes. We also estimate, as a perturbation, the electromagnetic emission from the disk that characterizes the inspiral and merger epochs. Our treatment in this regime is appropriate for describing the epoch following disk-binary "decoupling," when the BHBH inspiral timescale is much shorter than the viscous timescale in the disk, whereby viscosity-induced inflow can be neglected. Our analysis remains valid throughout the binary merger and ringdown phases, but is no longer adequate to describe the late-time evolution when viscosity serves to drive gas into the hollow and accrete onto the merged remnant [7, 12].

In the pre-decoupling phase, the gravitational wave inspiral timescale is long compared to the viscous timescale, and BHBH inspiral due to gravitational radiation can be ignored. During this phase, a balance is achieved between binary torques, which add angular momentum to the gas and drive matter outward, and viscous torques which transport angular momentum outward, allowing gas to migrate inward. The radius at which these torques balance determines the inner edge of the circumbinary accretion disk [7] for equal mass BHBH binaries. While Newtonian analytic calculations have been carried out to determine equilibrium solutions [33, 74, 78, 79], they are limited by their simplified treatment of binary torques, viscosity, and restriction to thin disks and unequal mass ratios. A realistic treatment of the problem requires a fully general-relativistic magnetohydrodynamic (GRMHD) simulation in 3D, in which an effective viscosity arises naturally through MHD turbulence triggered by the magnetorotational instability (MRI) [80]. Here we report the first fully GRMHD simulation of a magnetized, circumbinary BHBH accretion disk. The effective viscosity competes with the tidal torques exerted by the binary, so that a quasi-stationary state is reached prior to binary-disk decoupling [7, 74]. This state has been simulated both in Newtonian [7] and in Post-Newtonian [81] gravitation. Typically, the computational domain excludes the region near the BHs and artificial inner boundary conditions are imposed. Recent Newtonian studies [82] make clear the importance of imposing the correct boundary conditions on the flow inside the central disk hollow and near the BHs, further motivating a treatment in full, dynamical GR whereby BH horizons can be modeled reliably.

The basic evolution of the system is as follows: For large binary separations a, the inspiral time due to GW

emission is much longer than the viscous time ($t_{\rm GW} \gtrsim t_{\rm vis}$), so that the disk settles into a quasi-stationary state. For equal-mass BHs, the binary tidal torques carve out a partial hollow in the disk [33, 7, 36, 78] of radius $\sim 2a$ and excite spiral density waves throughout the disk, that dissipate and heat the gas. However, gas can penetrate the hollow in response to the time-varying tidal torque [36, 83, 78, 81]. At sufficiently small separations $t_{\rm GW} \lesssim t_{\rm vis}$, and the BHBH *decouples* from the disk. The disk structure at decoupling crucially determines its subsequent evolution and the EM emission. GW emission close to merger leads to mass loss [11, 10] and may induce remnant BH recoil [40], which give rise to further characteristic EM signatures. Here we simulate the system in two different epochs: (I) The pre-decoupling phase ($t_{\rm GW} > t_{\rm vis}$) and (II) the post-decoupling phase ($t_{\rm GW} < t_{\rm vis}$), including the inspiral and merger of the BHBH. We consider equal-mass, nonspinning binaries. While the BH mass scales out, we are primarily interested in total (ADM) masses $M \gtrsim 10^6 M_\odot$ and low density disks for which the tidally-induced binary inspiral and the disk self-gravity are negligible. This investigation, though preliminary, previews more detailed GRMHD simulations we plan to perform in anticipation of future, simultaneous detections of gravitational and electromagnetic radiation from a merging BHBH-disk system.

Chapter 2

Metric Evolution Equations

2.1 3+1 decomposition of Einstein's equations

In the standard formulation of general relativity, space and time are unified into 4-dimensional spacetime. The curvature of spacetime can be quantified with the 4-dimensional Riemann curvature tensor

$$ {}^{(4)}R^{\alpha}{}_{\beta\gamma\delta} = {}^{(4)}\Gamma^{\alpha}{}_{\beta\delta,\gamma} - {}^{(4)}\Gamma^{\alpha}{}_{\beta\gamma,\delta} + {}^{(4)}\Gamma^{\alpha}{}_{\mu\gamma}{}^{(4)}\Gamma^{\mu}{}_{\beta\delta} - {}^{(4)}\Gamma^{\alpha}{}_{\mu\delta}{}^{(4)}\Gamma^{\mu}{}_{\beta\gamma} \ , \tag{2.1} $$

where we have defined the 4-dimensional connection coefficient

$$ {}^{(4)}\Gamma^{\mu}{}_{\nu\lambda} = \frac{1}{2} g^{\mu\kappa}(g_{\kappa\nu,\lambda} + g_{\kappa\lambda,\nu} - g_{\nu\lambda,\kappa}) \ . \tag{2.2} $$

Here $g^{\mu\nu}$ is the metric which appears in the spacetime line element

$$ ds^2 = g_{\mu\nu} dx^{\mu} dx^{\nu} \ . \tag{2.3} $$

The influence of matter on the curvature of spacetime, and the motion of matter through curved spacetime, are elegantly described by Einstein's field equations

$$ {}^{(4)}G^{\mu\nu} \equiv {}^{(4)}R^{\mu\nu} - \frac{1}{2} g^{\mu\nu}{}^{(4)}R = 8\pi T^{\mu\nu}. \tag{2.4} $$

where $R_{\mu\nu} \equiv R^{\rho}{}_{\mu\rho\nu}$ is the Ricci curvature tensor, $R \equiv R^{\mu}{}_{\mu}$ is the Ricci curvature scalar, and $T^{\mu\nu}$ is the stress-energy tensor.

While the form of Einstein's equation given in Eq. (2.4) has aesthetic appeal, we must break the unification of space and time if we are to recast the equations into an initial value formulation amenable to numerical simulations. The Arnowitt-Deser-Misner formalism (ADM) provides a suitable starting point [84]. In the ADM formalism, the spacetime is foliated into a sequence of 3-dimensional spatial hypersurfaces. Initial data

may be defined on an initial hypersurface, and evolved to subsequent hypersurfaces according to Einstein's equations. The spacetime line element is written as

$$ds^2 = g_{\mu\nu}dx^\mu dx^\nu = -\alpha^2 dt^2 + \gamma_{ij}(dx^i + \beta^i)(dx^i + \beta^i) \ , \tag{2.5}$$

where the lapse function α specifies the amount of proper time which elapses between neighboring hypersurfaces, the shift β^i describes the relabeling of spatial coordinates from one hypersurface to the next, and the spatial metric γ_{ij} describes the spatial geometry of each slice.

The lapse and shift are gauge quantities which reflect the four degrees of coordinate freedom in Einstein's Equations. Once these quantities have been specified, the unit normal 4-vector to the spatial hypersurface is given by $n^\mu = (\alpha^{-1}, -\alpha^{-1}\beta^i)$. The spatial metric is the projetion of the 4-metric onto the spatial hypersurface, and is given by

$$\gamma_{\mu\nu} = g_{\mu\nu} + n_\mu n_\nu \ . \tag{2.6}$$

It is straightforward to compute the Riemann tensor associated with the 3D metric. We simply replace $g_{\mu\nu}$ with $\gamma_{\mu\nu}$ in Eq. (2.1) and Eq. (2.2). However, this object only contains information about the *intrinsic* curvature of the hypersurface. The remaining information is contained in the *extrinsic* curvature tensor

$$K_{\mu\nu} = -\frac{1}{2}\mathcal{L}_{\mathbf{n}}\gamma_{\mu\nu} \ , \tag{2.7}$$

where $\mathcal{L}_n$ is the Lie derivative of along n^μ, and can be though of as a "time derivative".

2.2 Constraint Equations

If we project Einsten's equation twice along the normal direction, we find

$${}^{(4)}R^{\mu\nu}n_\mu n_\nu + \frac{1}{2}{}^{(4)}R = 8\pi T^{\mu\nu}n_\mu n_\nu \equiv 8\pi\rho_S \ , \tag{2.8}$$

while one normal projection and one spatial projection gives

$${}^{(4)}R^{\mu\nu}\gamma_{i\mu}n_\nu = 8\pi T^{\mu\nu}\gamma_{i\mu}n_\nu \equiv 8\pi S_i \ . \tag{2.9}$$

Here, $\rho_S \equiv n_\mu n_\nu T^{\mu\nu}$ and $S_i \equiv \gamma_{i\mu}n_\nu T^{\mu\nu}$. Using Gauss' equation, the Codazzi equation, and the Ricci equation, each of which may be derived by taking spatial and normal projections of the 4D Riemann tensor

(see [77]), we may rewrite Eqns. (2.8) and (2.9) as

$$R + K^2 - K_{ij}K^{ij} = 16\pi\rho_S \ , \tag{2.10}$$

and

$$D_i K - D_j K^j{}_i = 8\pi S_i \ . \tag{2.11}$$

These are known as the Hamiltonian constraint and the momentum constraint, respectively, and they must be satisfied on each spatial hypersurface.

2.3 Evolution equations

By expanding the Lie derivative in definition of the extrinsic curvature in Eq. (2.7) in terms of covariant and partial derivatives, we may derive an evolution equation for the spatial metric γ_{ij}.

$$\partial_t \gamma_{ij} = -2\alpha K_{ij} + D_i\beta_j + D_j\beta_i \tag{2.12}$$

We may also combine Einstein's equations with Gauss's equation and the Ricci equation to derive an evolution equation for K_{ij} (See [77] for details).

$$\partial_t K_{ij} = -D_i D_j \alpha + \alpha(R_{ij} - 2K_{ik}K^k_{\ j} + KK_{ij}) - 8\pi\alpha\left[S_{ij} - \frac{1}{2}\gamma_{ij}(S - \rho_S)\right] + \mathcal{L}_\beta K_{ij} \ . \tag{2.13}$$

Here $S_{ij} \equiv \gamma^\alpha{}_i \gamma^\beta{}_j T_{\alpha\beta}$ and $S \equiv S^i{}_i$.

2.4 The Baumgarte-Shapiro-Shibata-Nakamura (BSSN) formalism

While the ADM formulation successfully recasts Einstein's equations into the 3+1 form needed for numerical simulations, it suffers from numerical instabilities. Small deviations from the constraint surfaces grow exponentially, rapidly spoiling the solution. A modification known as the BSSN formulation has been developed in order to avoid such numerical instabilities. Here we outline the BSSN formulation, following [51, 50]. We begin by defining the conformal exponent

$$\phi = \frac{1}{12}\log(\det(\gamma_{ij})) \ . \tag{2.14}$$

Next we use ϕ to define the conformal metric and the conformal, traceless extrinsic curvature

$$\tilde{\gamma}_{ij} = e^{-4\phi}\gamma_{ij}, \tag{2.15}$$

$$\tilde{A}_{ij} = e^{-4\phi}\left(K_{ij} - \frac{1}{3}\gamma_{ij}K\right), \tag{2.16}$$

where $K \equiv \gamma^{ij}K_{ij}$ is the trace of the extrinsic curvature. With these definitions, Eq. (2.12) splits into two evolution equations for ϕ and $\tilde{\gamma}_{ij}$,

$$(\partial_t - \mathcal{L}_\beta)\tilde{\gamma}_{ij} = -2\alpha\tilde{A}_{ij}, \tag{2.17}$$

$$(\partial_t - \mathcal{L}_\beta)\phi = -\frac{1}{6}\alpha K, \tag{2.18}$$

and Eq. (2.13) splits into two evolution equations for K and $\tilde{A}_{ij}$,

$$\begin{aligned}(\partial_t - \mathcal{L}_\beta)K &= -\gamma^{ij}D_jD_i\alpha + \frac{1}{3}\alpha K^2 + \alpha\tilde{A}_{ij}\tilde{A}^{ij} + 4\pi\alpha(\rho + S),\\ (\partial_t - \mathcal{L}_\beta)\tilde{A}_{ij} &= e^{-4\phi}(-D_iD_j\alpha + \alpha(R_{ij} - 8\pi S_{ij}))^{TF} + \alpha(K\tilde{A}_{ij} - 2\tilde{A}_{il}\tilde{A}^l{}_j).\end{aligned}$$

The Ricci tensor can be decomposed into a conformal part $\tilde{R}_{ij}$, which depends only on the conformal metric and it's derivatives, and it's remainder R^ϕ_{ij}. We also introduce a new evolution variable

$$\tilde{\Gamma}^i \equiv \tilde{\gamma}^{ij}\tilde{\Gamma}^i{}_{jk} = -\tilde{\gamma}^{ij}{}_{,j}. \tag{2.19}$$

With this defnition, $\tilde{R}_{ij}$ can be expressed as

$$\tilde{R}_{ij} = -\frac{1}{2}\tilde{\gamma}^{kl}\tilde{\gamma}_{ij,kl} + \tilde{\gamma}_{k(i}\partial_{j)}\tilde{\Gamma}^k + \tilde{\Gamma}^k\tilde{\Gamma}_{(ij)k} + \tilde{\gamma}^{lm}\left(2\tilde{\Gamma}^k_{l(i}\tilde{\Gamma}_{j)km} + \tilde{\Gamma}^k_{im}\tilde{\Gamma}_{klj}\right) . \tag{2.20}$$

Note that because $\tilde{\Gamma}^i$ is an evolution variable, the only second derivatives of $\tilde{\gamma}_{ij}$ appear in the first term of Eq. (2.20), which is a laplacian. Thus, Eq. (2.17) and Eq. (2.19), taken together, act as an inhomogenous wave equation for $\tilde{\gamma}_{ij}$. This feature improves the hyperbolicity of the evolution equations and may be largely responsible for the stability of the BSSN formulation. An evolution equation for $\tilde{\Gamma}^i$ may be derived by taking

a time derivative of Eq. (2.19) and substituting the momentum constraint in Eq. (2.11),

$$\begin{aligned}\partial_t \tilde{\Gamma}^i &= \partial_j(2\alpha\tilde{A}^{ij} + \mathcal{L}_\beta \tilde{\gamma}^{ij}) \\ &= \tilde{\gamma}^{jk}\beta^i{}_{,jk} + \frac{1}{3}\tilde{\gamma}^{ij}\beta^k{}_{,kj} - \tilde{\Gamma}^j\beta^i{}_{,j} + \frac{2}{3}\tilde{\Gamma}^i\beta^j{}_{,j} + \beta^j\tilde{\Gamma}^i{}_{,j} - 2\tilde{A}^{ij}\partial_j\alpha \\ &\quad -2\alpha\left(\frac{2}{3}\tilde{\gamma}^{ij}K_{,j} - 6\tilde{A}^{ij}\phi_{,j} - \tilde{\Gamma}^i{}_{jk}\tilde{A}^{jk} + 8\pi\tilde{\gamma}^{ij}S_j\right).\end{aligned}$$

Finally, we rewrite the constrint equations (2.10) and (2.11) in terms of BSSN variables,

$$0 = \mathcal{H} = \tilde{\gamma}^{ij}\tilde{D}_i\tilde{D}_j e^\phi - \frac{e^\phi}{8}\tilde{R} + \frac{e^{5\phi}}{12}\tilde{A}^{ij}\tilde{A}_{ij} + \frac{e^{5\phi}}{12}K^2 + 2\pi e^{5\phi}\rho, \tag{2.21}$$

$$0 = \mathcal{M}^i = \tilde{D}_j(e^{6\phi}\tilde{A}^{ji}) - \frac{2}{3}e^{6\phi}\tilde{D}^i K - 8\pi e^{6\phi}S^i. \tag{2.22}$$

2.5 Gauge evolution

In principle, we are free to specify any lapse α and shift β^i that we like, reflecting the coordinate freedom inherent in Einstein's equations. In practice, however, finding gauge conditions which can avoid numerically unstable singularities has proven difficult. Fortunately, more sophisticated gauge conditions have been discovered which can avoid such singularities. We choose the standard moving puncture gauge conditions, which include the "1+log" slicing condition for the lapse, and the "Gamma-freezing" condition for the shift [85],

$$\partial_0\alpha = -2\alpha K\ , \tag{2.23}$$

$$\partial_0\beta^i = (3/4)B^i\ , \tag{2.24}$$

$$\partial_0 B^i = \partial_0\tilde{\Gamma}^i - \eta B^i\ , \tag{2.25}$$

where $\partial_0 \equiv \partial_t - \beta^j\partial_j$.

2.6 Treatment of spacetime with helical Killing vector

When simulating BHBH spacetimes, there are many cases of interest for which the binary separation a is sufficiently large so that the inspiral time scale is much longer than the orbital time scale. This fact can be exploited by neglecting the change in binary separation and employing a metric that is quasistationary in

the rotating frame of the binary. This simplification provides an accurate solution for the spacetime without the computational expense of a full evolution of Einstein's field equations.

In order to use this method, we must choose a coordinate system in which the metric explicitly reflects the symmetry of the spacetime. This symmetry, describing a spacetime that is quasistationary in a frame that rotates with the orbital frequency of the binary Ω, can be constructed by employing a helical Killing vector,

$$\xi \equiv \partial_t + \Omega \partial_\phi. \tag{2.26}$$

For a spacetime admitting such a Killing vector, we have

$$\mathcal{L}_\xi g_{\mu\nu} = 0 \ , \tag{2.27}$$

where $\mathcal{L}$ is the Lie derviative, and $g_{\mu\nu}$ is the spacetime metric.

Provided we are working in an appropriate coordinate system (i.e. one employing Killing coordinates t and ϕ), we may express the metric at any point in spacetime in terms of the metric on an initial $t = 0$ slice according to

$$g_{\mu\nu}(t, r, \theta, \phi) \doteq g_{\mu\nu}(0, r, \theta, \phi - \Omega t) \tag{2.28}$$

where the symbol $\doteq$ denotes that the equality holds only in a particular coordinate system. One can easily verify that the above equation satisfies Killing's equation (2.27).

We note that Eq. (2.28) is written in spherical polar coordinates, i.e. $\{x^\alpha\} = \{t, r, \theta, \phi\}$. However, Cartesian coordinates are more suitable for work in 3D, as coordinate singularities at $r = 0$ and on the polar axis are avoided. We therefore transform the spherical components of $g_{\mu\nu}$ back to the Cartesian components using the usual tensor transformation formula.

BHBH evolution employing standard puncture initial data and moving puncture gauge conditions does not result in a metric that satisfies Eq (2.27) (Puncture initial data does not implement a helical Killing vector). By contrast, BHBH conformal-thin-sandwich (CTS) initial data (see, e.g. [76]) are specifically constructed to satisfy this equation: CTS initial data impose the condition that the spacetime in the rotating frame is stationary (see [77] for discussion and references). This condition is valid, approximately, whenever the binary companions are sufficiently well separated that the inspiral time scale is much longer than the orbital time scale. In this quasistationary early inspiral regime we can employ CTS initial data and CTS lapse and shift functions to evolve the metric via a simple coordinate rotation in lieu of integrating the Einstein field equations. We can then evolve the disk by integrating the hydrodynamic equations for the

fluid in this background spacetime.

CTS initial data contains excised interiors. We follow the technique outlined in [86] and fill the excised region inside the BH interiors with smoothly extrapolated "junk" (i.e., constraint-violating) data. This treatment is valid because the interior regions are causally disconnected from the exterior spacetime.

Chapter 3

GRMHD Formalism

3.1 Evolution of large-scale electromagnetic fields

In the ideal MHD limit, in which the fluid is a perfect conductor, Ohm's law yields the MHD condition $F^{\mu\nu}u_\nu = 0$. This condition is equivalent to the statement that the electric field in the fluid's rest frame vanishes. The evolution equation for the electromagnetic field can be obtained in conservative form by taking the dual of Maxwell's equation $F_{[\mu\nu,\lambda]} = 0$. One finds

$$\nabla_\nu {}^*F^{\mu\nu} = \frac{1}{\alpha\sqrt{\gamma}}\partial_\nu \left(\alpha\sqrt{\gamma}\ {}^*F^{\mu\nu}\right) = 0 \ , \tag{3.1}$$

where $F^{\alpha\beta}$ is the Faraday tensor, and ${}^*F^{\alpha\beta} = \epsilon^{\alpha\beta\mu\nu}F_{\mu\nu}/2$ is its dual. Using the fact that the magnetic field as measured by a normal observer n^α is given by $B^i = n_\mu {}^*F^{\mu i}$, the time component of Eq. (3.1) gives the no-monopole constraint $\partial_j \tilde{B}^j = 0$, where $\tilde{B}^j = \sqrt{\gamma}\, B^j$. The spatial components of Eq. (3.1) give the magnetic induction equation, which can be written as

$$\partial_t \tilde{B}^i + \partial_j \left(v^j \tilde{B}^i - v^i \tilde{B}^j\right) = 0 \ , \tag{3.2}$$

where $v^i \equiv u^i/u^0$.

One of the biggest challenges in solving the MHD equations numerically is ensuring that the no-monopole constraint ($\nabla \cdot \mathbf{B} = 0$) is satisfied. In general, small errors in the evolution of the induction equation lead to unphysical violations of this constraint. With uniformly-spaced grids, constrained transport (CT) schemes are effective in eliminating violations to machine precision [87]. For AMR grids, hyperbolic divergence-cleaning methods have been employed (see e.g. [88]), but these do not preserve the constraint to machine precision and have proven to be difficult to use in the presence of black holes.

In this work, we adopt a scheme in which we recast the induction equation as an evolution equation for the electromagnetic 4-vector potential $\mathcal{A}_\mu = \Phi n_\mu + A_\mu$, with $n^\mu A_\mu = 0$. Under this definition, the constraint

and induction equations become

$$B^i = \epsilon^{ijk}\partial_j A_k \tag{3.3}$$

$$\partial_t A_i = \epsilon_{ijk} v^j B^k - \partial_i(\alpha\Phi - \beta^j A_i) \tag{3.4}$$

The no-monopole constraint is satisfied automatically in this formulation because the divergence of a curl is always equal to 0. Moreover, this scheme need not be modified in order to work with non-uniform AMR grids.

When choosing $\mathcal{A}_\mu$ as our dynamical variable, we intruduce a new gauge degree of freedom. This requires us to make an EM gauge choice in order to close the system of equations. For this work, we choose the modified Lorenz gauge,

$$\nabla_\mu \mathcal{A}^\mu = \xi n_\mu \mathcal{A}^\mu \ . \tag{3.5}$$

where we choose $\xi = 4/M$. Here, we have added a source term to the right-hand-side of the usual Lorenz gauge equation in order to damp spurious gauge modes. We find that this leads to a significant improvement in the stability of our evolutions. Rewriting Eq. (3.5) as an evolution equation for Φ, we find,

$$\partial_t \Phi = \beta^i \partial_i \Phi - \alpha \partial_i A^i + \gamma^{-1/2}\Phi\partial_i(\sqrt{\gamma}\beta^i) - \gamma^{-1/2}A^i\partial_i(\alpha\sqrt{\gamma}) - \Phi\partial_t \ln(\sqrt{\gamma}) - \alpha\xi\Phi \ . \tag{3.6}$$

3.2 Evolution of the MHD field

In the MHD limit, $T^{\mu\nu}_{(\mathrm{em})}$ can be expressed as

$$T^{\mu\nu}_{(\mathrm{em})} = b^2 u^\mu u^\nu + \frac{1}{2} b^2 g^{\mu\nu} - b^\mu b^\nu \ , \tag{3.7}$$

where $b^\mu = B^\mu_{(u)}/\sqrt{4\pi}$ and where

$$B^\mu_{(u)} = u_\nu {}^*F^{\nu\mu} = -\frac{h^\mu{}_\nu B^\nu}{n_\nu u^\nu} \tag{3.8}$$

is the magnetic field measured by an observer comoving with the fluid. The stress-energy tensor associated with the perfect fluid can be expressed as

$$T^{\mu\nu}_{(\mathrm{hydro})} = \rho_0 h u^\mu u^\nu + P g^{\mu\nu} \ , \tag{3.9}$$

where ρ_0 is the (baryon) rest-mass density, P is matter pressure, $h = 1 + \epsilon + P/\rho_0$ is the specific enthalpy, and ϵ is the specific internal energy density of the matter. For brevity, we denote

$$T^{\alpha\beta}_{(\mathrm{mhd})} = T^{\alpha\beta}_{(\mathrm{hydro})} + T^{\alpha\beta}_{(\mathrm{em})} \ . \tag{3.10}$$

Thus, we see that the conservation of the total stress-energy tensor can be written as

$$T^{\alpha\beta}_{(\mathrm{mhd});\beta} = ((\rho_0 h + b^2)u^\mu u^\nu + (P + \frac{1}{2}b^2)g^{\mu\nu} - b^\mu b^\nu)_{;\beta} = 0 \tag{3.11}$$

Additionally, we have the continuity equation expressing baryon number conservation,

$$(\rho_0 u^\nu)_{;\nu} = 0 \ . \tag{3.12}$$

Rewriting Eqs. (3.11) and (3.12) in conservative form gives (cf. Section IIC in [89])

$$\partial_t \rho_* + \partial_j(\rho_* v^j) = 0 \ , \tag{3.13}$$

$$\partial_t \tilde{S}_i + \partial_j(\alpha\sqrt{\gamma} T^j_{(\mathrm{mhd})i}) = \frac{1}{2}\alpha\sqrt{\gamma}\, T^{\alpha\beta}_{(\mathrm{mhd})} g_{\alpha\beta,i} \ , \tag{3.14}$$

$$\partial_t \tilde{\tau} + \partial_i(\alpha^2\sqrt{\gamma} T^{0i}_{(\mathrm{mhd})} - \rho_* v^i) = s \ , \tag{3.15}$$

where the MHD evolution variables are

$$\rho_* = \alpha\sqrt{\gamma}\,\rho_0 u^0 \ , \tag{3.16}$$

$$\begin{aligned} \tilde{S}_i &= \sqrt{\gamma}\, n_\mu T^\mu_{(\mathrm{mhd})i} \\ &= \alpha\sqrt{\gamma}\, T^0_{(\mathrm{mhd})i} \\ &= (\rho_* h + \alpha u^0\sqrt{\gamma} b^2)u_i - \alpha\sqrt{\gamma} b^0 b_i \ , \end{aligned} \tag{3.17}$$

$$\begin{aligned} \tilde{\tau} &= \sqrt{\gamma}\, n_\mu n_\nu T^{\mu\nu}_{(\mathrm{mhd})} - \rho_* \\ &= \alpha^2\sqrt{\gamma}\, T^{00}_{(\mathrm{mhd})} - \rho_* \ , \end{aligned} \tag{3.18}$$

and the source term s is

$$\begin{aligned} s &= -\alpha\sqrt{\gamma}\, T^{\mu\nu}_{(\mathrm{mhd})} \nabla_\nu n_\mu \\ &= \alpha\sqrt{\gamma}\,[(T^{00}_{(\mathrm{mhd})}\beta^i\beta^j + 2T^{0i}_{(\mathrm{mhd})}\beta^j + T^{ij}_{(\mathrm{mhd})})K_{ij} - (T^{00}_{(\mathrm{mhd})}\beta^i + T^{0i}_{(\mathrm{mhd})})\partial_i\alpha] \ . \end{aligned} \tag{3.19}$$

Note that these evolution variables are very similar to those in [89].

To complete the system of equations, it remains only to specify the equation of state (EOS) of the fluid. In this paper, we adopt a Γ-law EOS,

$$P = (\Gamma - 1)\rho_0\epsilon, \tag{3.20}$$

where Γ is the adiabatic gas constant. We choose a Γ-law EOS because it simplifies some of the calculations, it is applicable to many cases of interest, and it is a standard choice for demonstrating new computational techniques in the numerical relativity literature. Also, the analytic solutions we are going to use as code tests also use this EOS. Nevertheless, all evolution equations derived in this section apply for any equation of state, and generalization to a more realistic EOS is straightforward. In fact, our code is currently capable of handling the general class of EOSs of the form $P = P(\rho_0, \epsilon)$.

3.3 Summary of equations

To reiterate, the system of coupled Einstein-radiation-Maxwell-MHD equations we consider are the BSSN equations (2.17)–(2.21), the magnetic induction equation (3.4), the magnetic gauge evolution equation (3.6), and the MHD equations (3.13)–(3.15). The evolution variables are ϕ, $\tilde{\gamma}_{ij}$, K, $\tilde{A}_{ij}$, $\tilde{\Gamma}^i$, $\bar{\tau}$, $\bar{S}_i$, A^i, Φ, ρ_*, $\tilde{S}_i$ and $\tilde{\tau}$. These variables are not completely independent: the BSSN variables ϕ, $\tilde{\gamma}_{ij}$, K, $\tilde{A}_{ij}$, and $\tilde{\Gamma}^i$ have to satisfy the Hamiltonian constraint (2.21) and the momentum constraint (2.22).

The total stress-energy tensor $T^{\mu\nu}$ is given by

$$\begin{aligned} T^{\mu\nu} &= T^{\mu\nu}_{(\text{hydro})} + T^{\mu\nu}_{(\text{em})} & (3.21)\\ &= \left(\rho_0 h + b^2\right) u^\mu u^\nu + \left(P + \frac{1}{2}b^2\right) g^{\mu\nu} - b^\mu b^\nu \ . & (3.22) \end{aligned}$$

The BSSN matter-energy source terms can be expressed as

$$\begin{aligned} \rho &= (\alpha u^0)^2 \left(\rho_0 h + b^2\right) - \left(P + \frac{1}{2}b^2\right) - (\alpha b^0)^2 & (3.23)\\ S_i &= \alpha u_0 \left(\rho_0 h + b^2\right) u_i - \alpha b^0 b_i & (3.24)\\ S_{ij} &= \left(\rho_0 h + b^2\right) u_i u_j + \left(P + \frac{1}{2}b^2\right) \gamma_{ij} - b_i b_j \ . & (3.25) \end{aligned}$$

Chapter 4

Numerical Methods

4.1 Bondi initial data

For each binary-Bondi simulation discussed in this thesis, we consider the gas to be adiabatic (apart from shocks) with uniform density and pressure at infinity. We take the gas either be asymptotically at rest (binary Bondi accretion), or moving uniformly (binary BHL accretion). We use the `TWOPUNCTURES` code [90] to construct the initial data for the binary BHBH metric. We choose the bare mass and momentum of the punctures according to [91] in order to ensure that the BHBH binary orbit is initially close to quasicircular.

We restrict our analysis to equal-mass, nonspinning BHs in this thesis. However, we note that upon merger, the remnant settles down to a spinning black hole with ADM mass $M_f = 0.95M$. Here M_f denotes the final ADM mass, while M denotes the initial ADM mass of the binary. We also measure a final spin parameter $J_f/M_f^2 = 0.69$, in good agreement with the estimate of [92]. For this case, there is no recoil velocity.

For all of our binary-Bondi runs we use the analytic relativistic Bondi solution for accretion onto a stationary Schwarzschild BH as initial data. This solution is reviewed in Sec. 5.1. To implement this data, we treat the binary as a single gravitating object of mass M, where M is the ADM mass of the binary, and apply the analytic Bondi solution. The fluid pressure is set according to a polytropic EOS, $P = K\rho_0^\Gamma$, with $K = P_\infty/\rho_{0,\infty}^\Gamma$, where $\rho_{0,\infty}$ and P_∞ are the rest-mass density and pressure at infinity, respectively.

4.2 Disk initial data

For our disk initial data, we use the equilibrium solution for a stationary disk around a *single* Kerr BH derived by Chakrabarti *et al.* [93] and summarized in [94]. We take this disk as inital data for a binary BHBH, placing the inner boundary of the disk well outside the BHBH orbital radius. Though no longer stationary, the initial disk settles down to quasistationary equilibrium as the binary rotates, apart from low amplitude spiral density waves induced by the time-varying tidal torque. For completeness, we provide a

brief summary of the construction of disk initial data in Appendix A.

For our fiducial equation of state, $\Gamma = 5/3$, the resulting outer disk radius is $R_{out} \approx 65M$ and the disk scale height at R_{disk} is $H/R = 0.11$ (see Table 6.4 for more details). Here H is defined as the height above the equatorial plane where the pressure falls to $1/e$ its value on the equatorial plane at the radius of maximum pressure. For binary BHs, the disk is approximately stationary if $R_{in} \gg d$, where d is the binary separation and R_{in} is the inner edge of the disk. Initially, we take $R_{in}/d = 1.5$. We find that the disk relaxes to a near quasistationary state after a time $\sim 4t_{disk}$.

4.3 Evolution of metric and matter

We evolve the BSSN field equations with fourth-order accurate, centered, finite-difference stencils, except on shift advection terms, where we use fourth-order accurate upwind stencils. We apply Sommerfeld outgoing wave boundary conditions to all BSSN fields. Our code is embedded in the Cactus parallelization framework [95], and our fourth-order Runge-Kutta time-stepping is managed by the `MoL` (Method of Lines) thorn, with a Courant-Friedrichs-Lewy factor set to 0.5 in all BHBH simulations. We use the Carpet [96] infrastructure to implement the moving-box AMR. In all AMR simulations presented here, we use second-order temporal prolongation, coupled with fifth-order spatial prolongation. The apparent horizon of the BH is computed with the `AHFinderDirect` Cactus thorn [97].

We write the general-relativistic hydrodynamics equations in conservative form. They are evolved by an HRSC technique [89] that employs the piecewise parabolic (PPM) reconstruction scheme [98] coupled to the Harten, Lax, and van Leer (HLL) approximate Riemann solver [99]. The adopted hydrodynamic scheme is second-order accurate for smooth flows, and first-order accurate when discontinuities (e.g. shocks) arise. Throughout the evolution, we impose limits on the pressure to prevent spurious heating and negative values of the internal energy ϵ. Specifically, we require $P_{\rm min} \leq P \leq P_{\rm max}$ inside the horizon, where $P_{\rm max} = 10K\rho_0^\Gamma$ and $P_{\rm min} = K\rho_0^\Gamma/2$. Whenever P exceeds $P_{\rm max}$ or drops below $P_{\rm min}$, we reset P to $P_{\rm max}$ or $P_{\rm min}$, respectively. We check that this fix is applied only inside the apparent horizon, which is causally disconnected from the rest of the grid.

At each timestep, we need to recover the "primitive variables" ρ_0, P, and v^i from the "conservative" variables ρ_*, $\tilde{\tau}$, and $\tilde{S}_i$. We perform the inversion as specified in Eqs. (57)–(62) of [89], but with a slightly modified analytic quartic solver from the GNU Scientific Library that outputs only the real roots. We use the same technique as in [100] to ensure that the values of $\tilde{S}_i$ and $\tilde{\tau}$ yield physically valid primitive variables, except we reset $\tilde{\tau}$ to $10^{-10}\tilde{\tau}_{0,\rm max}$ (where $\tilde{\tau}_{0,\rm max}$ is the maximum value of $\tilde{\tau}$ initially) when either $\tilde{S}_i$ or $\tilde{\tau}$ is

unphysical (i.e., violate one of the inequalities (34) or (35) in [100]). The restrictions usually apply only to the region near the puncture inside the horizon.

For each of our calculations, we set our outer boundary at $128M$ and use 8 AMR refinement levels. The maximum resolution near each BH is $\delta x/M = 0.03125$. For our single BH test calculations, we place our outer boundary at $128M$ and use 6 AMR refinement levels. For these cases, the highest resolution near the BH is $\delta x/M = 0.0625$.

We model the emission of electromagnetic radiation by treating this radiation loss as a perturbation, and neglect its influence on the hydrodynamic flow, as well as any deviation from adiabaticity that it induces.

4.4 Diagnostics

4.4.1 Surface density

In order to track the global evolution of disk structure and compare with other disk calculations, it is useful to define the surface density Σ. Following [101], we define

$$\Sigma(R,\phi) = \int_{z\geq 0} \rho_0 u^t \sqrt{-g} dz \ , \tag{4.1}$$

where $R \equiv \sqrt{x^2+y^2}$ (R will always be the cylindrical radius in this thesis, while r will always be the spherical polar radius). We also report the angle-averaged surface density $\langle\Sigma(R)\rangle$ where

$$\langle\Sigma\rangle \equiv \frac{1}{2\pi}\int_0^{2\pi} \Sigma d\phi \ . \tag{4.2}$$

4.4.2 Flux diagnostics

To derive meaningful flux diagnostics we must identify the conserved currents. Details of this derivation are given in Appendix C. To summarize, consider a 3D region Σ_t which lies between two world tubes F and L on a timeslice t=const. Let F be defined by $h(t,x,y,z) = 0$, and L be defined by $l(t,x,y,z) = 0$. In [16], this region is depicted as the lower shaded region in Fig. 24. For the purposes of this thesis, we let F be the world tube defined by the apparent horizon(s), and L be the world tube defined by a sphere of constant coordinate radius centered at the origin. Of course the surfaces could be chosen to take on other shapes as well.

4.4.3 Conserved quantities

Now consider a conserved current, j^μ which satisfies

$$\nabla_\mu j^\mu = 0 \ . \tag{4.3}$$

Then it can be shown that (see e.g. Appendix A of [16])

$$\dot{q} \equiv \frac{dq}{dt} = -\mathcal{F}_F + \mathcal{F}_L \ , \tag{4.4}$$

where

$$q(t) = \int_{\Sigma_t} j^\mu d^3\Pi_\mu \tag{4.5}$$

$$= \int_{\Sigma_t} j^t \sqrt{-g}\ d^3x \ , \tag{4.6}$$

$$\mathcal{F}_F = -\int_F \sqrt{-g'} j^h da db \ , \tag{4.7}$$

$$\mathcal{F}_L = -\int_L \sqrt{-g'} j^l da db \ . \tag{4.8}$$

Here g' is the determinant of the metric in the (t, h, a, b) or (t, l, a, b) coordinate systems. In the above example, $\mathcal{F}_F$ is the flux of q across the horizon(s), while $\mathcal{F}_L$ is the flux of q across the outer sphere.

4.4.4 Freedom in coordinate choice

These fluxes are independent of any changes in coordinates that leave the slicing intact. Equivalently, we may alter the shift without affecting the flux, but the lapse must be kept the same. We can rewrite these fluxes in any other coordinate system (t, x, y, z) which preserves the same slicing. While a and b can be any two coordinates on the surface, we label them here as θ and ϕ for convenience, as this is done in our actual numerical calculations,

$$\mathcal{F}_F = -\int_F \sqrt{-g}\ det \left| \frac{\partial(x,y,z)}{\partial(h,\theta,\phi)} \right| j^\mu \partial_\mu h\ d\theta d\phi \ , \tag{4.9}$$

$$\mathcal{F}_L = -\int_L \sqrt{-g}\ det \left| \frac{\partial(x,y,z)}{\partial(l,\theta,\phi)} \right| j^\mu \partial_\mu l\ d\theta d\phi \ . \tag{4.10}$$

4.4.5 Rest-mass conservation

Rest-mass conservation, $\nabla_\mu(\rho_0 u^\mu) = 0$, corresponds to $j^\mu = \rho_0 u^\mu$. If we now define

$$M_0 \equiv \int_{\Sigma_t} \sqrt{-g}\rho_0 u^0 d^3x = \int_{\Sigma_t} \rho_* d^3x \ , \tag{4.11}$$

$$\mathcal{F}_F^{(M)} \equiv -\int_F \sqrt{-g}\ det\left|\frac{\partial(x,y,z)}{\partial(h,\theta,\phi)}\right| \rho_0 u^\mu h_{,\mu}\ d\theta d\phi \ , \tag{4.12}$$

$$\mathcal{F}_L^{(M)} \equiv -\int_L \sqrt{-g}\ det\left|\frac{\partial(x,y,z)}{\partial(l,\theta,\phi)}\right| \rho_0 u^\mu l_{,\mu}\ d\theta d\phi \ , \tag{4.13}$$

then we may integrate Eq. (4.4) in time to derive the following rest-mass conservation law

$$\left(M_0(t) + \int_{t_i}^{t} dt \left(\mathcal{F}_F^{(M)} - \mathcal{F}_L^{(M)}\right)\right)/M_{0,i} = 1 \ , \tag{4.14}$$

where $M_{0,i}$ is the rest mass between the horizons and the surface L at $t = 0$. Equivalently, we can define the rest-mass accretion rate

$$\dot{M}_0 \equiv -\mathcal{F}_F^{(M)} + \mathcal{F}_L^{(M)} \ . \tag{4.15}$$

4.4.6 $E - \Omega J$ conservation

We employ the helical Killing vector defined in Eq. (2.26) to construct another conserved current,

$$j^\mu \equiv \xi_\nu T^{\mu\nu} = T^\mu{}_t + \Omega T^\mu{}_\phi \ . \tag{4.16}$$

We now define the following quantities

$$E(t) \equiv -\int_{\Sigma_t} \sqrt{-g} T^t{}_t\ d^3x \ , \tag{4.17}$$

$$J(t) \equiv \int_{\Sigma_t} \sqrt{-g} T^t{}_\phi\ d^3x \ , \tag{4.18}$$

$$\mathcal{F}_F^{(E)} \equiv \int_F \sqrt{-g}\ det\left|\frac{\partial(x,y,z)}{\partial(h,\theta,\phi)}\right| T^\mu{}_t h_{,\mu}\ d\theta d\phi \ , \tag{4.19}$$

$$\mathcal{F}_L^{(E)} \equiv \int_L \sqrt{-g}\ det\left|\frac{\partial(x,y,z)}{\partial(l,\theta,\phi)}\right| T^\mu{}_t l_{,\mu}\ d\theta d\phi \ , \tag{4.20}$$

$$\mathcal{F}_F^{(J)} \equiv -\int_F \sqrt{-g}\ det\left|\frac{\partial(x,y,z)}{\partial(h,\theta,\phi)}\right| T^\mu{}_\phi h_{,\mu}\ d\theta d\phi \ , \tag{4.21}$$

$$\mathcal{F}_L^{(J)} \equiv -\int_L \sqrt{-g}\ det\left|\frac{\partial(x,y,z)}{\partial(l,\theta,\phi)}\right| T^\mu{}_\phi l_{,\mu}\ d\theta d\phi \ , \tag{4.22}$$

and we see that Eqs. (4.4) and (4.16) give

$$\dot{E} - \Omega \dot{J} = -\left(\mathcal{F}_F^{(E)} - \Omega \mathcal{F}_F^{(J)}\right) + \left(\mathcal{F}_L^{(E)} - \Omega \mathcal{F}_L^{(J)}\right) \ , \tag{4.23}$$

for spacetimes possessing a helical Killing vector. Again, we may integrate in time to derive another conservation law

$$E(t) - \Omega J(t) + \int_{t_i}^{t} dt \left(\mathcal{F}_F^{(E)} - \Omega \mathcal{F}_F^{(J)}\right) - \int_{t_i}^{t} dt \left(\mathcal{F}_L^{(E)} - \Omega \mathcal{F}_L^{(J)}\right) = E(t_i) - \Omega J(t_i)$$

4.4.7 Spiral density wave diagnostics

In our simulations, we use our CTS metric and Eq. (2.28) to ensure that our disk models exhibit quasistationary behavior before we begin the binary inspiral. Such quasistationary configurations are interesting in their own right, as they lend insight into any accretion flow onto a binary before merger. A key feature of this flow is the presence of spiral density waves in the inner disk cavity. Following [36], we highlight the existence of these density waves by calculating the surface density fluctuation $\delta\Sigma$, defined by

$$\delta\Sigma \equiv \frac{\Sigma - \langle\Sigma\rangle}{\langle\Sigma\rangle} \ . \tag{4.24}$$

We also define the torque density, dT/dR, for comparison with analytic models and other simulations,

$$\frac{dT}{dR} = \int \sqrt{-g} T^{\mu}{}_{\nu} \nabla_{\mu} \phi^{\nu} R dz d\phi \ , \tag{4.25}$$

where $\phi^{\mu} \equiv (\partial_{\phi})^{\mu}$, which gives $\phi^{\mu} = (0, -y, x, 0)$ in Cartesian coordinates. Details of the derivation of Eq. (4.25) are given in Appendix B.

4.4.8 Luminosity diagnostics

In order to study the electromagnetic emission from our disk evolutions, we estimate the luminosity due to thermal bremmstrahlung and nonthermal synchrotron emission using the approximations described in [16]. For synchrotron emission, we assume the presence of a small-scale, turbulent B field whose magnitude is approximated by setting $P = \beta P_M \equiv \beta B^2/(8\pi)$. We thus assume that the magnetic pressure is some fraction $1/\beta$ of its equipartition value. Simulations of magnetized accretion flows have demonstrated that the magnetic fields do not typically reach their full equipartition value [102]. We have chosen $\beta = 10$ to account for this. We also assume that the radiation propagates through an optically thin gas and we neglect

the roles of radiation pressure and radiative cooling on the hydrodynamic evolution. While an accurate estimation of the electromagnetic emission requires a full solution to the radiative transfer problem, this crude method can provide a reasonable estimate of the magnitude of the emission under suitable conditions.

Chapter 5

Code Tests

Our HRSC general relativistic hydrodynamic code has been thoroughly tested by passing a robust suite of tests. These tests include maintaining stable rotating stars in stationary equilibrium, reproducing the exact Oppenheimer-Snyder solution for collapse to a BH, and reproducing analytic solutions for relativistic shocks, alfven waves, and spherical Bondi accretion onto isolated BHs [89]. Our code has also been used to simulate the collapse of very massive, rotating stars to black holes [103]; merging BHBH binaries [86], BHNS binaries [100, 104], and relativistic hydrodynamic matter in the presence of puncture black holes [105]. Recently, our code has been generalized to incorporate (optically thick) radiation transport and its feedback on fluids in dynamical spacetimes [106].

All of the above tests and simulations were performed on grids with uniform spacing. In some of the simulations, we utilized the multiple-transition fisheye transformation [107] so that a uniform computational grid spacing corresponds to physical coordinates with spatially varying resolution. Recently, we have modified our code so that we can use the moving-box AMR infrastructure provided by Carpet [96]. To test our new code, we have performed shock-tube tests and 3+1 simulations of linear gravitational waves, single stationary and boosted puncture BHs, puncture BHBH binaries, and rapidly and differentially rotating relativistic stars. Our AMR code has also been used to perform simulations of BHNS mergers [104].

All of our 3+1 AMR code tests were performed assuming equatorial symmetry (i.e., symmetry about the $z = 0$ orbital plane), which we assume in all evolutions presented in this paper. We have also checked that our AMR code is able to accurately reproduce the analytic Bondi solution, and we have shown good agreement with the results of [68] for BHL accretion. Results of the latter two tests are summarized in Sec. 5.2.

5.1 Analytic Relativistic Bondi Solution

Steady state, adiabatic, spherically symmetric accretion onto point masses was first considered by Bondi for Newtonian gravitation [62]. This work was later extended to handle accretion onto BHs in general

relativity [63, 64, 108, 109]. A thorough discussion of the relativistic solution may be found in Appendix G of [65]. Here we briefly summarize this solution. We consider spherically symmetric, steady-state accretion onto a Schwarzschild BH of mass M. We assume that the BH is at rest in an infinite gas cloud which has rest-mass density ρ_∞, pressure P_∞, and fluid 4-velocity $u^i = 0$ at infinity. We assume that the gas is adiabatic with an adiabatic index Γ. We can solve the equations of relativistic hydrodynamics to derive an exact solution for the accretion flow.

Key Equations

For simplicity, we will derive the solution in Schwarzschild coordinates, then transform to isotropic coordinates. We begin by recasting the steady-state relativistic continuity and Euler equations into an integral form, following the derivation outlined in [65],

$$4\pi\rho_0\hat{u}\hat{r}^2 \equiv \dot{M} = \text{const.} \tag{5.1}$$

$$h^2\left(1 - \frac{2M}{\hat{r}} + \hat{u}^2\right) \equiv h_\infty^2 = \text{const.} \tag{5.2}$$

Here, $\hat{r}$ and $\hat{u}$ denote the radius and radial fluid 4-velocity in Schwarzschild coordinates.

For adiabatic flow, the Γ-law EOS implies the polytropic relation $P = K\rho_0^\Gamma$, with K =const. Thus

$$P = K\rho_0^\gamma = (\Gamma - 1)\rho_0\frac{h-1}{\Gamma} \ . \tag{5.3}$$

For an adiabatic gas, the speed of sound is,

$$a \equiv \frac{1}{h^{1/2}}\left(\frac{dP}{d\rho_0}\right)^{1/2} = \left(\frac{\Gamma P}{\rho_0 h}\right)^{1/2} \ . \tag{5.4}$$

This leads to the following relations between the enthalpy, the speed of sound, and the temperature

$$a^2 = (\Gamma - 1)\frac{h-1}{h} \tag{5.5}$$

$$kT \equiv \frac{P}{2n} = \frac{m_B}{2}\frac{\Gamma - 1}{\Gamma}(h-1) \ . \tag{5.6}$$

Any solution satisfying Eqs. (5.1) and (5.2) that maintains the causality constraint $a^2 < 1$ must contain a transonic radius outside the event horizon [65]. At the transonic radius the radial velocity $\hat{u}_s$ and the speed

of sound are given by

$$\hat{u}_s^2 = \frac{M}{2\hat{R}_s} , \tag{5.7}$$

$$a_s^2 = \frac{M/2\hat{R}_s}{1 - 3M/2\hat{R}_s} . \tag{5.8}$$

The transonic radius sets the length scale at which the fluid parameters begin to deviate from their asymptotic values during inward flow. We derive the transonic radius by plugging Eq. (5.8) into Eq. (G.30) from Appendix G of [65]. This leads to a polynomial equation which we solve using a numerical root solver. In the Newtonian limit, in which $a_\infty \ll 1$ and $M/R_s \ll 1$, we recover the expressions,

$$R_s = \begin{cases} \dfrac{5-3\Gamma}{4}\dfrac{M}{a_\infty^2} & 1 \le \Gamma < 5/3 \\ \dfrac{3}{4}\dfrac{M}{a_\infty} & \Gamma = 5/3 . \end{cases} \tag{5.9}$$

Knowing the transonic radius, the accretion rate is given by

$$\dot{M} = 4\pi\rho_s\hat{u}_s\hat{R}_s^2 = 4\pi\lambda M^2\rho_\infty a_\infty^{-3} , \tag{5.10}$$

where $\lambda = \lambda(\Gamma, a_\infty)$ is a parameter of order unity, which in the Newtonian limit is given by

$$\lambda = \left(\frac{1}{2}\right)^{(\Gamma+1)/2(\Gamma-1)} \left(\frac{5-3\Gamma}{4}\right)^{-(5-3\Gamma)/2(\Gamma-1)} . \tag{5.11}$$

In the relativistic domain, we must solve a cubic equation for to find λ (see [65] for details). Given values for $\rho_{0,\infty}$ and T_∞, we can determine $\dot{M}$ and h_∞ using Eqs. (5.5), (5.6), and (5.10). We can then use Eqs. (5.1) and (5.2), along with the EOS, Eq. (5.3), to obtain the complete analytic solution.

Transformation to isotropic coordinates

In order to provide initial data for our simulations, we transform the solution to isotropic coordinates, the coordinate system adopted for our metric (puncture) initial data. The relation between Schwarzschild radius $\hat{r}$ and isotropic radius r outside the horizon is given by

$$\hat{r} = r\left(1 + \frac{M}{2r}\right)^2 \tag{5.12}$$

$$r = \frac{\hat{r} - M + \sqrt{\hat{r}(\hat{r} - 2M)}}{2} . \tag{5.13}$$

Since the flow is purely radial, we have

$$\begin{aligned} u &= -u^r = -\hat{u}^{\hat{r}} \frac{dr}{d\hat{r}} = \hat{u} \left(\frac{d\hat{r}}{dr} \right)^{-1} \\ &= \frac{\hat{u}}{(1 - M/2r)(1 + M/2r)} , \end{aligned} \tag{5.14}$$

where u^r is the radial component of the 4-velocity. The time component of the 4-velocity, u^0, remains unchanged by the transformation. We find the 3-velocity $v = v^r = u^r/u^0$ from the normalization condition $u^\alpha u_\alpha = -1$, or

$$-\alpha^2 (u^0)^2 + e^{4\phi} (u^0)^2 v^2 = -1 \tag{5.15}$$

The above transformation is needed only when assigning fluid initial data for $r > r_0$. We follow the method of [105] and adjust the fluid parameters within the radius r_0. We choose $r_0 = 0.6M$, which is outside the horizon, to avoid the initial coordinate singularity of u^0 at the horizon. There is no singularity during the evolution as the adopted 1+log slicing condition is horizon penetrating.

Moving Bondi solutions

We also wish to consider the problem of adiabatic, steady-state accretion onto a BH which moves with constant velocity V_∞ through a gas which is uniform at infinity. This problem was first studied in Newtonian gravitation in [66] and [67], and is often referred to as "Bondi-Hoyle-Lyttleton (BHL) accretion". The problem has also been studied numerically in Newtonian theory by [69, 70], and for BHs in full general relativity by [68, 71]. For cases in which the gas is not at rest asymptotically, we construct initial data following the method described in [105], in which we "boost" the stationary Bondi solution by taking the initial density at any coordinate point to be approximately the stationary isotropic Bondi solution, and computing the initial velocity field employing a "Lorentz transformation" for the velocities. See [16] for details of this transformation. This method of computing initial data is only strictly valid asymptotically. This is because we use the Bowen-York initial data for the moving BH metric, which are not obtained by boosting the stationary BH metric. However, we find that deviations propagate away quickly, leaving a stationary flow. In Sec. 5.2 we describe a simulation of Bondi accretion which we perform in a moving reference frame. In this case, we use the same technique described above to construct hydrodynamic initial data.

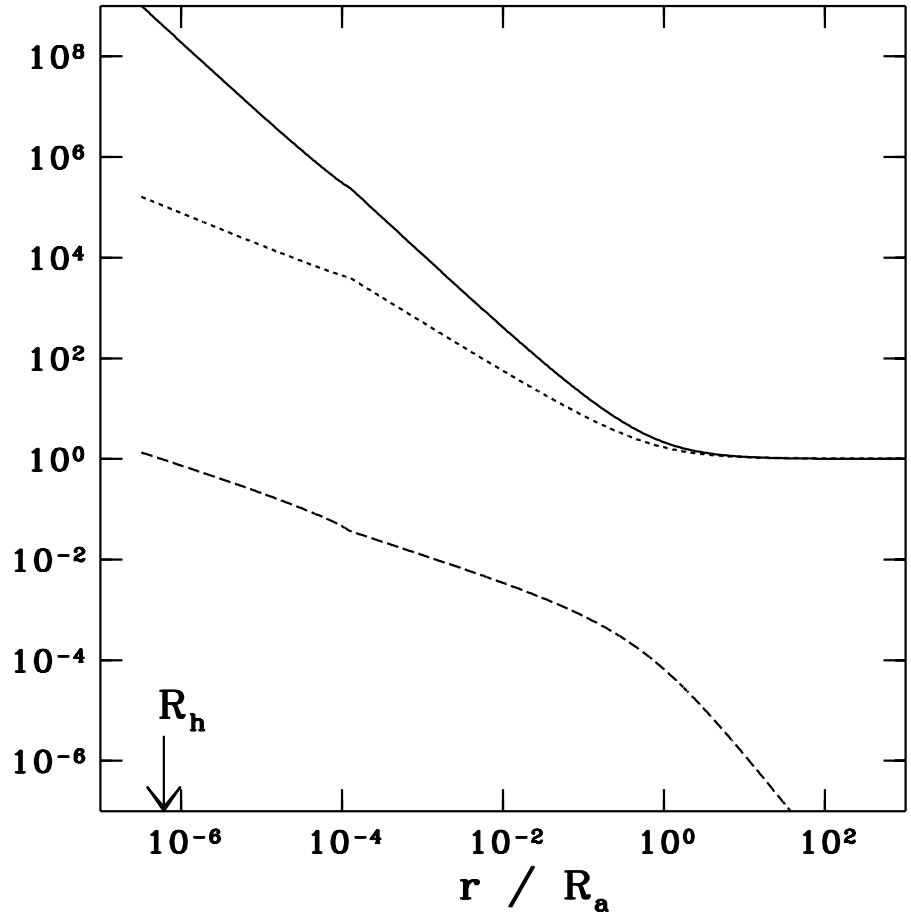

Figure 5.1: Semi-analytic profiles of density, temperature and fluid 4-velocity for spherical, adiabatic Bondi accretion onto a Schwarzschild BH. The solid line gives $\rho_0/\rho_{0,\infty}$, the dotted line shows T/T_∞, and the dashed line shows the fluid 4-velocity in Schwarzschild coordinates, $\hat{u}$. The adiabatic index is given by $\Gamma = \Gamma^*$ according to Eq. (5.16). The asymptotic temperature is $T_\infty = 10^6 K$. The horizon is labeled R_h.

Effective adiabatic index

In some cases, we consider a gas cloud which the electrons have nonrelativistic temperatures at infinity, but achieve relativistic temperatures near the binary. In this case we follow [64] and define an "effective adiabatic index" Γ^* according to

$$\Gamma^* = \begin{cases} 5/3 & kT/m_e c^2 \leq 2/3 \\ 13/9 & kT/m_e c^2 > 2/3 \ , \end{cases} \tag{5.16}$$

Thereby replacing the actual continuous transition by a simpler discrete transition. This transition occurs at a Schwarzschild radius [65]

$$\frac{r_*}{M} \approx \frac{9}{40}\frac{m_p}{m_e} \approx 400 \ . \tag{5.17}$$

We solve for r_* using Eqs. (5.1), (5.2), (5.6), and the fact that $kT(r_*) = (2/3)m_e c^2$. Using the continuity of ρ_0 and P at $r = r_*$, we obtain the full equilibrium flow solution. In practice, r_* is outside the outer boundary of the computational grid in our simulations, so we still implement a constant Γ. However, taking into account this transition alters our initial data significantly, since the outer $\Gamma = 5/3$ region drives $a \lesssim u$ up to $r = r_*$, increasing the gas temperature near the black hole when compared to gas in which $\Gamma = 13/9$ everywhere. Analytic profiles of density, temperature, and fluid velocity for this equation of state are plotted in Fig. 5.1.

5.2 Relativistic Bondi test

We test our code's ability to accurately simulate hydrodynamic accretion onto a moving puncture. This is particularly important in an AMR code in which matter crosses moving refinement zone boundaries. To test our code, we simulated spherical Bondi accretion in a frame in which both the BH and gas cloud are moving with the same velocity. We consider a BH moving with velocity $V_{BH} \equiv P^x/M = 0.37$, initially situated at the origin. Here P^x is the momentum of the BH as measured by a stationary coordinate observer at infinity. We consider a gas with adiabatic index $\Gamma = 13/9$ with asymptotic sound speed $a_\infty^2 = 0.022$ also moving with velocity $v = V_{BH}$ at infinity. With this choice the transonic radius is given by areal radius $R_a = 45.5M$ in the comoving frame. We evolve for a duration $t = 713.6M$, which is approximately equal to two free-fall times at the accretion radius. By this time, the BH has moved to a coordinate location of $x = 247M$.

To assess the agreement with the analytic solution, we compare invariant quantities [105]. Two such invariants are the fluid rest-mass density, ρ_0, and the the rate of change of the fluid rest-mass density, as

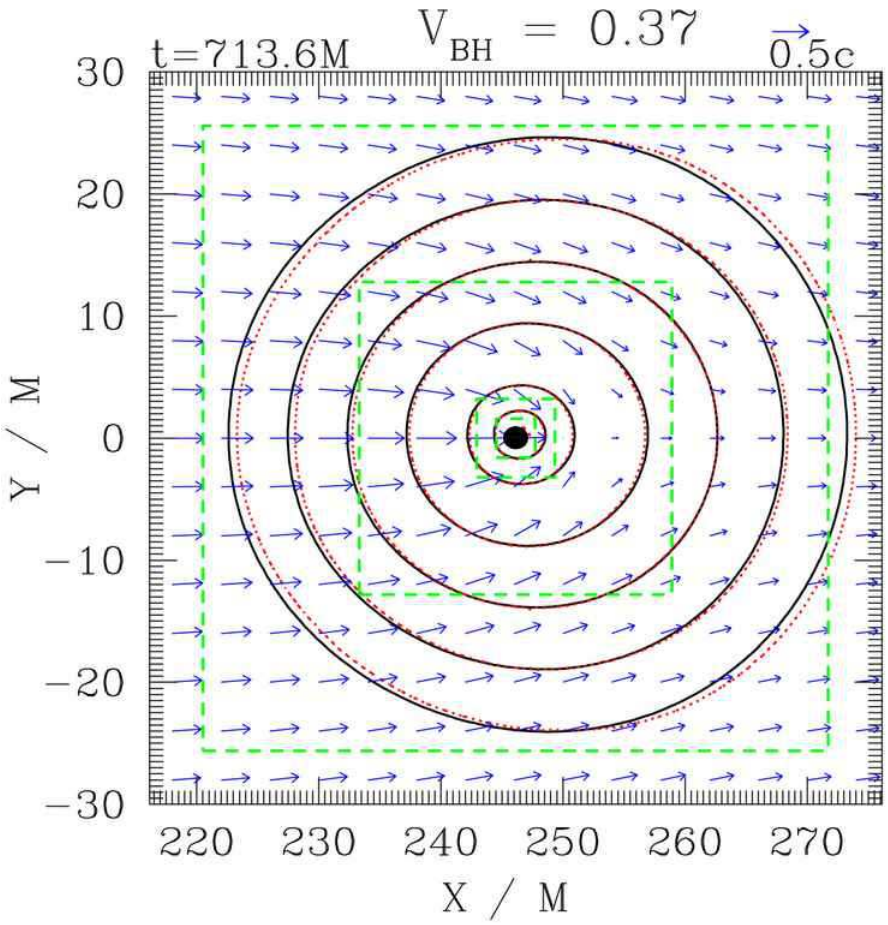

Figure 5.2: Snapshots showing spherical Bondi accretion onto a single BH simulated in a frame in which the BH and gas move with velocity $V_{BH} = 0.37$. Contours of constant density ρ_0 (solid black lines) and constant $d\rho_0/d\tau$ (dotted red lines) are shown. Their overlap indicates agreement with the analytic Bondi solution. The adiabatic index is set to $\Gamma = 13/9$ and $a_\infty = 0.148$. The green dashed lines show the boundaries of the innermost AMR refinement levels. Arrows denote velocity vectors.

measured by a comoving observer, $d\rho_0/d\tau$. We choose a set of 6 areal radii in the comoving frame. At each radius, we compute ρ_0 and $d\rho_0/d\tau$ analytically. By construction, contours of ρ_0 and $d\rho_0/d\tau$ are spherical and coincide in this frame. However, because ρ_0 and $d\rho_0/d\tau$ are both coordinate-independent quantities, their contours must continue to coincide in *any* coordinate frame. We use this fact to check that our numerical simulation, performed in a frame in which the BH and gas are moving, matches the analytic solution (see Fig. 5.2).

5.3 Relativistic Bondi-Hoyle-Lyttleton test

We will simulate cases of accretion onto binaries in which the BHBH center of mass moves relative to the asymptotic gas cloud. Here we verify that we can accurately simulate "BHL" accretion of a single puncture BH moving at constant velocity through a gas cloud. While there is no analytic solution for this problem, we compare our findings with results of previous work. We consider a test case in which a single BH puncture is placed in a cloud with asymptotic sound speed $a_\infty = 0.1$ and $\Gamma = 4/3$, with the puncture moving supersonically with speed $V_\infty = 0.25$ relative to the gas cloud. We perform our simulation in a frame in which the puncture is at rest and the asymptotic fluid velocity is set to V_∞. Figure 5.3 shows a snapshot of the stationary-state density and velocity profile from our simulation. We measure $\dot{M}$ and compare with the results of [68]. In order to facilitate this comparison, we define a canonical unit of rest-mass accretion flux to be

$$\dot{M}_{can} = \frac{4\pi\lambda M^2 \rho_{0,\infty}}{(V_\infty^2 + a_\infty^2)^{3/2}} \ , \tag{5.18}$$

We find $\dot{M}/\dot{M}_{can} = 2.6$, which is slightly smaller than the value 3.0 reported in [68]. We have varied our resolution and determined that our results are convergent to within $\sim 1\%$. Thus, the most likely sources of the small discrepancy are the outer boundary condition (we use the stationary spherical Bondi solution with a Lorentz boost, whereas [68] use constant asymptotic values), and the fact that [68] impose an approximate inner boundary condition outside the horizon. Other differences between these two codes are that we use a 3+1 code with AMR, whereas [68] employ an axisymmetric code. Also, our outer boundary is placed at $r_{max}/M = 820$ for this test, whereas [68] place the outer boundary at $r_{max}/M = 140$.

5.4 Disk tests

All of our 3+1 AMR code tests were performed assuming equatorial symmetry (i.e., symmetry about the $z = 0$ orbital plane), which we assume in all evolutions presented in this paper. We have checked that our AMR code is able to accurately maintain a stable equilibrium disk around a single Schwarzschild BH, as demonstrated in Fig. 5.4. For this test, we use the same disk initial data as run A1 in Table 6.4, except that we set the background metric to be that of a single Schwarzchild BH at the origin. As we describe in Sec. 4.2, such a disk is an equilibrium solution and is expected to maintain its initial profile.

We have also checked that the conservations laws in Eqs. (4.14) and (4.24) are satisfied in a quasistationary, binary spacetime, as described in Sec. 4.4. In Fig. 5.5, the dashed red curve shows the left-hand side of Eq. (4.14), with the world tube L chosen to correspond to a sphere centered at the orgin with a radius

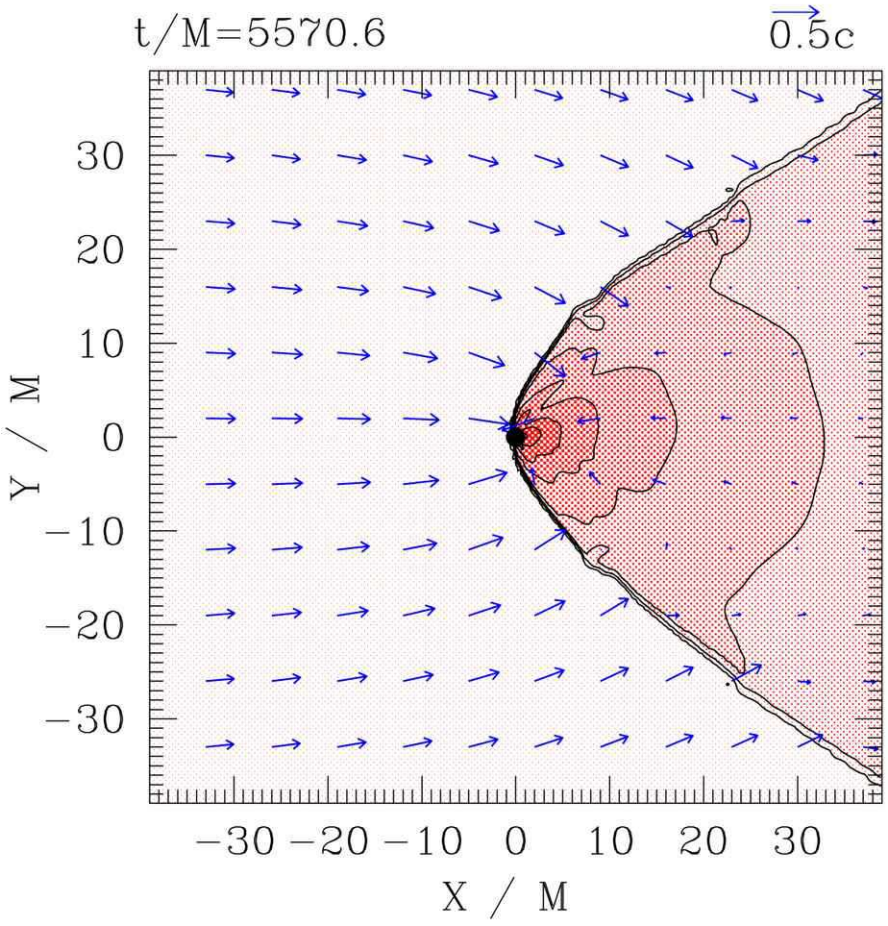

Figure 5.3: Snapshots of density contours for the BHL accretion code test. The adiabatic index is $\Gamma = 4/3$, the sound speed is $a_\infty = 0.1$. Density contours are chosen at $\rho_0 = \rho_{0,\infty} 10^{0.25j}$ $(j = 1, 2, ...12)$. Contours of highest density are very near the BH. Arrows represent velocity vectors.

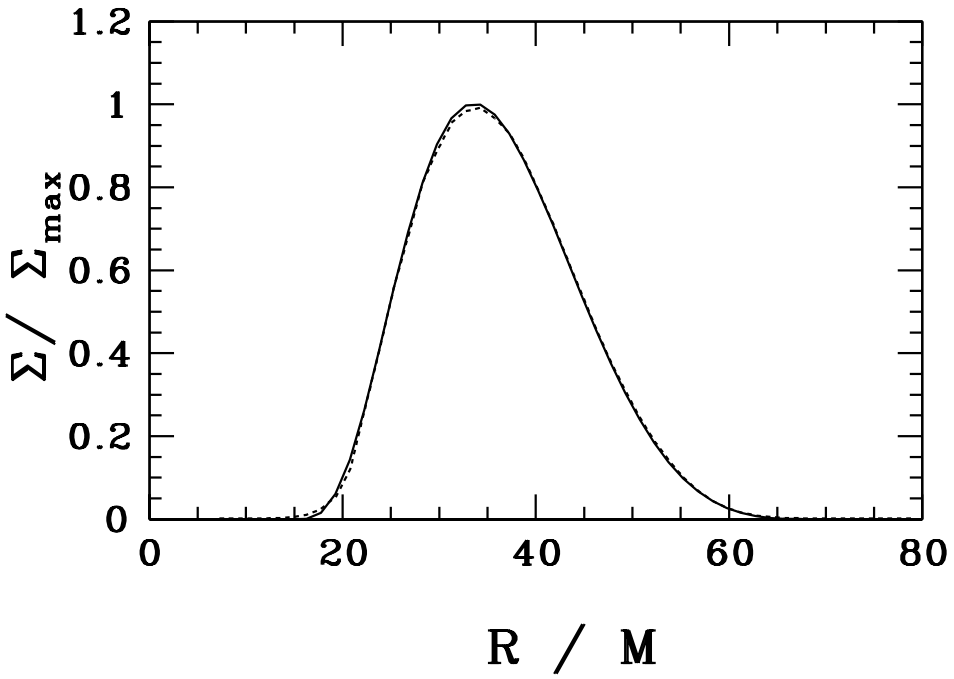

Figure 5.4: Surface density profiles at $t = 0$ (solid line) and $t \approx \ t_{disk}$ (dotted line), where t_{disk} is the Keplerian period at the radius of maximum pressure. Overlap indicates that disk accurately maintains equilibrium configuration over this time scale.

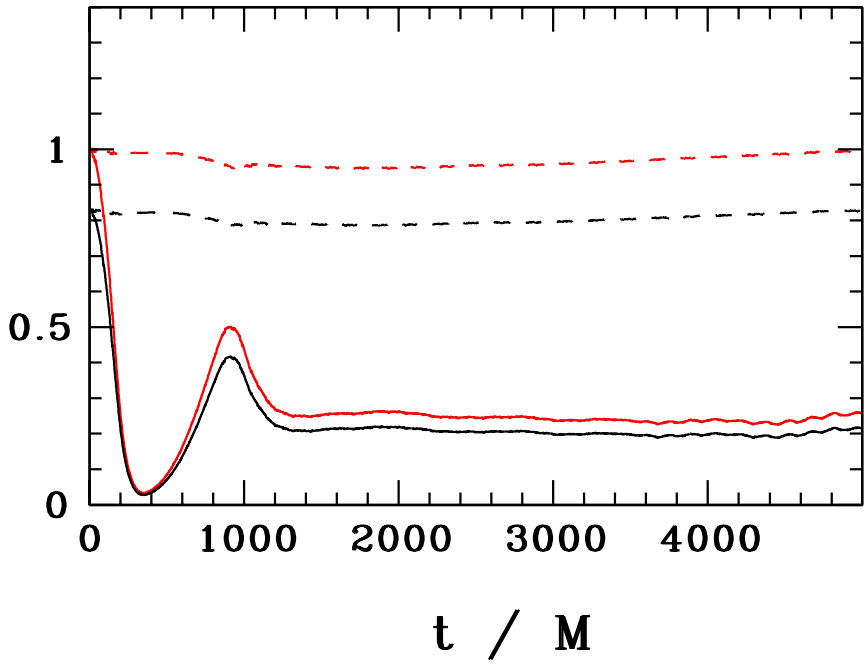

Figure 5.5: Plots demonstrating the accurate maintenance of conserved quantities. Rest mass $M_0(t)/M_{0,i} + \int dt\ (\mathcal{F}_F^{(M)} - \mathcal{F}_L^{(M)})/M_{0,i}$ (dashed red line) maintains its initial value accurately when compared to $M_0/M_{0,i}$ (solid red). Similarly, the conserved quantity $(E(t) - \Omega J(t) + \int dt\ (\mathcal{F}_F^{(E)} - \Omega \mathcal{F}_F^{(J)}) - \int dt\ (\mathcal{F}_L^{(E)} - \Omega \mathcal{F}_L^{(J)}))/M_{0,i}$ (dashed black line) maintains its initial value accurately when compared to $(E(t) - \Omega J(t))/M_{0,i}$ (solid black line).

$r_L = 25M$. For comparison, we also plot $M_0(t)/M_{0,i}$ with the solid red curve. The data are from run A2, in which we impose a helical Killing vector to solve for the metric as described in Sec. 2.6, while evolving the hydrodynamics using Eqs. (3.13), (3.14), and (3.15). We find that Eq. (4.14) is well satisfied, indicating that our code is conserving rest mass correctly. Similarly, the dashed black line shows the left-hand side of Eq. (4.24), normalized by $M_{0,i}$, while the solid black line shows $(E(t) - \Omega J(t))/M_{0,i}$ for comparison. Again, we see that our code is conserving $E - \Omega J$ correctly.

Chapter 6

Results

6.1 Binary Bondi-Hoyle-Lyttleton accretion

The transonic radius for Bondi accretion with a realistic asymptotic temperature of $10^6 K$ is $R_a \sim 10^6 M$. It is beyond the capability of current $3+1$ GR simulations to evolve the binary from initial separation $d > R_a$ all the way to merger, while resolving a BH horizon of size $\sim M$. The range of length scales is too large and the total coalescence time too long for such a task. We approach this issue by performing two types of simulations. We perform simulations of binaries merging in "realistic" gas clouds with asymptotic temperature $T_\infty = 10^6 K$, following only the last phase of the merger in which the binary separation satisfies $d \ll R_a$. Our focus here is on identifying observable electromagnetic signals generated by the time-dependent shock heating caused by the binary motion. We also perform "prototype" calculations with artificially high temperatures and sound speeds in order to study how the accretion flow changes as the binary transitions between the following regimes during the inspiral:

1. "widely separated regime", in which $d > R_a$
2. "moderately separated regime", in which $d \approx R_a$
3. "closely separated regime", in which $d < R_a$

We set the asymptotic temperature $T_\infty \sim 10^{11} K$ in the "prototype" calculations to decrease the accretion radius R_a to a value closer to d so that we can explore all three regimes by combining the results of several numerical simulations. All of our BHBH simulations are summarized in Table 6.1. Important results are summarized in Table 6.2 and Table 6.3. The initial BHs in the binary are all equal-mass and nonspinning.

6.1.1 Scaling

For a given asymptotic gas temperature T_∞ or sound speed a_∞, our solution for binary Bondi flow can be scaled to arbitrary density $n_\infty \equiv \rho_{0,\infty}/m_B$ (neglecting self-gravity of the gas) and black hole mass M. Hence a single simulation with an arbitrary n_∞ and M suffices to determine the solution for any other n_∞

Table 6.1: Parameters for BHBH simulations

run	run type	V_∞	V_∞/a_∞	Γ	$T_\infty(K)$	a_∞	$^\dagger R_a/M$	$^{\dagger\dagger}d/M$
PA1	prototype	0.0	0.0	13/9	8.73×10^{10}	0.148	22.7	$40, 20, 14, 10$
PA2				4/3	9.62×10^{10}			
PA3				5/3	7.44×10^{10}			
PB1		0.1	0.7	13/9	8.73×10^{10}	0.148	15.6	$40, 10$
PB2				4/3	9.62×10^{10}			
PB3				5/3	7.44×10^{10}			
PC1		0.4	2.7	13/9	8.73×10^{10}	0.148	2.74	$40, 10$
PC2				4/3	9.62×10^{10}			
PC3				5/3	7.44×10^{10}			
RA1	realistic	0.0	0.0	Γ^*	1×10^6	5.53×10^{-4}	3.27×10^6	10
RA2				5/3				

$^\dagger R_a = (M/2)/(a_\infty^2 + V_\infty^2)^{3/2}$ is the accretion radius for a single BH of mass $M/2$.
$^{\dagger\dagger}d =$ initial binary separation; simulations beginning at $10M$ proceed to merger.

Table 6.2: Parameters for BHBH simulations

run	flow characteristics[§]			
	n_{max}/n_∞	T_{max}/T_∞	K_{max}/K_∞	$^\dagger\dot{M}_{max}/\dot{M}_a$
PA1	631	18.3	1.2	3.7
PA2	1743	14.3	1.5	3.8
PA3	164	30.1	1.6	2.6
PB1	593	18.9	1.2	4.0
PB2	1638	15.2	1.7	3.3
PB3	153	30.8	1.9	2.5
PC1	99.2	28.3	6.0	0.7
PC2	158	32.2	14.0	0.7
PC3	46.6	37.7	6.5	0.8
RA1	1.4×10^{10}	1.8×10^6	4.7	3.9
RA2	3.63×10^9	2.7×10^6	13.0	3.3

$^\dagger\dot{M}_a c^2 = 4.6\times10^{40}\ \lambda_{5/3}\ n_1\ T_6^{-3/2}\ M_6^2$ erg s^{-1} is the accretion rate onto a single BH of mass $M/2$ undergoing stationary, spherical Bondi accretion.
[§] "max" label refers to the characteristic value at the moment of maximum luminosity.

Table 6.3: Parameters for BHBH simulations

run	emission characteristics[§§]				
	$^{\dagger\dagger}L_{ff}^{max}/L_{35}$	$h\nu_{ff}^{max}$	$^{\dagger\dagger}L_{syn}^{max}/L_{35}$	$h\nu_{syn}^{max}$	
RA1	300	150 MeV	$3\times10^8\beta_1^{-1}$	$80/(1+z)\ n_1^{1/2}\ T_6^{-3/4}\beta_1^{-1/2}$	eV
RA2	400	230 MeV	$4\times10^8\beta_1^{-1}$	$100/(1+z)\ n_1^{1/2}\ T_6^{-3/4}\beta_1^{-1/2}$	eV

$^{\dagger\dagger}L_{35} = 10^{35}\ n_1^2\ T_6^{-3} M_6^3$ erg s^{-1}
[§§] "max" label refers to the maximum values of the luminosities during the merger and the characteristic frequencies at these times.

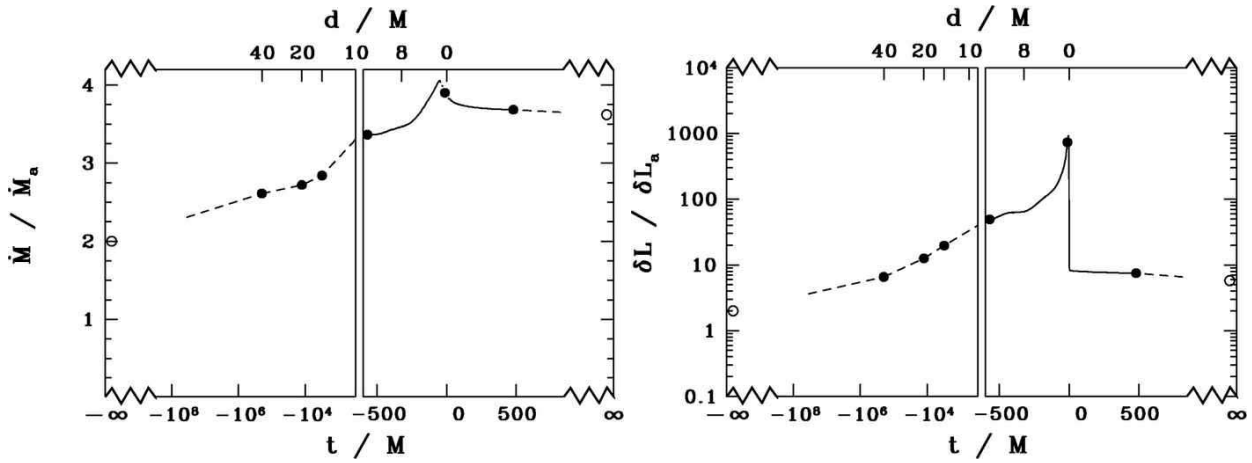

Figure 6.1: Time evolution of $\dot{M}$ and δL for binary Bondi accretion for the prototype case with $\Gamma = 13/9$. Time t/M is measured relative to the time at which the merger occurs. $\dot{M}_a$ and δL_a are the accretion rate and luminosity enhancement over the background for a single isolated black hole with mass equal to the initial ADM mass of the binary. The left-hand box shows values from "snapshots" in regimes 1 and 2. The right-hand box shows results for the final inspiral and merger from an initial separation of $d = 10M$ (regime 3). Solid lines denote numerical data, dashed lines denote extrapolated data. Solid dots correspond to profile plots highlighted in Fig. 6.4, while open circles show expected values at $t = \pm\infty$. The asymptotic sound speed is set at $a_\infty = 0.148$, for which $R_a/M = 22.7$.

or M. Thus, for example, the accretion rate is proportional to n_∞ and M^2 (see, e.g. Eq. (5.10)), while the 4-velocity u^α as a function of coordinates x^α/M are independent of n_∞ and M. If the asymptotic sound speed is sufficiently low that $a_\infty \ll 1$, then the solution can also be scaled to arbitrary a_∞ or T_∞. However, once a_∞ approaches the speed of light and the transonic radius approaches the horizon, scaling with a_∞ or T_∞ breaks down. This behavior is already evident from the relativistic Bondi solution for accretion onto a single BH.

The emergent electromagnetic luminosity and radiation spectrum also exhibit simple scaling. The form of the scaling relations depend on the temperature and density dependence of the adopted emissivities and will be described later in Sec. 6.1.3 when we treat realistic asymptotic temperatures and sound speeds.

6.1.2 Prototype Cases

Binary Bondi Accretion

The "prototype" calculations provide valuable qualitative insight into the evolution of the accretion flow as the binary separation decreases, passing through the three regimes identified above. For the case of "binary Bondi accretion", in which the gas at infinity is at rest relative to the binary center of mass, we obtain a

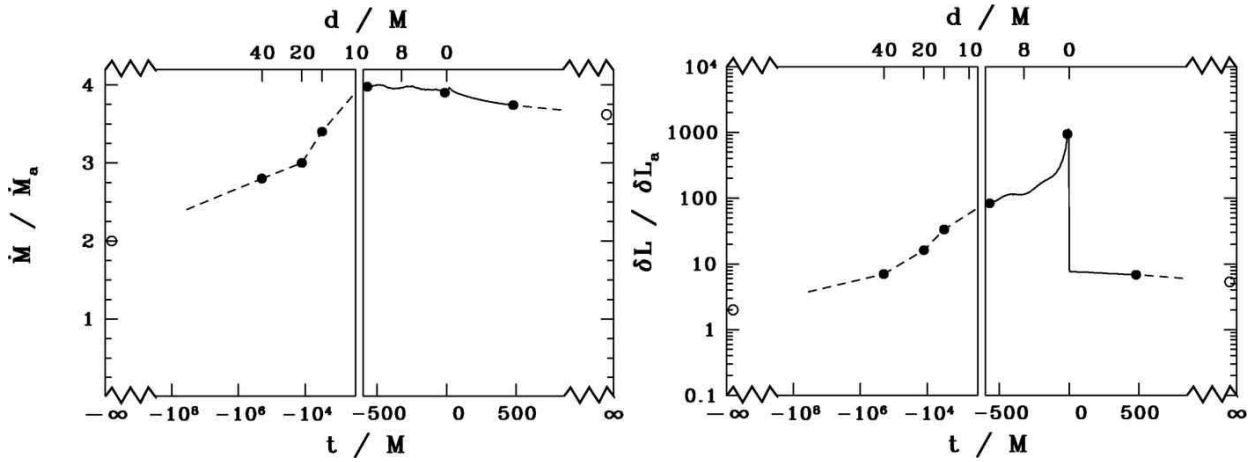

Figure 6.2: Same as Fig. 6.1, but for $\Gamma = 4/3$.

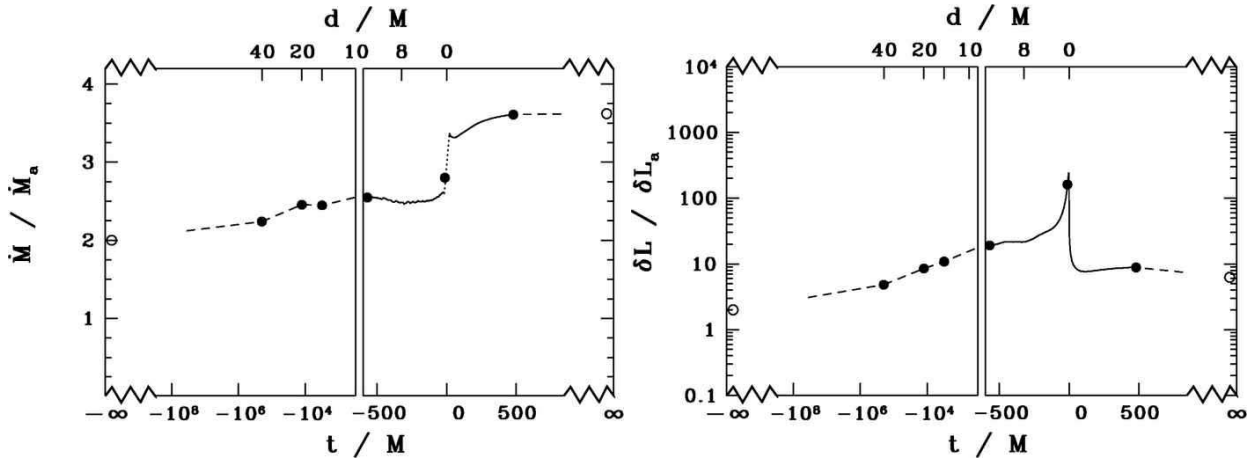

Figure 6.3: Same as Fig. 6.1, but for $\Gamma = 5/3$.

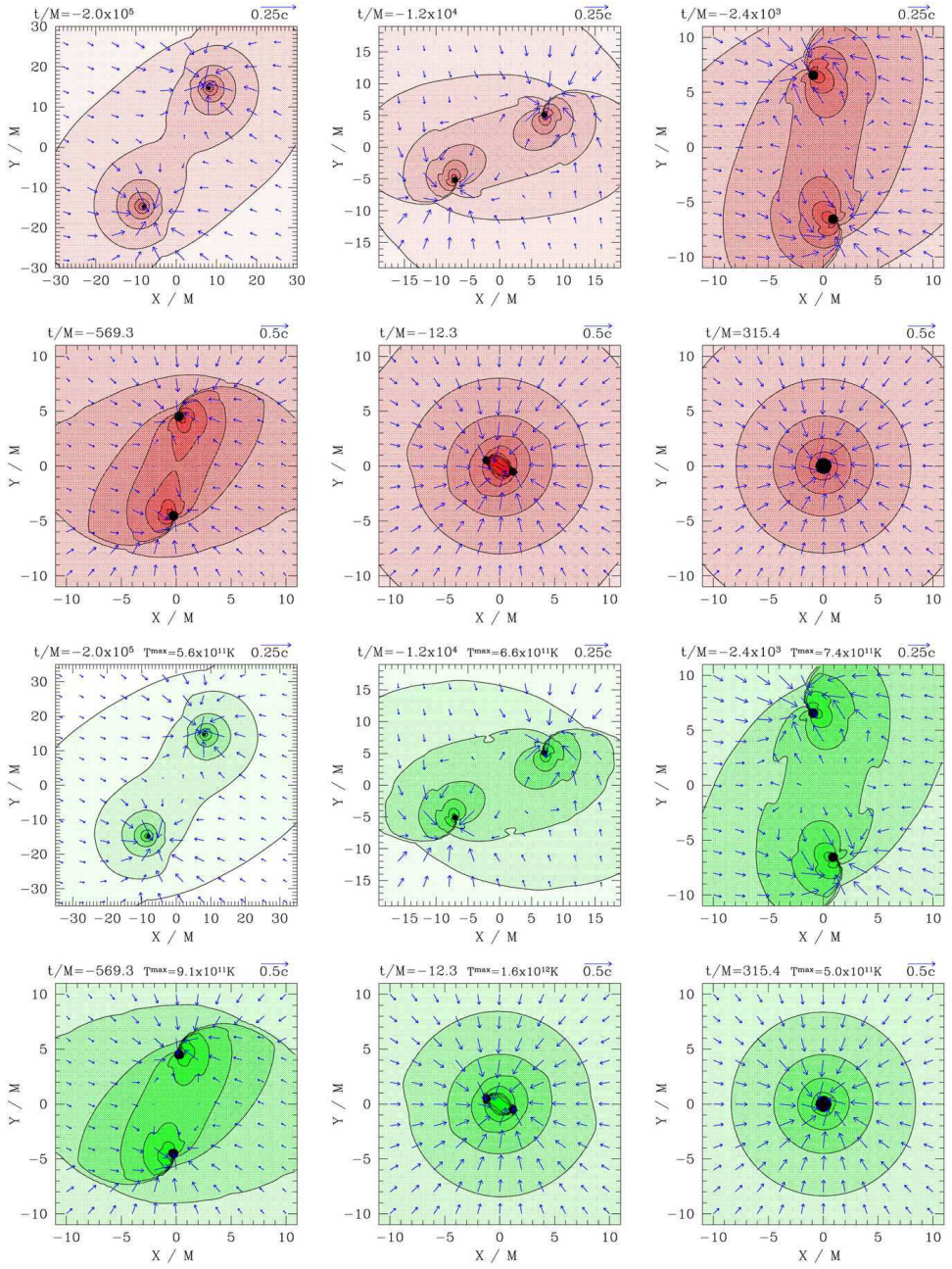

Figure 6.4: Snapshots of rest-mass density ρ_0 and temperature T contours in the orbital plane for the binary Bondi "prototype" case with $\Gamma = 13/9$. First and second rows show density contours and velocity profiles, third and fourth rows show snapshots of temperature T. Density contours are plotted at $\rho_0 = \rho_{0,\infty} 10^{0.25j}$ $(j = 1, 2, ..., 12)$. Temperature contours are plotted at $T = 10^{11+0.125j} K$ $(j = 1, 2, ..., 12)$. Contours of highest density and temperature are near the BHs. Arrows denote velocity vectors. The AH interior is marked by a filled black circle.

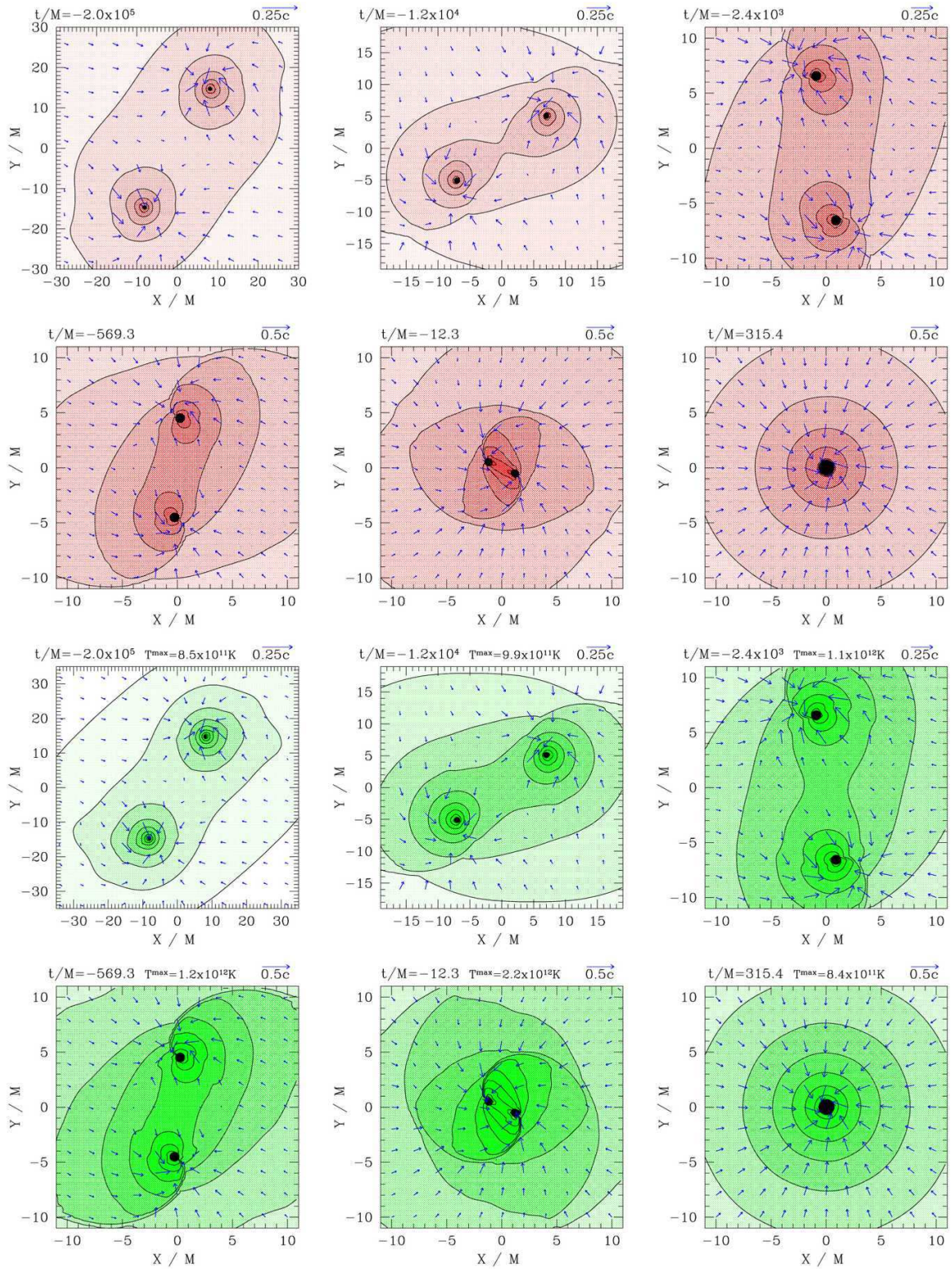

Figure 6.5: Same as Fig. 6.4, but for $\Gamma = 5/3$.

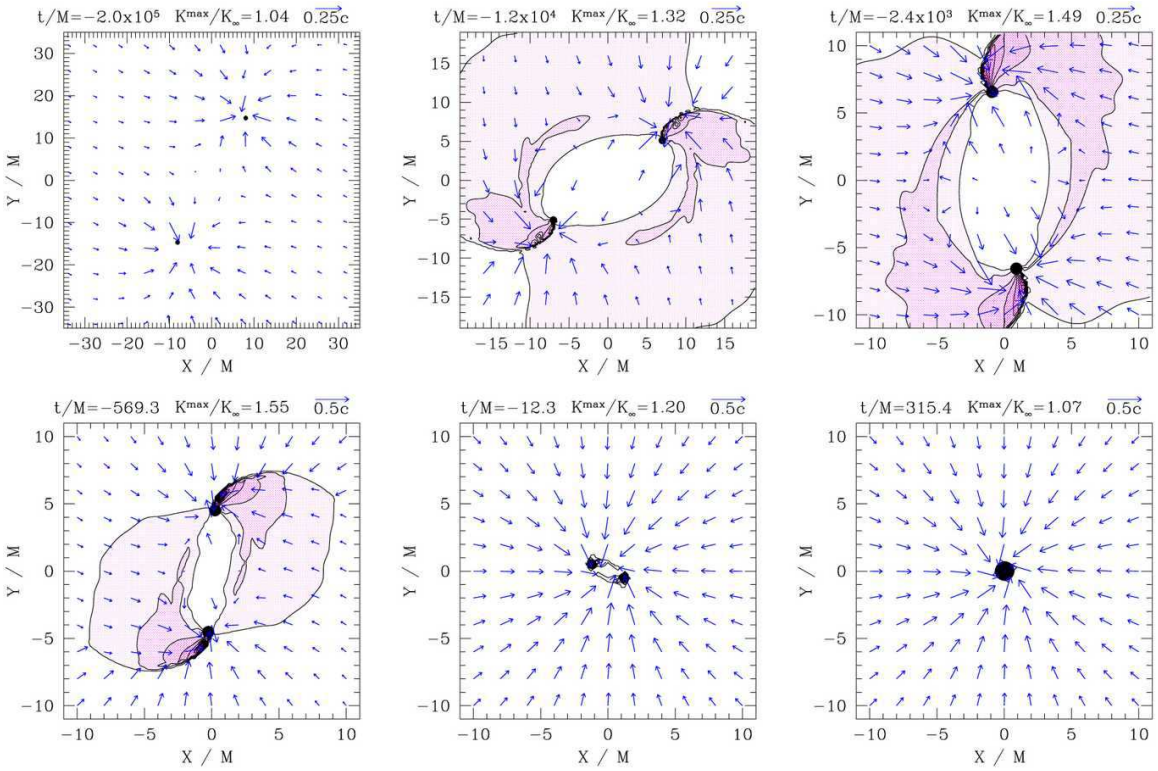

Figure 6.6: Snapshots of K/K_∞ contours in the orbital plane for the binary Bondi "prototype" case with $\Gamma = 13/9$. Contours are drawn for $K/K_\infty = 1 + 0.05j \quad (j = 1, 2, ..., 12)$. Arrows denote velocity vectors. The AH interior is marked by a filled black circle.

sequence of "snapshots" for different binary separations. Each snapshot is generated by evolving the binary long enough to allow the gas to relax to a quasistationary flow, but not long enough for the separation d to change significantly. This occurs at $t \approx 300M$. By sandwiching together snapshots we can trace the evolution in accretion rate $\dot{M}$ and luminosity L as the binary transitions from regime 1 to regime 2. The final transition from regime 2 to regime 3 is captured by a single simulation which follows the binary through inspiral and merger. We perform these simulations for cases PA1 ($\Gamma = 13/9$), PA2 ($\Gamma = 4/3$), and PA3 ($\Gamma = 5/3$) in order to study the effect of the EOS on the evolution (see Table 6.1). Numerical results for all cases are given in Table 6.2 and Table 6.3. The time variations in the accretion rate and total luminosity for these cases are shown in Figs. 6.1–6.3.

The evolution in $\dot{M}$ can be understood as follows. Define $\dot{M}_a$ to be the accretion rate onto a single, isolated BH of mass $M/2$. Then it follows that the total accretion rate onto two infinitely separated BHs of mass $M/2$ will be given by $\dot{M} = 2\dot{M}_a$. However, late in the inspiral, when the separation satisfies $d \ll R_a$, the binary can be treated as a single gravitating object. From Eq. (5.10) we see the accretion rate is proportional to M^2, so we expect that the accretion rate will approach $\dot{M} = 4\dot{M}_a$. During the final stage of the inspiral, mass-energy is radiated away in the form of gravitational waves. Thus we expect that the final post-merger accretion rate will be approximately given by $\dot{M} = 4\dot{M}_a(1 - \delta M/M)^2$. In our simulations, we find $\delta M/M \approx 0.05$, consistent with the values reported in [92]. We observe the expected behavior for both our PA1 (see Fig. 6.1) and PA2 (see Fig. 6.2) runs. For PA3, the accretion rate never reaches $4\dot{M}_a$ before the merger. We attribute this to the fact that for $\Gamma = 5/3$, gas is more efficiently heated, allowing $P \sim \rho_0 v^2$ and $a \sim v$, even in the absence of shocks. When shocks do form, the flow is much more easily disrupted as the kinetic energy of the flow does not dominate the thermal energy, contrary to cases PA1 and PA2. Thus, some matter is swept away from the vicinity of the binary, causing a lowering of the accretion rate (see Fig. 6.3). We note, however, that after the merger when the shocks have a chance to dissipate, the accretion rate does settle to its expected value, taking mass loss into account.

We also plot the luminosity enhancement due to bremsstrahlung and synchrotron emission in Figs. 6.1–6.3. Because the high-temperature homogeneous background gas in our prototype simulations has an intrinsic, nonnegligible emissivity, we subtract it from the total luminosity measured. We define $\delta L \equiv L - L_{bg}$, where L_{bg} is the background luminosity which would be present in our computational domain for a homogeneous gas cloud of density $\rho_{0,\infty}$ and temperature T_∞, with no BH present. We normalize δL by δL_a, which we define as the luminosity above background which would be present for a single, isolated BH of mass $M/2$. If we take the limit in which the binary separation $d \to \infty$, we expect that $\delta L/\delta L_a \to 2$. This limiting value is indicated by the open circle at $t/M = -\infty$ in Figs. 6.1–6.3. We also calculate the expected value of $\delta L/\delta L_a$

for a single BH of mass $M - \delta M$ and plot it for reference with an open circle at $t/M = +\infty$. We see that for each Γ the luminosity enhancement increases by several orders of magnitude over the course of the inspiral. While the numerical value of this variation is not physically meaningful due to the unrealistic temperatures used in these "prototype" calculations, this behavior provides strong qualitative evidence of a significant enhancement in luminosity that can be expected to accompany such an inspiral. Mergers in realistic clouds, yielding realistic luminosities whose values are physically meaningful, will be treated in Sec. 6.1.3.

Figures 6.4 and 6.5 show snapshots of density and temperature contours for cases PA1 and PA3. We do not show snapshots for the PA2 case because they look very similar to the PA1 case. We can see that in the early phases of the inspiral, the accretion flow resembles two independent spherical Bondi flows. As the separation decreases and becomes comparable to the transonic radius, the orbital velocity of each BH becomes comparable to the sound speed. Within R_a shocks begin to form, which grow in strength until the merger. It is the heating from these shocks which contributes to the dramatic increase in the luminosity observed. Note that the final accretion flow near the BH is not spherically symmetric due to the spin of the merged BH. The BH spin does not significantly change the final accretion rate predicted by Eq. (5.10), as this quantity is determined by gas parameters at $r \sim R_a \gg M$, where the effect of the BH spin is negligible. This result conforms with the findings of [109].

In order to highlight the role that shock heating plays during phases 2 and 3 of the merger, we also present contours of K/K_∞ for our PA1 case (see Fig. 6.6). Here $K \equiv P/\rho_0^\Gamma$ and K_∞ is the value of K at infinity. Because $K/K_\infty = 1$ everywhere for adiabatic flow in the absence of shocks, this quantity serves as a useful tracer for the amount of shock heating which is taking place. The quantity $K = K(s)$, where s is the gas entropy, and is constant in the absence of shocks; shock heating yields $K/K_\infty > 1$ (see Appendix B of [104]). As expected, we see that K/K_∞ increases steeply near the shock front. For each snapshot, we compute the maximum value of K/K_∞ outside the horizon. We find that K_{max}/K_∞ initially increases as the separation decreases and shocks become stronger, as expected. This trend terminates in the very late stage of the merger, when $d \sim 5M \sim d_{ISCO}$ [110]. This is likely due to the fact that kinetic energy dissipated as heat is confined to a small region and is being quickly consumed by the BHs at this stage. After the merger, the gas relaxes to laminar spherical Bondi flow and K/K_∞ returns to unity everywhere.

Binary Bondi-Hoyle-Lyttleton Accretion

In order to investigate additional electromagnetic signatures which may be present due to the motion of the binary relative to the cloud, we have performed a series of "prototype" simulations of BHL accretion onto merging binaries. We consider both subsonic cases ($V_\infty/a_\infty = 0.7$) and supersonic cases ($V_\infty/a_\infty = 2.7$).

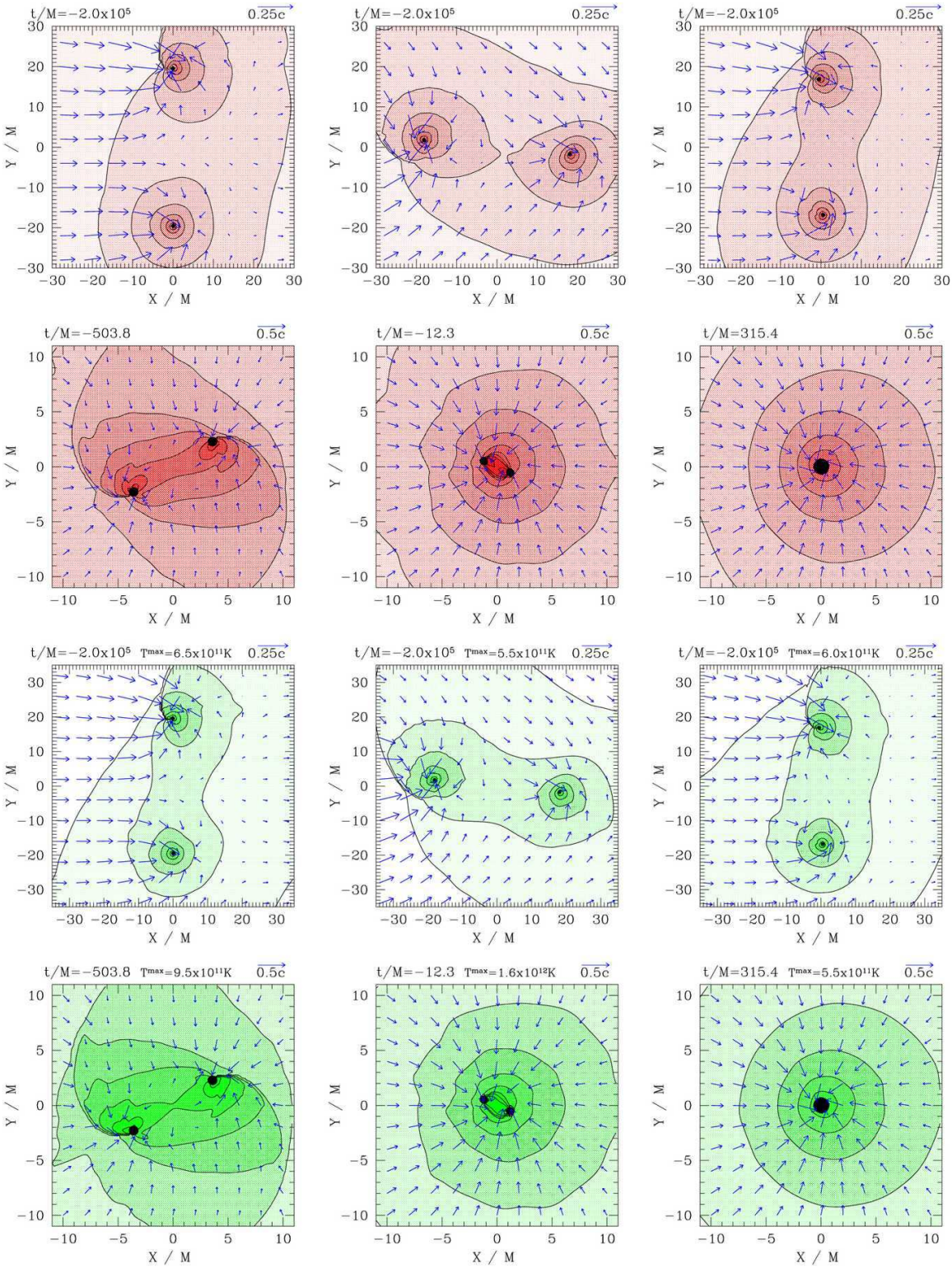

Figure 6.7: Same as Fig. 6.4, but for subsonic BHL accretion with $\Gamma = 13/9$ and $V_\infty = 0.1$. The asymptotic velocity V_∞ is in the $+\hat{x}$ direction.

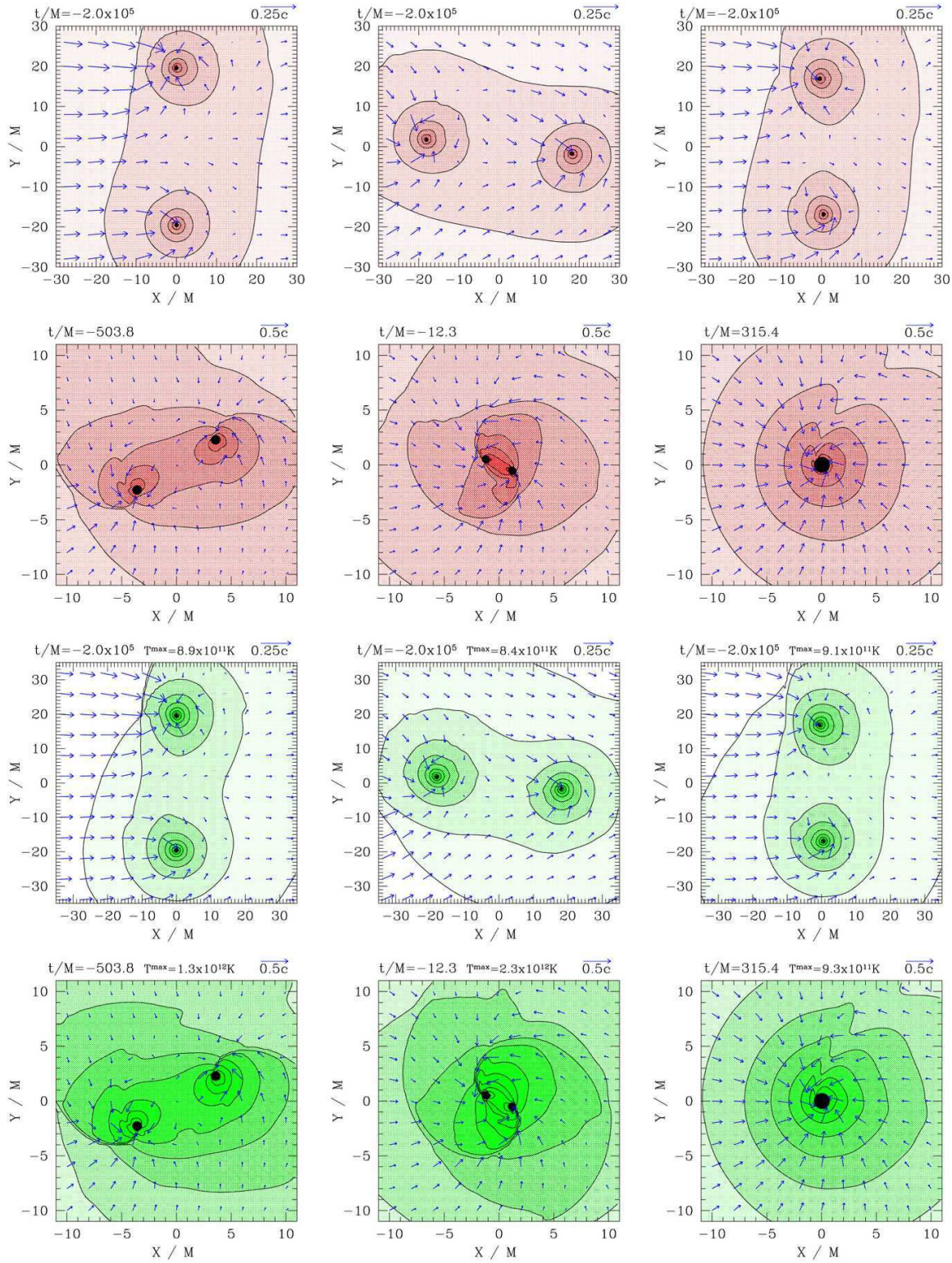

Figure 6.8: Same as Fig. 6.4, but for subsonic BHL accretion with $\Gamma = 5/3$ and $V_\infty = 0.1$. The asymptotic velocity V_∞ is in the $+\hat{x}$ direction.

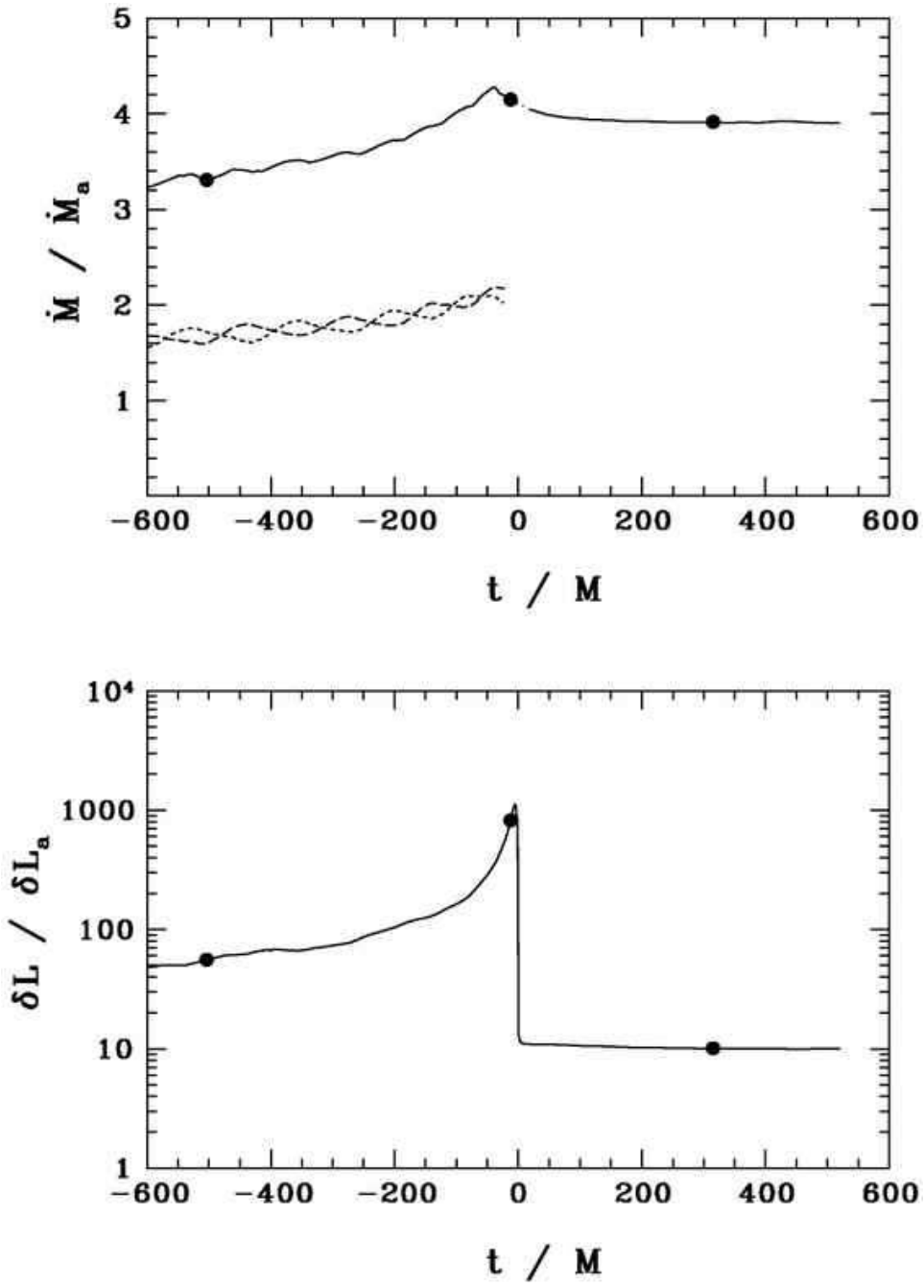

Figure 6.9: Time evolution of $\dot{M}$ and δL for binary BHL inspirals with $\Gamma = 13/9$, $a_\infty = 0.148$, and $V_\infty = 0.1$. The initial binary separation is $d = 10M$ and the BHs evolve to merger. $\dot{M}_a$ and δL_a are the accretion rate and luminosity enhancement over the background for a single isolated black hole with mass equal to the initial ADM mass of the binary. Dashed lines in $\dot{M}$ plot represent accretion rates onto individual BHs, the solid line represents the total accretion rate. Dots represent the times highlighted in the last three snapshots in Fig. 6.7.

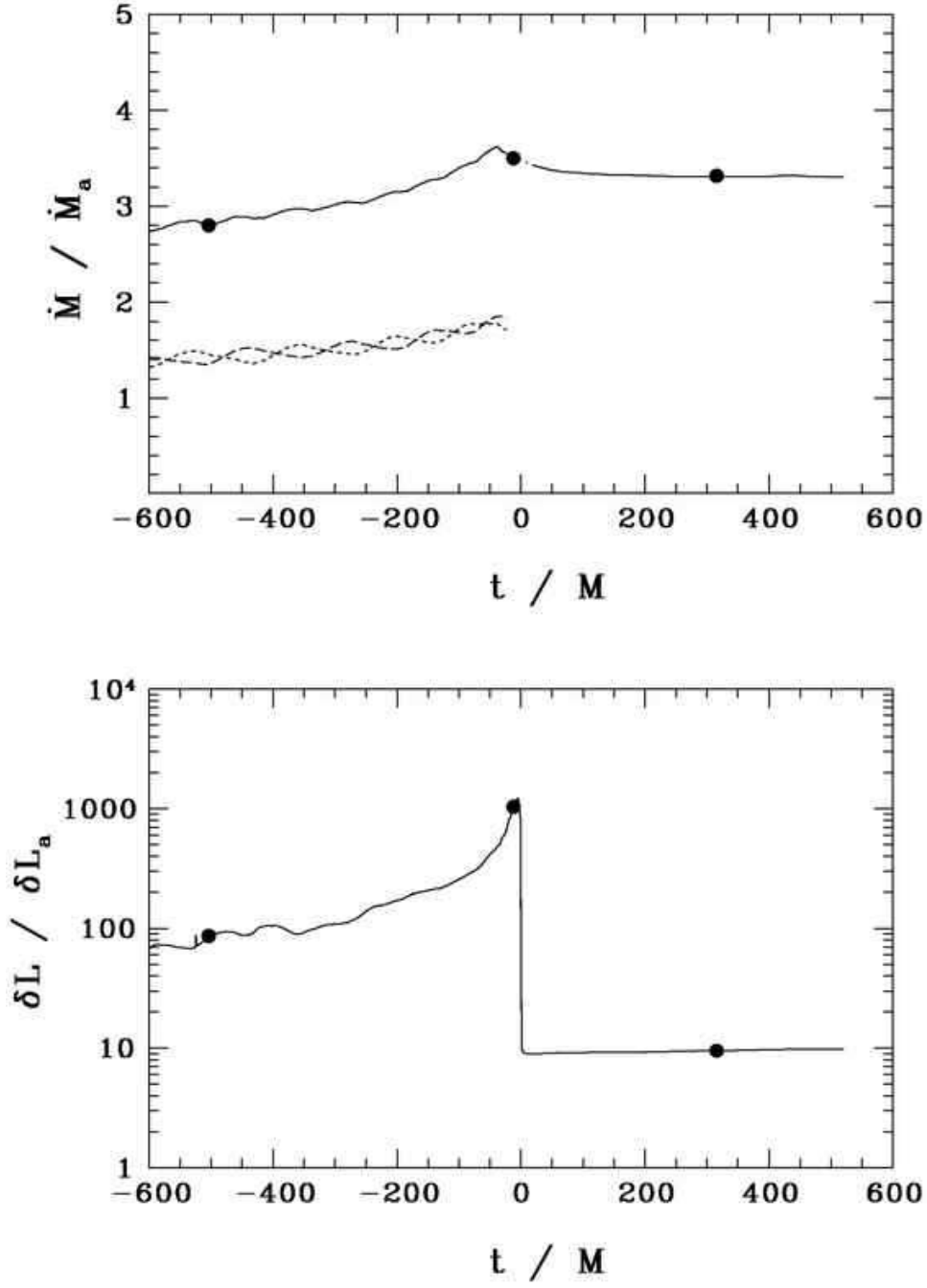

Figure 6.10: Same as Fig. 6.9, but for $\Gamma = 4/3$.

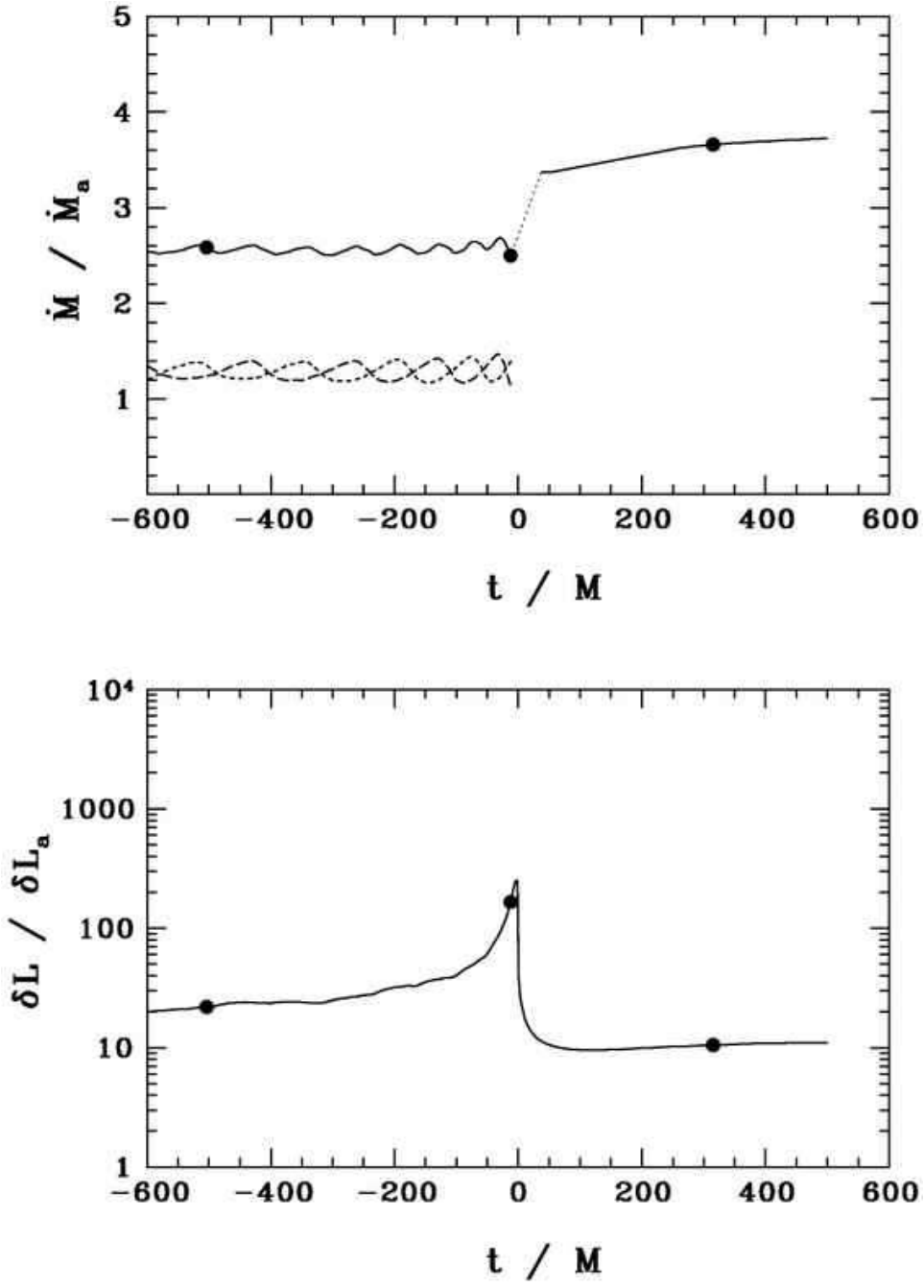

Figure 6.11: Same as Fig. 6.9, but for $\Gamma = 5/3$.

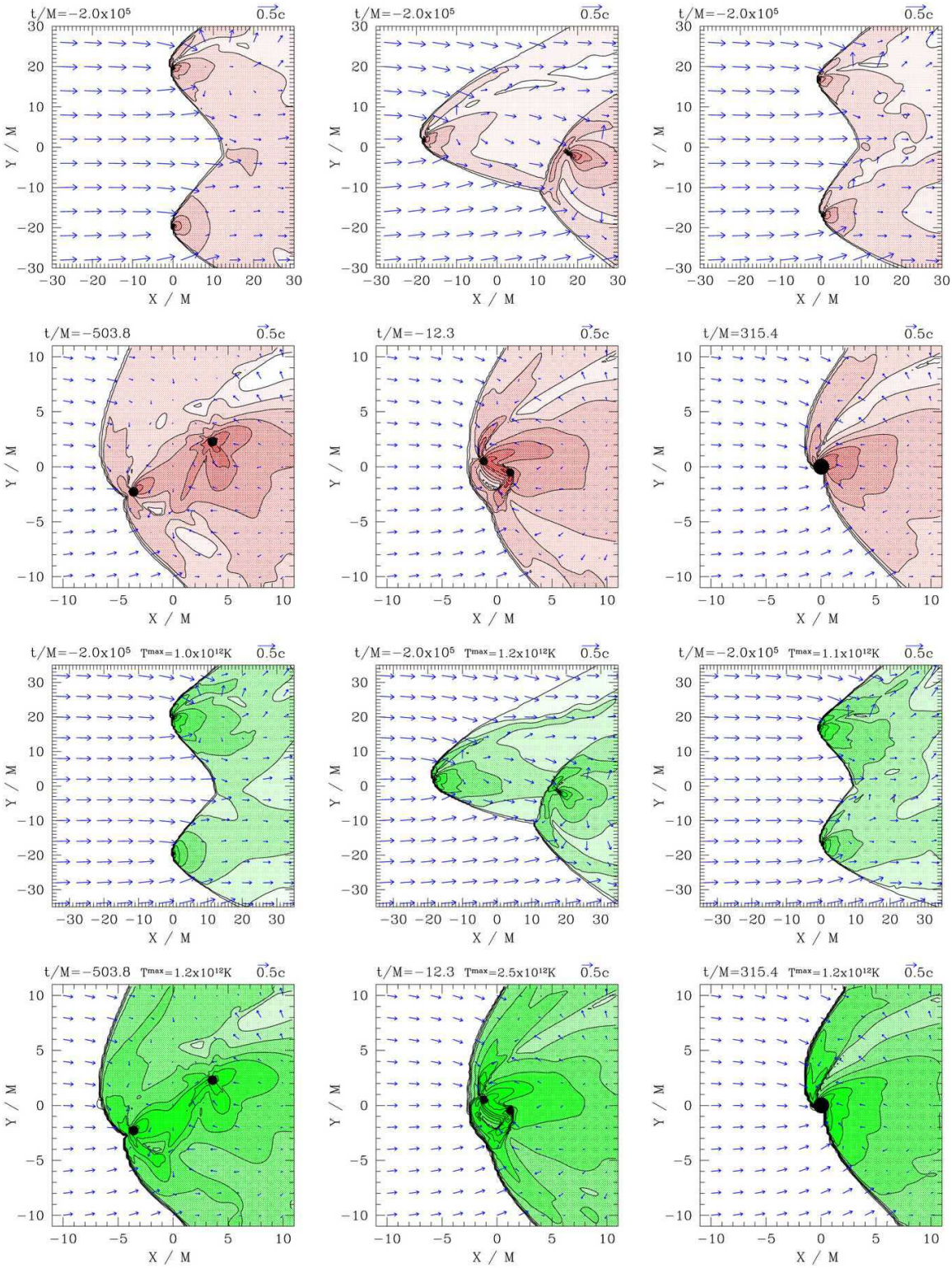

Figure 6.12: Same as Fig. 6.4, but for subsonic BHL accretion with $\Gamma = 13/9$ and $V_\infty = 0.4$. The asymptotic velocity V_∞ is in the $+\hat{x}$ direction.

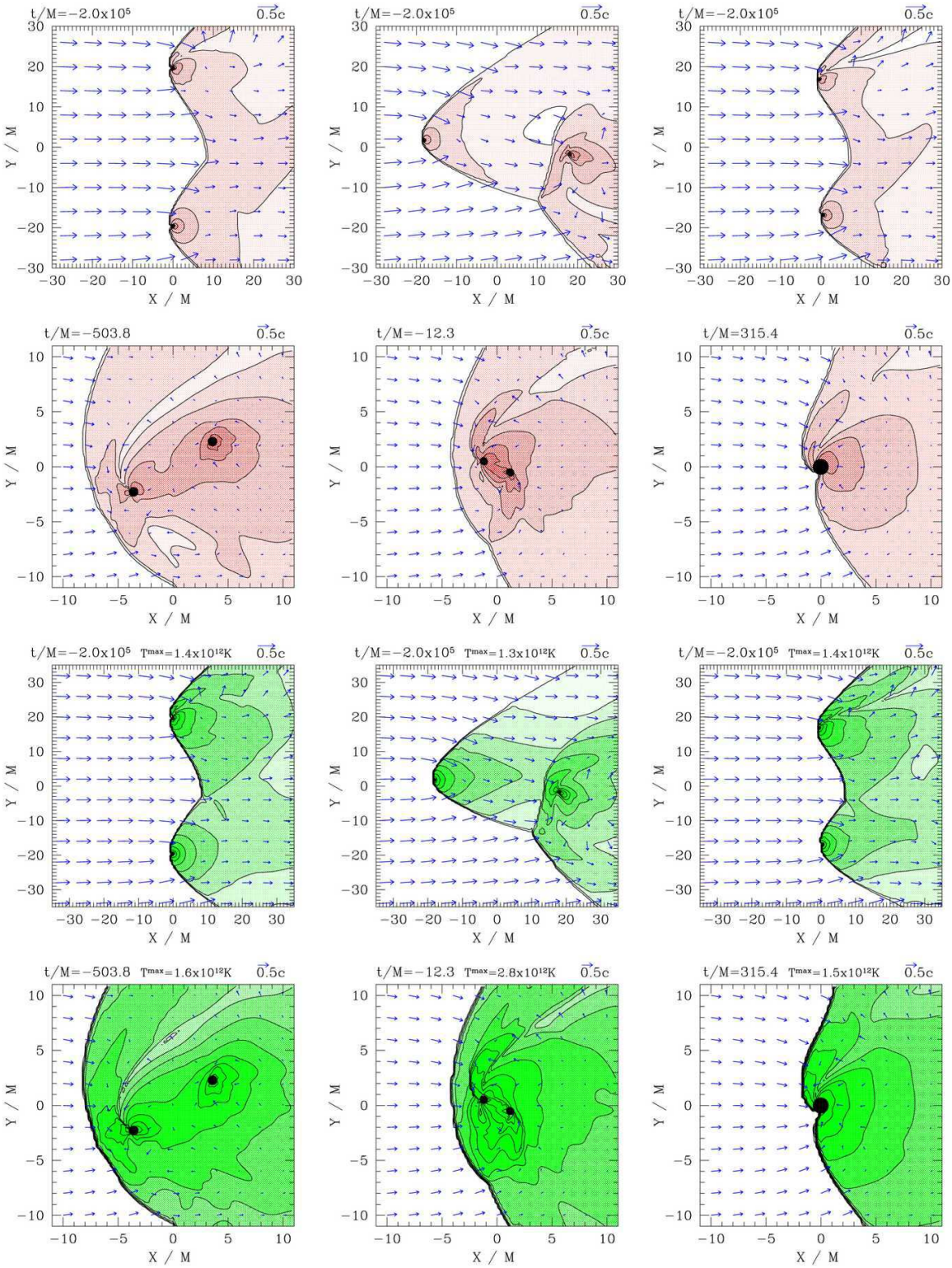

Figure 6.13: Same as Fig. 6.4, but for subsonic BHL accretion with $\Gamma = 5/3$ and $V_\infty = 0.4$. The asymptotic velocity V_∞ is in the $+\hat{x}$ direction.

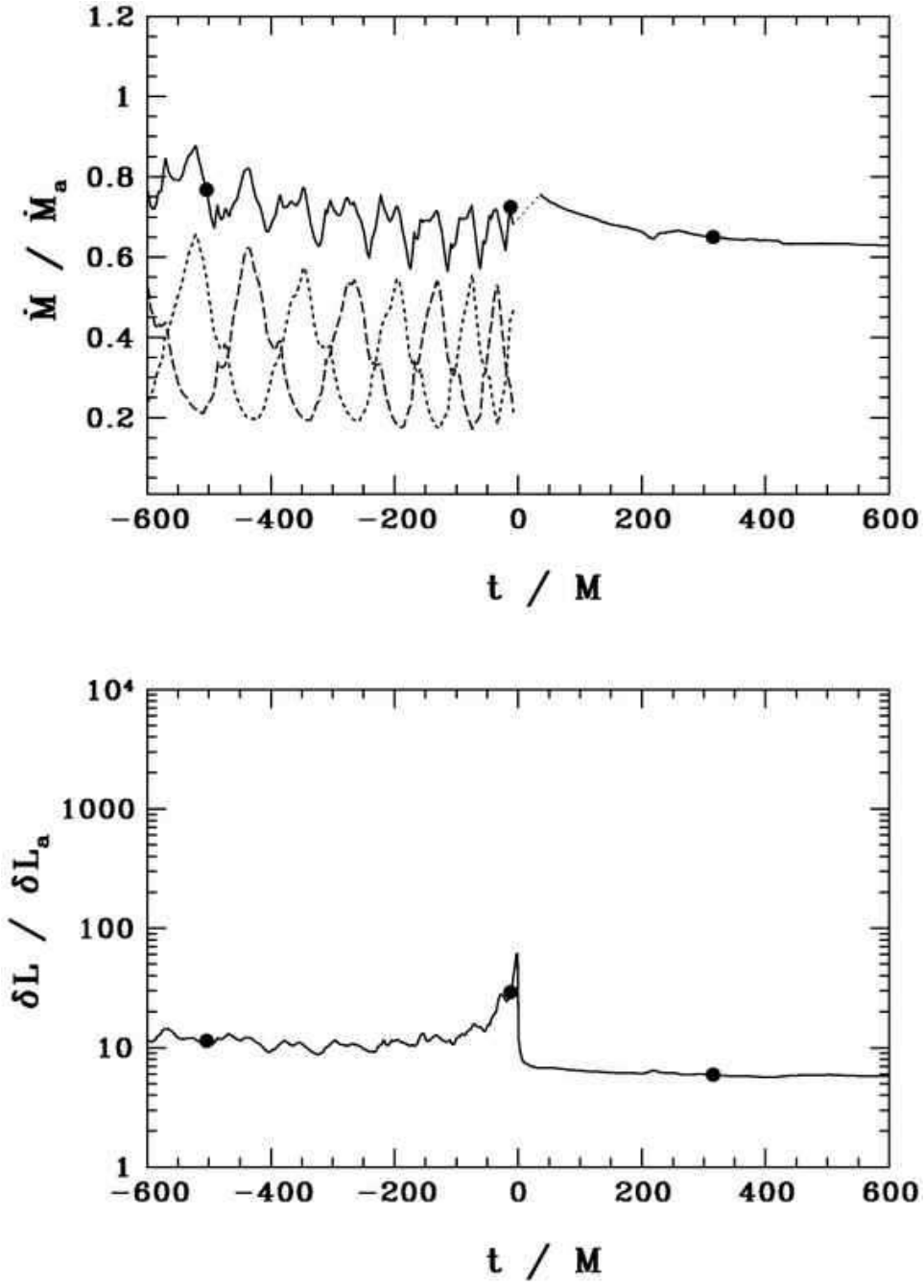

Figure 6.14: Same as Fig. 6.9, but for $\Gamma = 13/9$, $V_\infty = 0.4$.

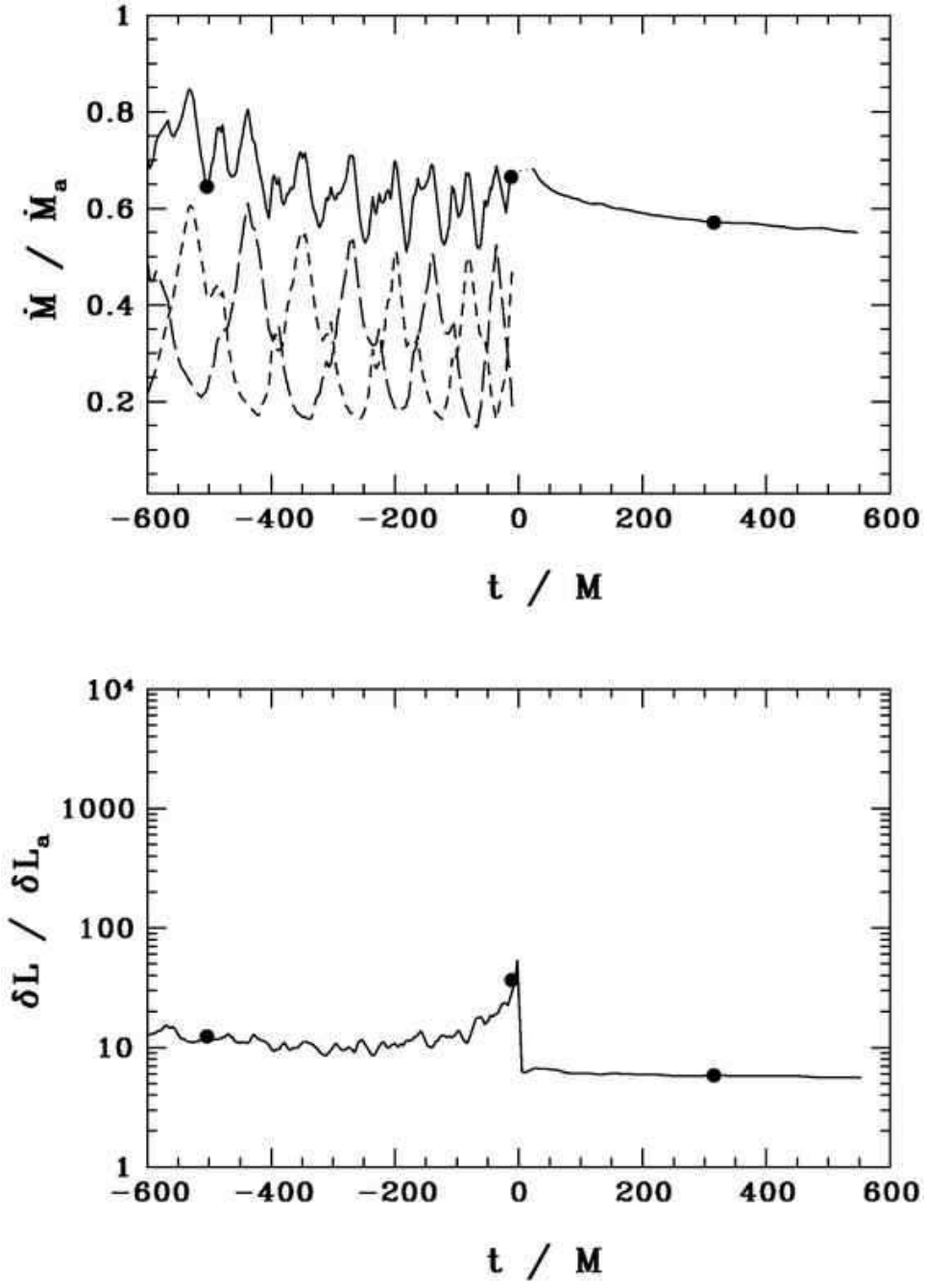

Figure 6.15: Same as Fig. 6.9, but for $\Gamma = 4/3$, $V_\infty = 0.4$.

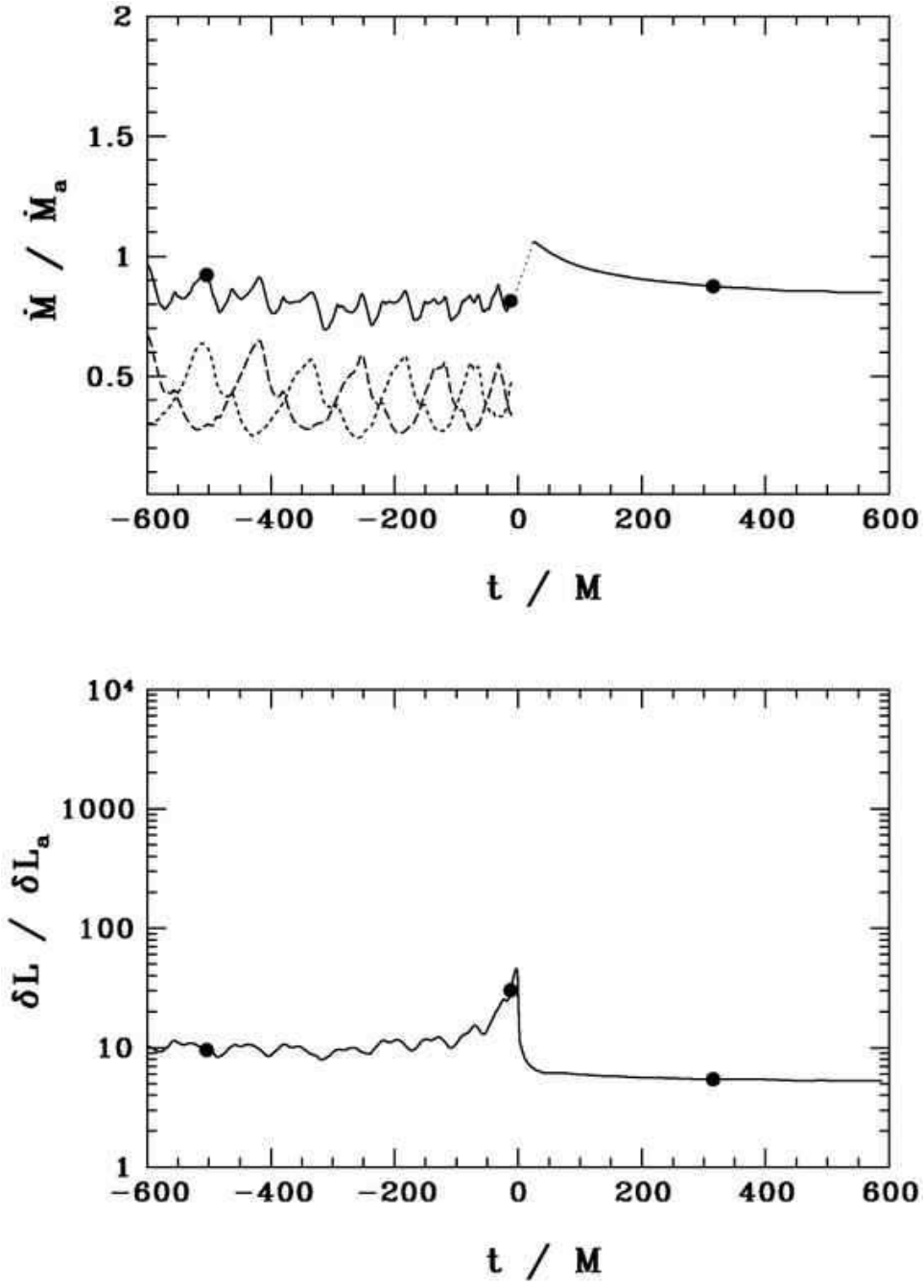

Figure 6.16: Same as Fig. 6.9, but for $\Gamma = 5/3$, $V_\infty = 0.4$.

We again consider $\Gamma = 13/9$ (PB1 and PC1), $\Gamma = 4/3$ (PB2 and PC2), and $\Gamma = 5/3$ (PB3 and PC3) in order to assess the influence of the EOS on the flow. We perform both wide separation runs ($d = 40M$) to produce snapshots that are quasistationary in the corotating frame of the binary, as well as close separation runs ($d = 10M$) in which we evolve the binary from inspiral to merger. While the angle between the binary trajectory and the orbital plane can be chosen arbitrarily, we restrict our attention to cases in which the binary trajectory lies in the orbital plane.

For our (asymptotically) subsonic cases, the departures from the binary Bondi case are subtle. Figures 6.7 and 6.8 show snapshots of density and velocity field for cases PB1 and PB3. Snapshots for case PB2 are similar to PB1 and hence are now shown here. At wide separation $d = 40M$, we see an asymmetry in the accretion flow for cases PB1 and PB2, as shocks develop around one BH as it moves against the flow of the gas, but not around the other as it moves in the same direction as the flow. This phenomenon continues up to the merger. At this separation the orbital Keplerian velocity is $V_k \approx 0.08$. Thus, these shocks are formed when one BH moves supersonically against the flow of the gas and $(V_k + V_\infty)/a \gtrsim 1$. The reason that this behavior is not seen in case PB3 is that the gas is adiabatically heated more efficiently for $\Gamma = 5/3$ as it flows toward the BHs, causing the sound speed of the gas to be greater near each BH. We find that for $\Gamma = 5/3$, $(V_k + V_\infty)/a < 1$ near the black hole, preventing any shocks from forming. The post-merger accretion flow exhibits some departure from spherical symmetry due to BH spin and $V_\infty \neq 0$, but all shocks dissipate. In Figs. 6.9–6.11, we once again observe an increase in accretion rate and luminosity over the course of the merger. We have also plotted in these figures the individual accretion rates onto each BH in order to demonstrate the effect of the binary motion relative to the wind.

For our supersonic cases (PC1-PC3), the departure from the binary Bondi case is more dramatic. When the BHs are widely separated ($d > R_a$), a bow shock forms around each individual BH, as seen in Figs. 6.12 and 6.13. Late in the inspiral, when $d < R_a$, these shocks merge and form a single bow shock surrounding the binary, which persists after the merger. The final flow resembles the solution found by [68] for steady accretion onto a moving BH with $V_\infty/a_\infty = 2.5$, although in our case the remnant is spinning. During the inspiral, the modulation in $\dot{M}$ and δL is more pronounced than in the subsonic case (see Figs. 6.14–6.16).

6.1.3 Realistic Binary Bondi accretion

While the high temperature prototype runs give us valuable insight into the general nature and different phases of the accretion flows onto inspiralling BHBH binary systems in gas clouds, we require simulations with more realistic gas temperatures in order to identify observational signatures. Accordingly, we have performed simulations of the binary Bondi problem for a gas cloud with asymptotic density $n_\infty = 10$ cm^{-3}

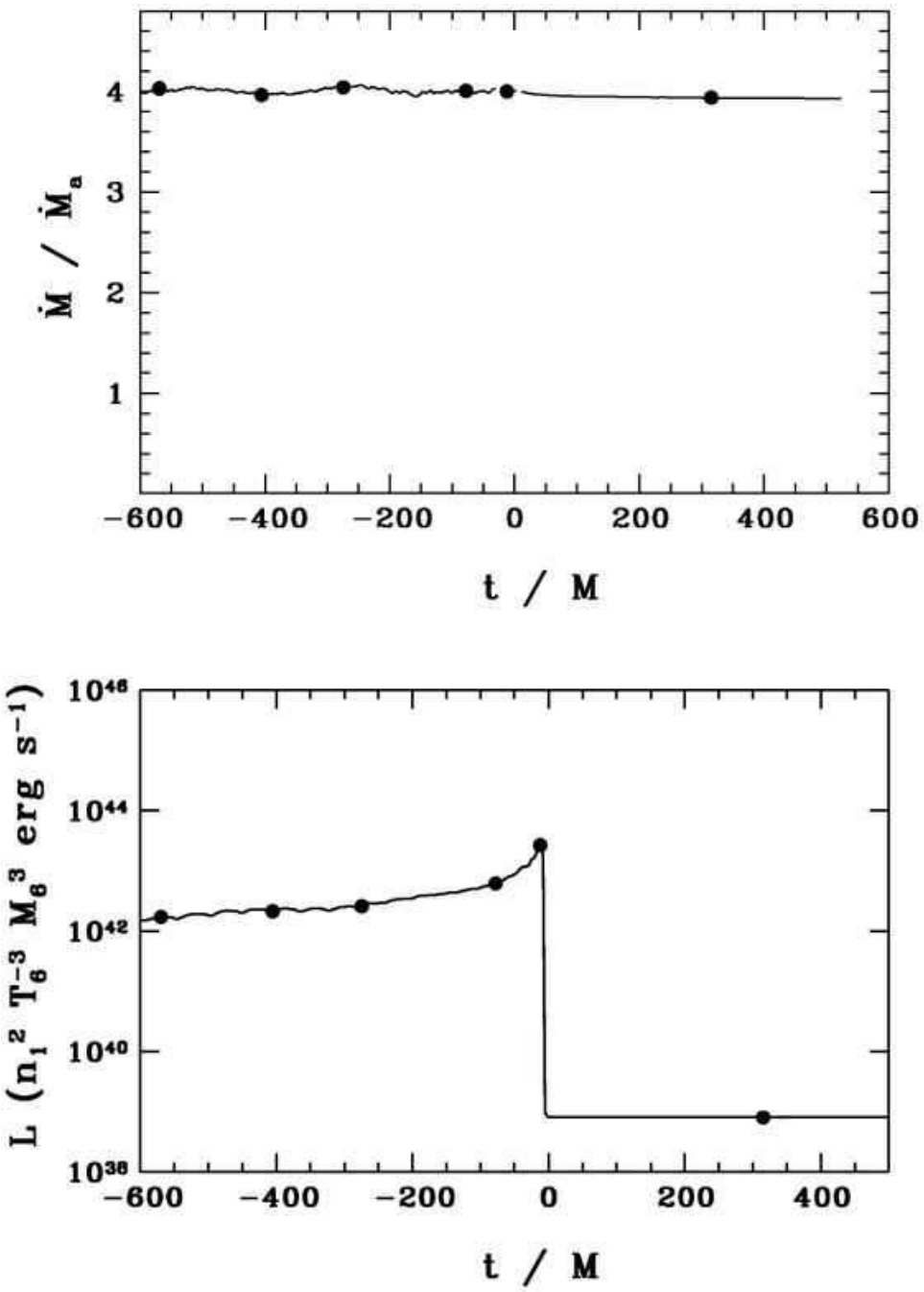

Figure 6.17: Plots showing time evolution of $\dot{M}$ and $\dot{L}$. Here time is measured relative to the time at which the merger occurs. Asymptotic temperature is $T = 10^6 K$. Adiabatic index given by $\Gamma = \Gamma^*$. $n_1 \equiv n_\infty/10\text{cm}^{-3}$, $T_6 \equiv T_\infty/10^6 K$, $M_6 \equiv M/10^6 M_\odot$.

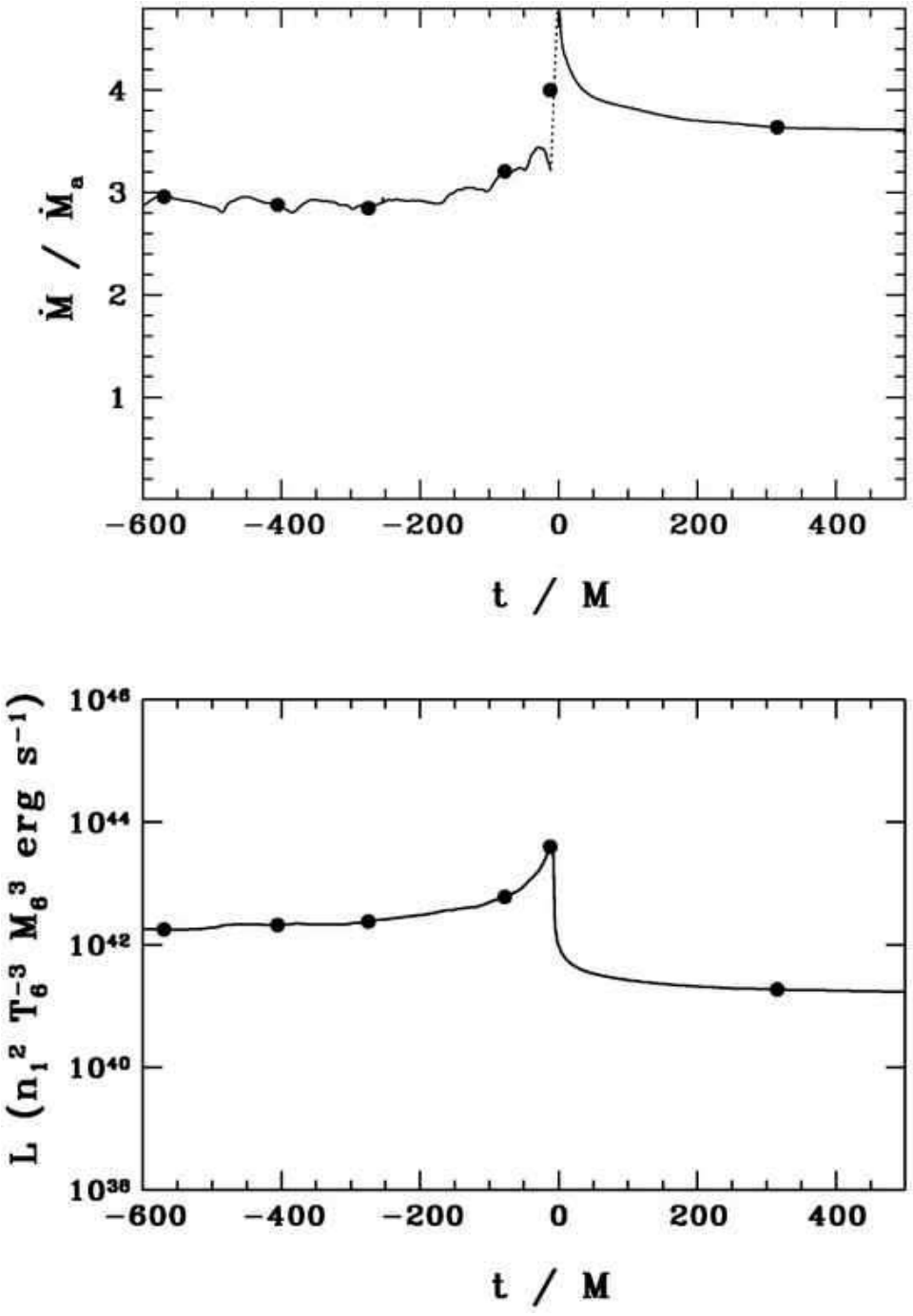

Figure 6.18: Same as Fig. 6.17, but for $\Gamma = 5/3$.

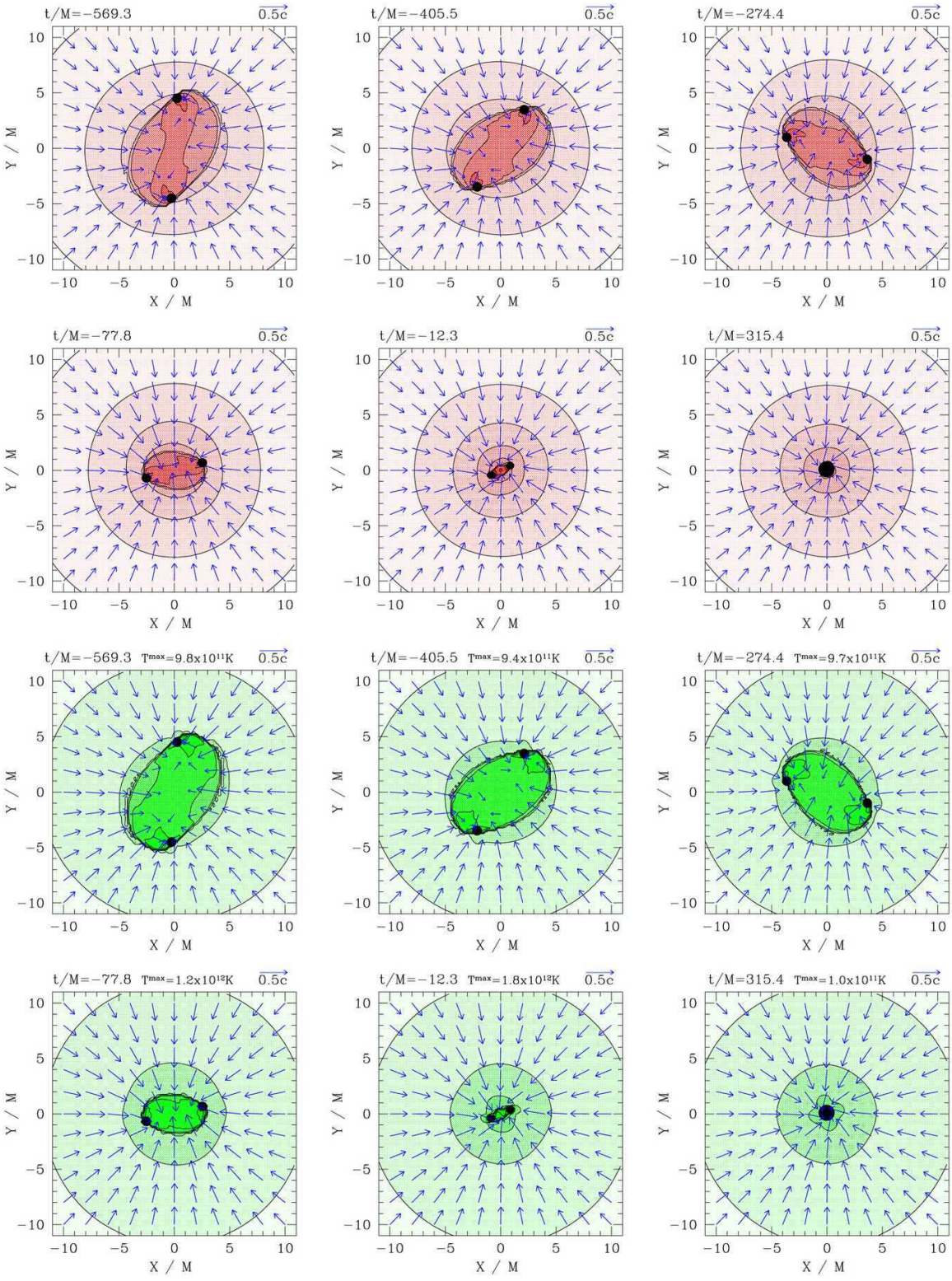

Figure 6.19: Snapshots of rest-mass density ρ_0 and temperature T contours for the $\Gamma = \Gamma^*$ case. First and second rows show snapshots of density contours and velocity profiles in the orbital plane. Third and fourth rows show snapshots of T. Density is plotted according to $\rho = \rho_{0,\infty} 10^{7+0.33j}$ $(j = 1, 2, ..., 12)$. Temperature contours are plotted according to $T = 10^{10+0.25j} K$ $(j = 1, 2, ..., 12)$. Arrows represent the velocity field in the given plane.

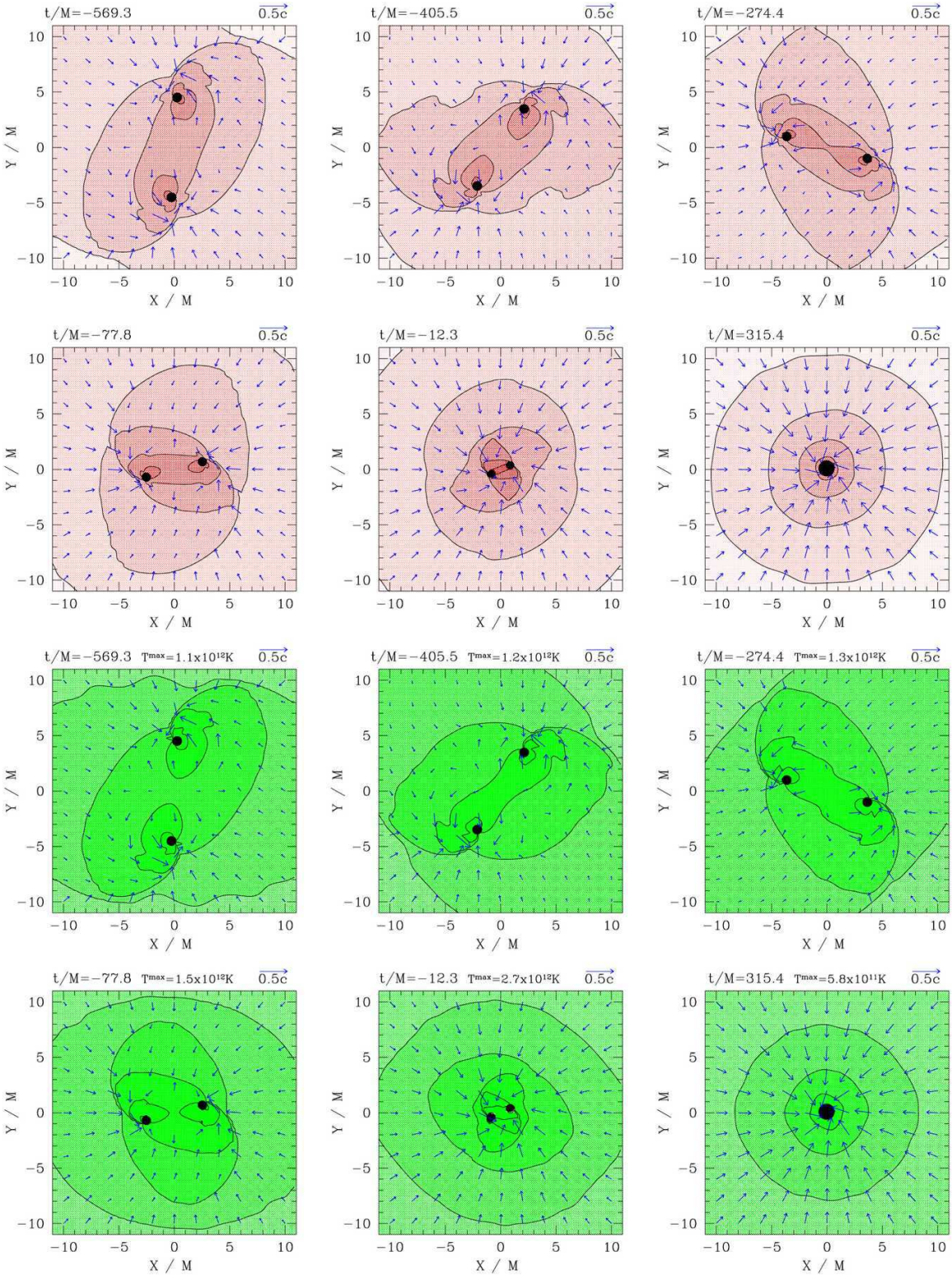

Figure 6.20: Same as Fig. 6.19 but for $\Gamma = 5/3$.

and temperature $T = 10^6 K$. This choice is consistent with the proposed "cooling flow model of quasar fueling" describing the hot interstellar gas found in galaxies [6, 61]. As mentioned previously, computational limitations demand that our outer boundary be placed inside the transonic radius for these simulations. As a result, we focus only on the final phase of the inspiral and merger, in which $d \ll R_a$. We use both a $\Gamma = \Gamma^*$ (case RA1) and $\Gamma = 5/3$ (case RA2) EOS. As explained in Sec. 5.1, we still set $\Gamma = 13/9$ in the computational domain for the $\Gamma = \Gamma^*$ case since the $\Gamma = 5/3$ and transition region is outside our computational domain. However, the initial hydrodynamic profile of the flow is very different from a pure $\Gamma = 13/9$ EOS with the same asymptotic temperature. We focus here on the BHBH Bondi problem only ($V_\infty = 0$), and postpone a study of binary BHL accretion in a realistic gas cloud for a later analysis. As in the prototype calculations, we find evidence for a strong enhancement in the luminosity due to shock heating of the gas (see Fig. 6.17 and Fig. 6.18). For these runs, we plot the luminosities in cgs units.

We note that for case RA1, strong shocks form, but are confined to the immediate vicinity of the binary. This is because the inward gas flow onto the binary is strongly supersonic, making it difficult for shocks to propagate outward (see Fig. 6.19). For case RA2, on the other hand, the radial component of the 4-velocity $u \sim a$ everywhere, making it much easier for shocks to spread outward, as seen in Fig. 6.20.

6.1.4 Scaling and Detectability

All of our quoted results for the accretion rate $\dot{M}$ are normalized by the value for a single black hole of mass $M/2$ undergoing stationary, spherical Bondi accretion. Using Eq. (5.10) we see that this quantity scales with asymptotic temperature and density according to

$$\dot{M}_a c^2 = 4.6 \times 10^{40}\ \lambda_{5/3}\ n_1\ T_6^{-3/2}\ M_6^2\ \mathrm{erg\ s^{-1}}\ , \tag{6.1}$$

where we define $\lambda_{5/3} \equiv \lambda(\Gamma, a_\infty)/\lambda(5/3, a_\infty)$, $n_1 \equiv n_\infty/10\mathrm{cm}^{-3}$, $T_6 \equiv T_\infty/10^6 K$, and $M_6 \equiv M/10^6 M_\odot$. Recall that in the Newtonian limit, when $R_a \gg M$, λ depends only on Γ.

It is also possible to derive simple scaling relations for the luminosities. In each of our simulations, most of the electromagnetic luminosity is generated near the horizons of the BHs, as the temperature and density both rise sharply when approaching the horizon, and achieve their maximum values there. By examining Eqs. (D.1)–(D.5) (ignoring the logarithmic terms), and Eq. (D.18), we see that in the high temperature limit ($kT > m_e c^2$), which applies near the horizon in all of our simulations, the bremsstrahlung and synchrotron

emissivities depend on the density and temperature according to,

$$q_{ff} \propto n_h^2 T_h \tag{6.2}$$

$$q_{syn} \propto n_h^2 T_h^3 \beta^{-1} \tag{6.3}$$

Here n_h and T_h refer to the density and temperature at the horizon, respectively. Integrating Eqs. (6.2) and (6.3), we find

$$L_{ff} \approx \int dV q_{ff} \propto n_h^2 T_h M^3 \tag{6.4}$$

$$L_{syn} \approx \int dV q_{syn} \propto n_h^2 T_h^3 \beta^{-1} M^3 \ , \tag{6.5}$$

where we have assumed that most of the (high-energy) radiation is generated near the horizon and hence the radiative volume scales as M^3. To estimate n_h, we use the fact that $r_h \ll R_a$, and so the fluid 4-velocity is approximately given by its free-fall value

$$\hat{u} \approx \left(\frac{2M}{r_h}\right)^{1/2} \ . \tag{6.6}$$

Substituting this into Eq. (3.12) and Eq. (5.10), we find that

$$\frac{n_h}{n_\infty} \sim \left(\frac{R_a}{r_h}\right)^{3/2} \propto \left(\frac{kT_\infty}{m_B c^2}\right)^{-3/2} \tag{6.7}$$

Here we have used $a^2 \approx \Gamma P/\rho_0 = 2\Gamma kT/m_B c^2$. This scaling should remain reasonably accurate, even in the presence of strong shocks, as the shocks cause density enhancements of $\lesssim (\Gamma+1)/(\Gamma-1)$ (see Sec. 89 of [111]), which is of order unity.

The temperature at the horizon T_h, on the other hand, will be strongly affected by the presence of shocks. The gas in any shocked region will be heated to $kT \sim m_B v^2$. Since $v \lesssim c$ near the horizon, shock heating guarantees that $kT_h \lesssim m_B c^2 \sim 10^{13}$ K *independant* of the gas temperature at infinity T_∞. This result has important consequences for the scaling of the maximum luminosities. Once the shock-heated gas is accreted following the merger, T_h drops below this value for all $\Gamma < 5/3$ (see e.g. Fig 5.1) and the luminosity settles down to a value below the maximum.

Even in the absence of shocks, $kT_h \lesssim m_B c^2$ for $\Gamma = 5/3$. This is because for this particular EOS, an appreciable fraction of the gravitational potential energy is converted into thermal energy (both scale as r^{-1} inside R_a: $kT \sim M m_B/r$) [65]. For $\Gamma = \Gamma^*$, it can be shown that the temperature at the horizon for

spherical Bondi flow is approximately given by [65]

$$kT_h \approx \frac{2}{3}\left(\frac{9}{80}\right)^{2/3}\left(\frac{m_e}{m_B}\right)^{1/3} m_B c^2 = 0.013\ m_B c^2 \tag{6.8}$$

Thus, we find that the temperature at the horizon, T_h is independent of gas parameters at infinity for both $\Gamma = 5/3$ and $\Gamma = \Gamma^*$. However, for $\Gamma = \text{const} < 5/3$, T_h does exhibit scaling with T_∞ in the absence of shocks. In this case, $P = K\rho_0^\Gamma$, so we find

$$\frac{T_h}{T_\infty} = \left(\frac{n_h}{n_\infty}\right)^{\Gamma-1} \propto \left(\frac{kT_\infty}{m_B c^2}\right)^{-3(\Gamma-1)/2} \tag{6.9}$$

We can now apply these results to see how the luminosity scales in different phases of the inspiral. During both the very early pre-merger phase of the inspiral, when $d > R_a$, and during the post-merger phase after the fluid has settled to a quasiequilibrium state, there are no shocks present. We can therefore use the above results to see that in these phases,

$$L_{ff} \propto \begin{cases} n_1^2\ T_6^{-3} M_6^3\ , & \Gamma = 5/3 \text{ or } \Gamma = \Gamma^*\ , \\ n_1^2\ T_6^{-(3\Gamma+1)/2} M_6^3\ , & \Gamma = \text{const} < 5/3\ , \end{cases} \tag{6.10}$$

$$L_{syn} \propto \begin{cases} n_1^2\ T_6^{-3} \beta_1^{-1} M_6^3\ , & \Gamma = 5/3 \text{ or } \Gamma = \Gamma^*\ , \\ n_1^2\ T_6^{-9(\Gamma-1)/2} \beta_1^{-1} M_6^3\ , & \Gamma = \text{const} < 5/3\ . \end{cases} \tag{6.11}$$

Here $\beta_1 \equiv \beta/10$. During the late premerger phase when $d \sim M \ll R_a$ shocks will be present and T_h will no longer depend on T_∞ for any EOS. In this case, we find

$$L_{ff} \propto n_1^2\ T_6^{-3} M_6^3 \quad , \quad L_{syn} \propto n_1^2\ T_6^{-3} \beta_1^{-1} M_6^3\ . \tag{6.12}$$

Using the above scaling relations along with the results of our realistic temperature simulations, we find that the peak luminosity shortly before the merger of an equal mass BHBH binary in a gas cloud for case RA1 ($\Gamma = \Gamma^*$) is given by

$$L_{ff}^{max} \approx 3 \times 10^{37}\ n_1^2\ T_6^{-3} M_6^3\ \text{erg s}^{-1}\ , \tag{6.13}$$

$$L_{syn}^{max} \approx 3 \times 10^{43}\ n_1^2\ T_6^{-3} \beta_1^{-1} M_6^3\ \text{erg s}^{-1}\ . \tag{6.14}$$

Similarly, the peak luminosity for case RA2 ($\Gamma = 5/3$) is given by

$$L_{ff}^{max} \approx 4 \times 10^{37}\ n_1^2\ T_6^{-3} M_6^3\ \mathrm{erg\ s^{-1}}\ , \tag{6.15}$$

$$L_{syn}^{max} \approx 4 \times 10^{43}\ n_1^2\ T_6^{-3} \beta_1^{-1} M_6^3\ \mathrm{erg\ s^{-1}}\ . \tag{6.16}$$

At the late post-merger phase, the fluid relaxes to a stationary flow. The scaling relations (6.10) and (6.11) hold. Combining these scaling relations and our simulation results, we find that during the post-merger phase

$$L_{ff} \approx 3 \times 10^{35}\ n_1^2\ T_6^{-3} M_6^3\ \mathrm{erg\ s^{-1}}\ , \tag{6.17}$$

$$L_{syn} \approx 8 \times 10^{38}\ n_1^2\ T_6^{-3} \beta_1^{-1} M_6^3\ \mathrm{erg\ s^{-1}} \tag{6.18}$$

for case RA1, and

$$L_{ff} \approx 3 \times 10^{36}\ n_1^2\ T_6^{-3} M_6^3\ \mathrm{erg\ s^{-1}}\ , \tag{6.19}$$

$$L_{syn} \approx 2 \times 10^{41}\ n_1^2\ T_6^{-3} \beta_1^{-1} M_6^3\ \mathrm{erg\ s^{-1}} \tag{6.20}$$

for case RA2. We note that in each case, the total luminosity is dominated by the synchrotron emission.

In each of our calculations, we have ignored the effects of radiative cooling on the gas dynamics. We can estimate the error induced by this by comparing the rate of thermal energy transport, $\dot{E}_{th}$, to the luminosity. Here we define

$$\dot{E}_{th} = \dot{M}\epsilon = \dot{M}\frac{P}{\rho_0(\Gamma - 1)}\ . \tag{6.21}$$

Since the luminosity is dominated by emission near the horizon, we are primarily concerned about the region near the horizon. Using Eqs. (5.10), (6.7), (6.8), (6.17) and (6.18), we find that for case RA1, at late times after the merger when the flow has reached equilibrium,

$$\frac{L_{syn} + L_{ff}}{\dot{E}_{th}} \sim 0.1\ n_1\ T_6^{-3/2}\ \beta_1^{-1} M_6\ . \tag{6.22}$$

Thus, we see that in these regimes, it is a good approximation to neglect the effects of radiative cooling for our canonical model parameters. At the moment of maximum luminosity, shortly before merger, we find that

$$\frac{L_{syn} + L_{ff}}{\dot{E}_{th}} \sim 40\ n_1\ T_6^{-3/2} \beta_1^{-1}\ M_6\ . \tag{6.23}$$

Thus during the final stages of the merger, the validity of our assumption of adiabatic flow begins to break down for canonical parameters. In future work, we will address this by including cooling terms in our gas evolution to account for energy losses due to radiation.

We also note that in order for us to be able to neglect radiation pressure in the momentum equation, we require that the luminosity be small compared to the Eddington luminosity. We find that for case RA1,

$$\frac{L_{syn}^{max} + L_{ff}^{max}}{L_{Edd}} \sim 0.2\ n_1^2\ T_6^{-3} \beta_1^{-1} M_6^2\ , \tag{6.24}$$

which suggests that radiation pressure may begin to play a role for parameters close to our canonical choices.

In calculating the luminosity, we have assumed that the gas is optically thin. We can verify this assumption by estimating the optical depth. For the gas parameters chosen for this study ($n_\infty = 10$ cm^{-3} and $T_\infty = 10^6$K), we find that the dominant source of opacity is electron scattering. We estimate that the optical depth for electron scattering of synchrotron photons is

$$\tau_{es} \approx n_h \sigma_T R \sim\ 10^{-3} n_1 T_6^{-3/2} M_6, \tag{6.25}$$

where $n_h \sim 10^{11} n_1 T_6^{-3/2}$ is the density at the horizon, $\sigma_T = 0.67 \times 10^{-24}$ cm^2 is the Thomson scattering cross-section, and $R \sim 10^{11} M_6$ cm is the characteristic size of the emission region. Thus, our assumption of an optically thin gas is valid.

To estimate the characteristic frequencies at which the emission occurs we again note that the maximum emission comes from near the horizons and compute the characteristic frequency produced in this region. For bremsstrahlung emission, the characteristic observed frequency of the emission is given by $h\nu \sim kT_h/(1+z)$ for a source at redshift z. We measure the maximum temperature near the horizon for our case RA1, and find that at the moment of maximum luminosity in the late pre-merger phase,

$$h\nu_{ff}^{max} \approx \frac{150\ \text{MeV}}{1+z}\ \text{(RA1)}\ , \tag{6.26}$$

After the merger, in the quasistationary phase, we find that the characteristic frequency drops to

$$h\nu_{ff} \approx \frac{10\ \text{MeV}}{1+z}\ \text{(RA1)}\ . \tag{6.27}$$

Following the same procedure for case RA2, we find that at the moment of maximum luminosity in the late

pre-merger phase,

$$h\nu_{ff}^{max} \approx \frac{230 \text{ MeV}}{1+z} \text{ (RA2)} , \tag{6.28}$$

and in the post-merger phase, the frequency drops to,

$$h\nu_{ff} \approx \frac{50 \text{ MeV}}{1+z} \text{ (RA2)} . \tag{6.29}$$

Thus, we see that the bremsstrahlung emission will be predominantly in γ-rays, in agreement with [64]. Given the bremsstrahlung luminosity calculated above, we estimate that the flux from this emission will be $\sim 10^{-21}$erg cm^{-2} s^{-1} for a source at $z = 1$. Unfortunately, it is unlikely that this emission is strong enough to be detectable.

We can estimate the characteristic frequency of the synchrotron emission by noting that Eq. (D.10) is maximized when $x_M \approx 1.09$. For case RA1, this corresponds to an observed frequency

$$h\nu_{syn}^{max} = \frac{1.09}{1+z}\frac{3ehB}{4\pi m_e c}\left(\frac{kT}{m_e c^2}\right)^2 \tag{6.30}$$

$$= \frac{80}{1+z}\, n_1^{1/2}\, T_6^{-3/4}\beta_1^{-1/2} \text{ eV (RA1)} \tag{6.31}$$

during the late pre-merger phase at the moment of maximum luminosity. In the post-merger phase, the frequency drops to,

$$h\nu_{syn} = \frac{0.008}{1+z}\, n_1^{1/2}\, T_6^{-3/4}\beta_1^{-1/2} \text{ eV (RA1)} , \tag{6.32}$$

For case RA2, we find the characteristic synchrotron frequency to be

$$h\nu_{syn}^{max} = \frac{100}{1+z}\, n_1^{1/2}\, T_6^{-3/4}\beta_1^{-1/2} \text{ eV (RA2)} \tag{6.33}$$

during the late pre-merger phase at the moment of maximum luminosity, and

$$h\nu_{syn} = \frac{0.75}{1+z}\, n_1^{1/2}\, T_6^{-3/4}\beta_1^{-1/2} \text{ eV (RA2)} \tag{6.34}$$

during the post-merger phase.

This corresponds to infrared and visible radiation. For a binary at $z = 1$ with the luminosity calculated above, this source has an apparent magnitude of $m = 24$ and should be observable by the proposed LSST instrument [112]. Our simulations follow the late stage of the inspiral in which the binary separation decreases from $d = 10M$ to merger. For a $10^6 M_\odot$ binary, this corresponds to a timescale of $\Delta t \sim 1.3$ hrs during which

Table 6.4: Parameters for BHBH disk simulations

Case	[a]Epoch	Orientation	Γ	[b]H/R
A1	early inspiral	prograde	5/3	0.11
A2			4/3	0.08
A3			[c]1.1	0.03
A4		retrograde	4/3	0.08
B1	late inspiral	prograde	5/3	0.14
B2	and merger		4/3	0.11
B3			[c]1.1	0.06
B4		retrograde	4/3	0.11

[a] Initial binary separation $d/M = 10$.
[b] H is the scale height of the disk at $R = R_{disk}$ (pressure max), measured at $t = 0$ for case-A runs and at $t = t_{merge}$ for case-B runs.
[c] Approximately isothermal.

the radiation should achieve peak values.

We note that all the scalings derived above will not apply when $V_\infty \gg a_\infty$, but can be derived in a similar fashion. For a realistic gas with $T \gtrsim 10^6 K$ ($a_\infty \approx 100$km/s), this regime may never be realized, so we neglect here.

6.2 Binary disk accretion

Each of our simulations into two phases. We first perform early inspiral epoch simulations in which we employ the quasistationary CTS metric while keeping the BH separation constant. This allows the disk to relax to a reliable quasistationary state. Upon achieving this state, we begin our late inspiral and merger epochs simulations in which we evolve the metric in full GR, allowing the BHs to inspiral and merge. Parameters for each of these disk runs are given in Table 6.4.

Equatorial snapshots from our simulations with $\Gamma = 5/3$ can be seen in Fig. 6.21, while meridional snapshots are shown in Fig. 6.22. The first two snapshots are from the early inspiral epoch calculations, while the second two snapshots are from the late inspiral and merger epochs calculations. We do not show snapshots for other equations of state here, as the accretion flow is qualitatively similar. Important results from simulations with other equations of state are reported in Table 6.5.

6.2.1 Early inspiral epoch

While the formulation outlined in Sec. 4.2 provides stable equilibrium disk initial data for a *single* BH, torques from the *binary* disrupt this equilibrium. Thus, it is important to allow the gas to relax to a

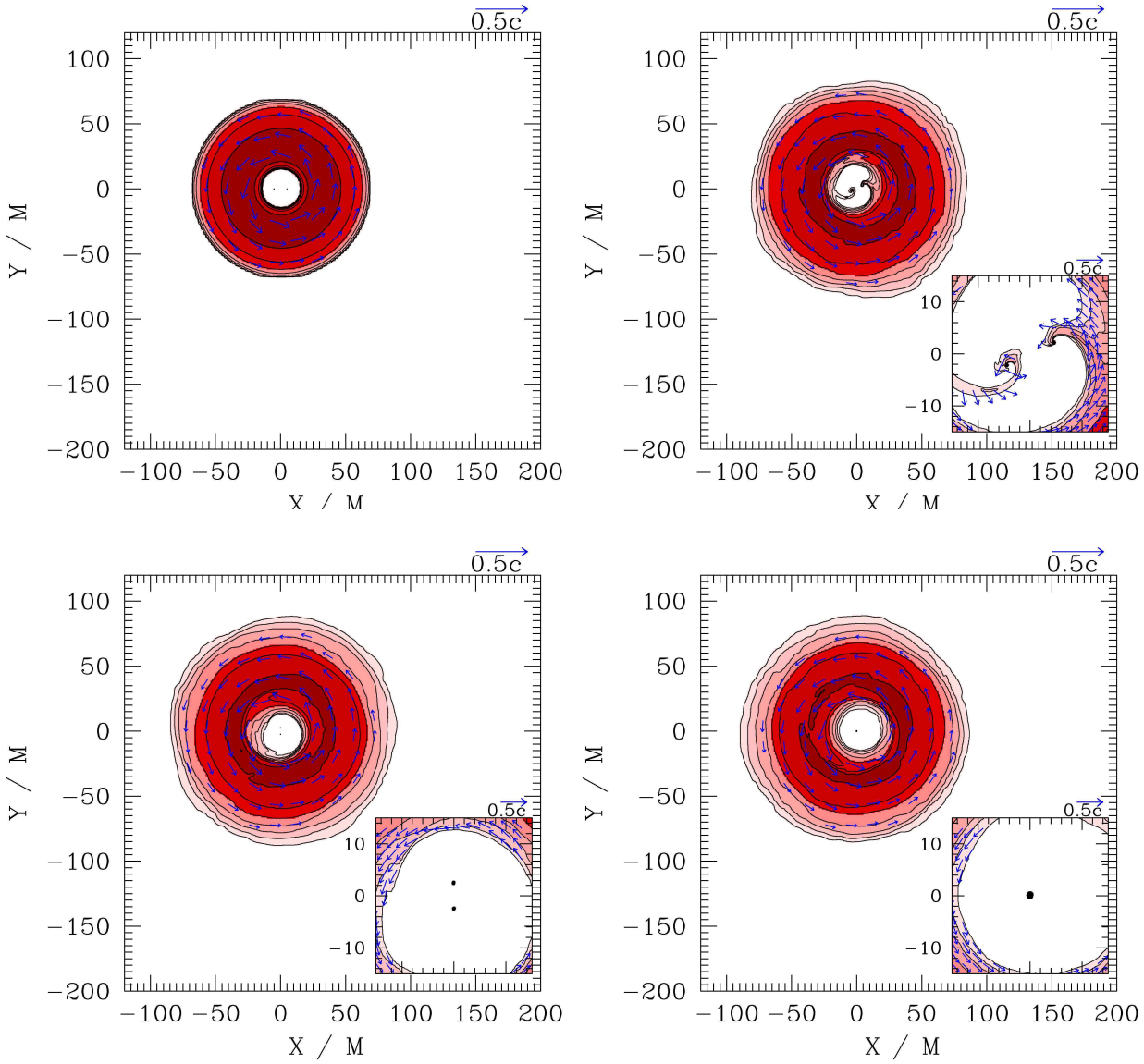

Figure 6.21: Snapshots of rest-mass density ρ_0 contours in the orbital plane for cases with $\Gamma = 5/3$. Density contours are plotted at $\rho_0/\rho_{0,max} = 10^{-2.75+0.5j}$ $(j = 1, 2, ..., 6)$. Contours of highest density are shown with darker shading and are near the BHs. Blue arrows denote velocity vectors. The apparent horizon interior is marked by a filled black circle. The top left frame is the initial data from the early inspiral epoch, the top right frame is the relaxed, quasistationary disk, which serves as initial data for the late inspiral and merger epochs at $t \approx t_{merge} - 1250M$. The bottom left frame is the data from the late inspiral and merger epochs run at $t \sim t_{merge} - 50M$, while the bottom left frame is the data from the late inspiral and merger epochs at $t \approx t_{merge} + t_{disk}$.

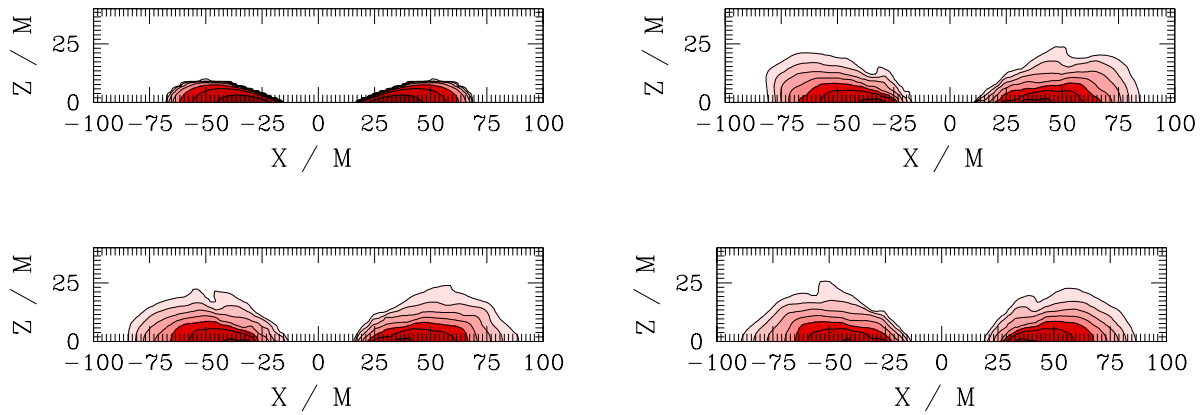

Figure 6.22: Snapshots of rest-mass denstiy ρ_0 contours in the meridional plane for cases with $\Gamma = 5/3$. Density contours are plotted at $\rho_0/\rho_{0,max} = 10^{-2.75+0.5j}$ $(j = 1, 2, ..., 6)$. Contours of highest density are near the BHs. The top left frame is the initial data for the early inspiral epoch; the top right frame is the relaxed, quasistationary disk that serves as initial data for the late inspiral and merger epochs; the lower left frame is the data from the late inspiral and merger epochs at $t \sim t_{merge} - 50M$; the bottom right frame is the data from the late inpiral and merger epochs at $t \approx t_{merge} + t_{disk}$.

quasistationary state before beginning the BH inspiral. We allow this relaxation to occur over $\sim 5t_{disk}$, where $t_{disk} \approx 1300M$. At this time, we find that $\dot{M}_0$, L_{syn}, and L_{brem} oscillate around roughly constant values, and there is little evolution in surface density profiles. Here L_{syn} and L_{brem} refer to synchrotron and bremsstrahlung luminosity, respectively.

During the relaxation process, the changes in the matter profiles are due to the presence of binary torques. These torques cause a disruption of the inner edge of the disk, allowing some gas to fall onto the BHs. Infalling gas forms spiral waves and shocks which heat the gas near the BHs. In the absence of shock heating, the disk would behave adiabatically, and the internal energy density would be given by its polytropic value,

$$\rho_0 \epsilon_{ad} = K \rho_0^{\Gamma} / (\Gamma - 1) \ . \tag{6.35}$$

Thus, shock heating may be measured by computing the enhancement in the internal energy density above its adiabatic value and integrating over the disk. We therefore compute

$$E_{int} = \int_{V_d} \sqrt{-g} \rho_0 u^t \epsilon \ d^3x \ , \tag{6.36}$$

and

$$E_{int,ad} = \int_{V_d} \sqrt{-g} \rho_0 u^t \epsilon_{ad} \ d^3x \ . \tag{6.37}$$

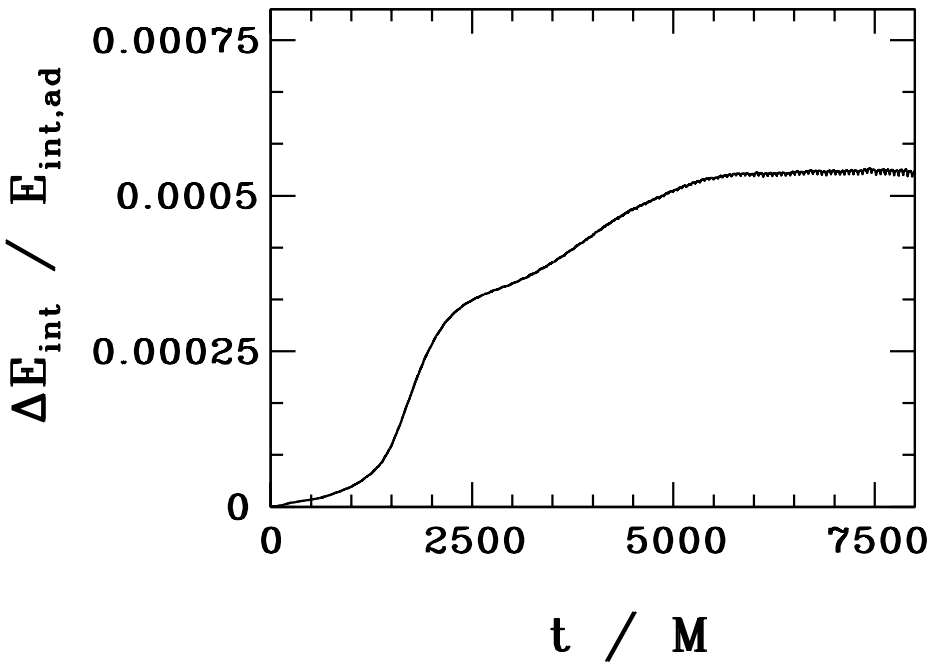

Figure 6.23: Time evolution of $\Delta E_{int}/E_{int,ad}$ for run A2.

Here the integral is over V_d, which is the volume between $r = 10M$ and the outer boundary of the computational domain at $128M$. This allows us to compute ΔE_{int} in the bulk of the disk, ignoring the gas near the BHs. In Fig. 6.23, we plot $\Delta E_{int}/E_{int,ad}$ vs time during the relaxation of the gas, where $\Delta E_{int} \equiv (E_{int} - E_{int,ad})$. We find that $\Delta E_{int}/E_{int,ad}$ increases monotonically over the course of the relaxation process, leveling off to a constant value of $\approx 5 \times 10^{-4}$ as the disk reaches a quasistationary state. Because $\Delta E_{int}/E_{int,ad} \ll 1$, we conclude that shock heating does not play a significant role in altering the bulk disk profile during this process.

In order to get a sense of the change in the disk profile from the initial data, we plot angle-averaged surface density profiles (see Fig. 6.24). In each case, the torque from the binary has the overall effect of pushing matter outward. However, the effect of the torques diminishes once the disk matter has moved outward and a quasistationary state is achieved after $t \sim 5t_{disk}$.

In Fig. 6.21, we plot snapshots of density contours for case A1. We see that the disk cavity, which initially extends to $R = 15M$, becomes partially filled, with a clear spiral structure, at small radii $R \lesssim 2d = 20M$ for each of the prograde cases. A similar spiral arm structure extending inside the disk cavity has been seen in Newtonian simulations (cf. [36, 113, 114]). In the retrograde case (A4), this structure is largely absent. This point is further emphasized by comparing the surface density fluctuation $\Delta\Sigma \equiv (\Sigma - \langle\Sigma\rangle)/\langle\Sigma\rangle$ between the prograde case A2 and the retrograde case A4 (see Figs. 6.25 and 6.26). Following [36], we compute this quantity in a rotating frame in which the binary is stationary, and average over several t_{orb}. In Fig. 6.25, we clearly see two strong spiral arms emanating from each BH and extending throughout the cavity region. However, unlike the results of the 2D, thin-disk simulations presented in [36], we do not see spiral density waves extending into the bulk of the disk. We attribute this to the fact that our 3d disks are thicker, which allows waves that are initially propagating in the radial direction to be deflected in the vertical direction, disrupting the spiral density wave structure. Such effects have been demonstrated even for geometrically thin disks in which density and temperature are stratified in the z direction [115, 116].

The structure of the spiral density waves observed near R_{in} is roughly consistent with the theoretical Newtonian picture of a wave that is excited by the binary torques at the outermost Lindblad resonance at $R_2 = (3/2)^{2/3}d$ with orbital resonance $\Omega_{bin} : \Omega = 3 : 2$ (initially, $R_2 = 0.87R_{in}$). We demonstrate this by computing the angle-averaged torque density as described in Sec. 4.4.7, and comparing with the (Newtonian) analytic prediction given in Eq. (31) of [36],

$$\frac{dT}{dR} \approx \frac{49}{288}\pi^2\Sigma(R_2)\Omega_{bin}^2\frac{d^4}{\lambda_2}\mathrm{Ai}\left(\frac{R_2 - R}{\lambda_2}\right) , \tag{6.38}$$

where $\lambda_2 = 2^{-2/3}(H/R)^{2/3}d$. Based on numerical data from run A1 at $t \gtrsim 5t_{disk}$, we choose $\Sigma(R_2) = 4 \times 10^{-4}\Sigma_0$ and $H/R = 0.3$, where Σ_0 is the initial maximum surface density and H/R is measured at R_2. As we show in Fig. 6.27, we find very good agreement with the analytic prediction out to $R/d \approx 2.2$, but break down at larger radii. This breakdown is not unexpected, as we have argued above that spiral density waves do not extend into the bulk of the disk as a result of the thickness of our 3d disks.

For the retrograde case (A4), we find that the spiral density waves are largely absent, as shown in Figs. 6.26 and 6.28. This is expected, as the Lindblad resonance does not exist when the angular momentum of the disk and the binary are antialigned.

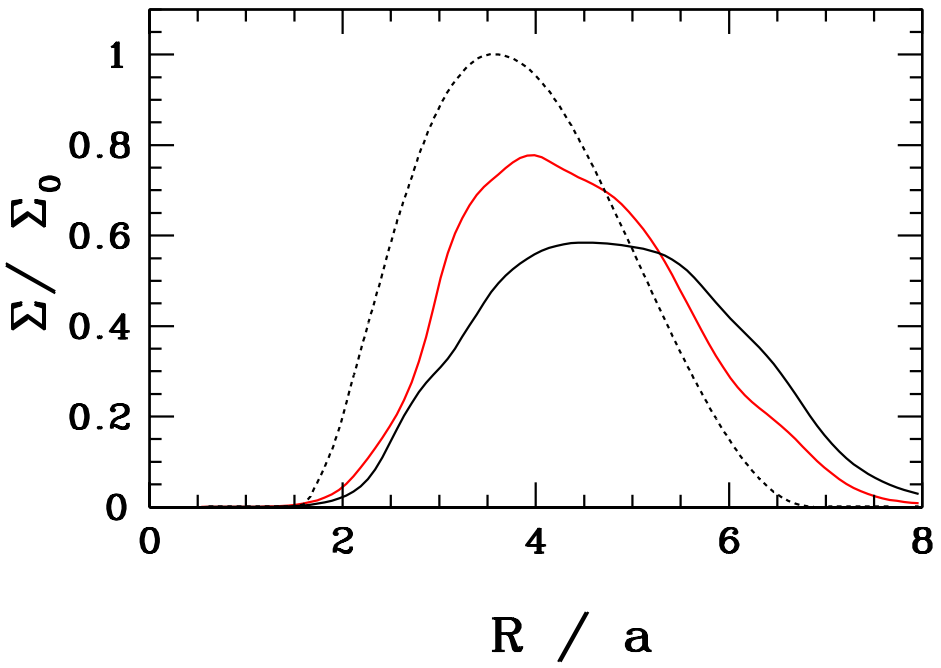

Figure 6.24: Surface density profiles of the $\Gamma = 5/3$ disk as a function of radius. The dashed black curve is the initial disk density prole; the solid red one is the surface density prole when the disk has reached a quasistationary configuration after $t \gtrsim 5t_{disk}$, averaged over $\sim 2t_{orb}$. The solid black curve is the density profile following the merger, averaged over $\sim 2t_{orb}$. Σ_0 is the initial maximum surface density.

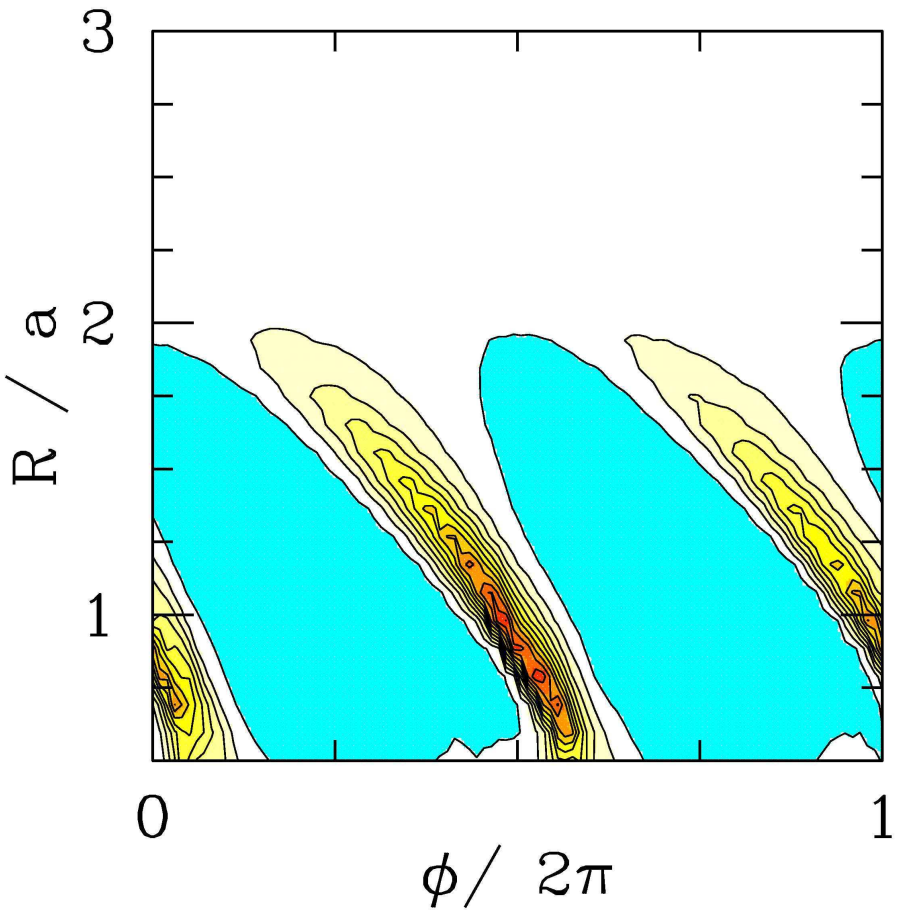

Figure 6.25: Time-averaged surface density fluctuation $(\Sigma - \langle\Sigma\rangle)/\langle\Sigma\rangle$ in the rotating frame in which the binary is at rest. The binary point masses are located at $R/a = 0.5$ and $\phi = (0, \pi)$. Red regions are density maxima and blue regions are density minima. Data is from run A2 with $\Gamma = 4/3$.

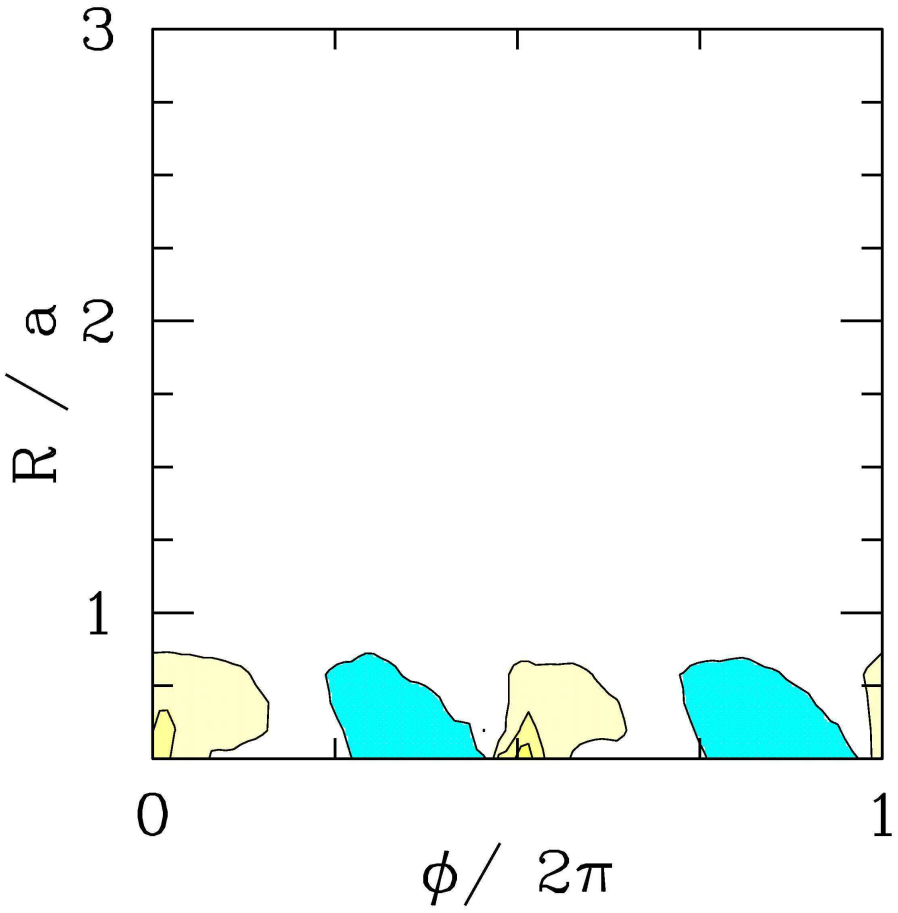

Figure 6.26: Same as Fig. 6.25 but for a retrograde disk.

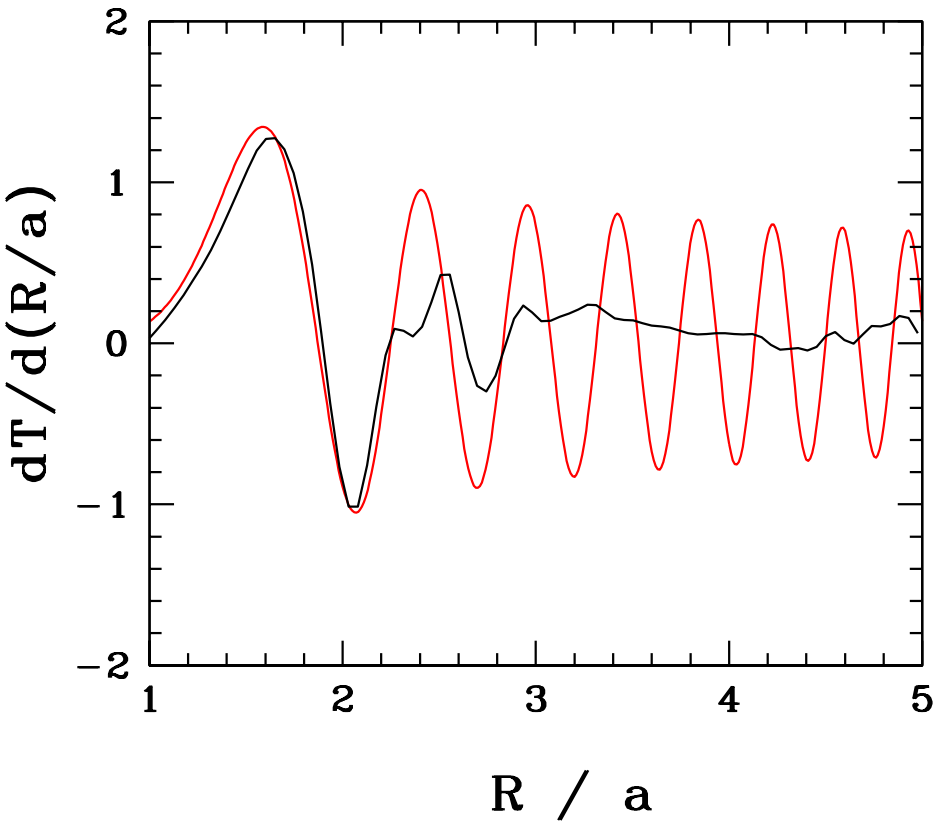

Figure 6.27: Time-averaged torque density dT/dR exerted by the binary on the disk after $t \gtrsim 5t_{disk}$. Time averaging was carried out over $\sim 2t_{orb}$ after the disk has reached a quasistationary state. Data from run A2 with $\Gamma = 4/3$. The torque is plotted in units of $10^{-3}Ma\Sigma_0$.

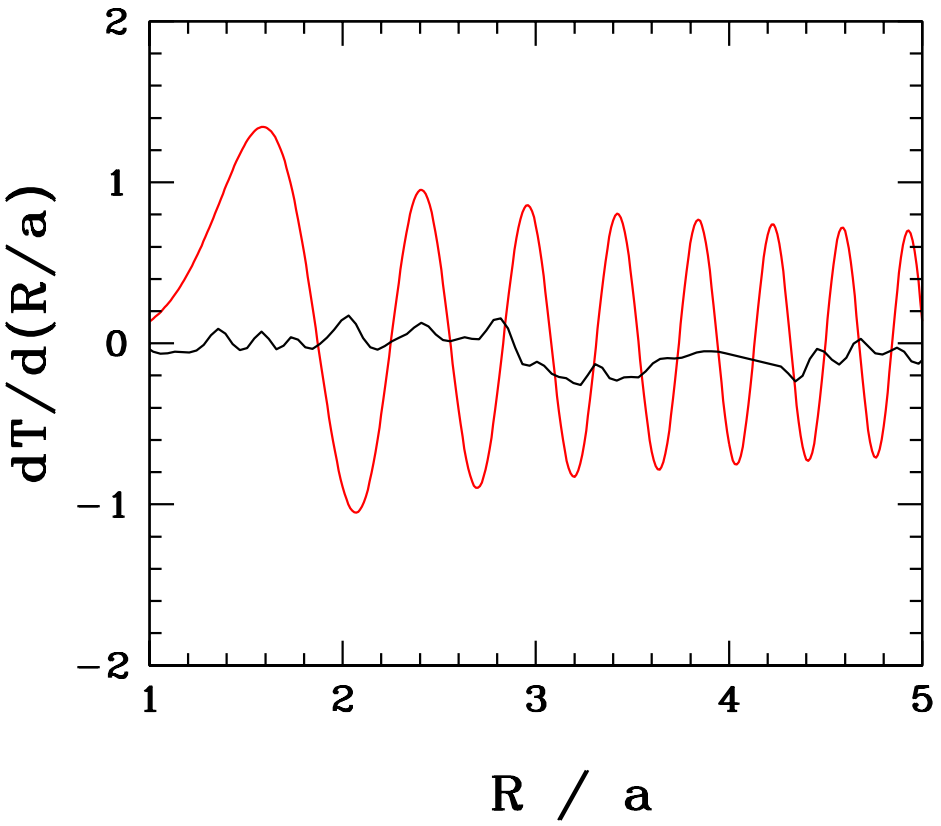

Figure 6.28: Same as Fig. 6.27, but for retrograde disk (run A4).

6.2.2 Late inspiral and merger epochs

Having allowed the disk to relax to a quasistationary state, we turn to the fully relativistic evolution of metric and matter fields in order to investigate variations in electromagnetic luminosity over the course of the inspiral and merger. Our calculations in this epoch apply to the decoupling phase of binary inspiral, through merger, but before appreciable gas fills the hollow due to viscosity. We again consider the prograde cases with $\Gamma = 4/3$ (B1), $\Gamma = 5/3$ (B2), and $\Gamma = 1.1$ (B3) the retrograde case with $\Gamma = 4/3$ (B4). In each case, we use the relaxed data from the end of the corresponding quasistationary metric run as initial data.

As the binary inspiral proceeds and the separation shrinks, the torques due to the binary are diminished. As a result, we find that the spiral density waves visible when $a/M = 10$ have largely disappeared by the time of merger and remain absent after the merger. This is evident in the bottom left and right frames of Fig. 6.21, which show snapshots of the density in the equatorial plane $\sim 50M$ before merger, and $\sim 1t_{disk}$ after merger. This effect is also illustrated by the evolution of $\dot{M}_0$, L_{brem}, and L_{syn} in Fig.6.29. Here, we have computed the luminosity assuming a fiducial value of $n_{disk} = 10^{12}$ cm^{-3}, where n_{disk} is the baryon number density at R_{disk}. This value is consistent with density estimates for a typical AGN derived from the Shakura-Sunyaev disk model [117, 60, 65], albeit in a radiation-dominated, geometrically thin regime. However, because there are large variations in the gas densities in galactic cores, we provide density scalings for our results. Because the position of the $m = 2$ outermost Lindblad resonance is approximately given by $R_2 \approx (3/2)^{2/3}d$, we see that as the binary separation is reduced, the location of the resonance retreats farther inside R_{in}, enabling less matter to be stripped from the inner edge of the disk, and reducing $\dot{M}_0$. The reduction in accretion similarly suppresses the electromagnetic luminosity generated near the BHs. This effect is exacerbated by the reduction in shock heating due to binary torques, as this lowers the temperature of the gas and reduces emissivities. Each of these effects is reflected in Fig. 6.29. We also show the h_+ polarization amplitude of the accompanying gravitational wave for comparison. Evidently, the decrease in electromagnetic luminosity beginning at the onset of decoupling is a precursor to the late inpiral and merger gravitational radiation. We find that the choice of EOS can play a significant role in setting the magnitude of the accretion rate and the luminosity. Larger values of Γ lead to both larger $\dot{M}_0$ as well as higher luminosities. We tabulate the values of luminosities, accretion rates and characteristic frequencies of emission at the onset of the late inspiral and merger epochs and just prior to merger in Table 6.5. In addition to the increase in the amount of gas near the BHs, larger values of Γ also allow the gas to be shock heated more effectively. Because the bremsstrahlung and synchrotron emissivities are sensitive to temperature, this also leads to an increase in luminosity. Comparing Eq. (6.39) and Eq. (6.40) below, we see that the temperature dependence is much stronger for synchrotron emission. This can explain the particularly large

differences in synchrotron luminosity for the different cases reported in Table 6.5. This effect also leads the synchrotron luminosity to be dominated by emission from the heated region near the binary, whereas the bremsstrahlung emission is predominantly from the bulk of the disk. This dependence accounts for the high variability of the synchrotron luminosity in comparison to that of the bremsstrahlung emission.

Because our simulations assume a perfect fluid with no dynamical magnetic fields (turbulent fields are assumed only to estimate synchrotron emission), there is no viscosity present to counteract the effect of the binary torques in driving matter outward. As a result, we find that even after relaxing to a quasistationary disk state in our early inspiral epoch calculations, in which the accretion rate and luminosity oscillate around fixed values, there remains an overall slow outward drift in the bulk of the disk. This is evident in Fig. 6.24, in which the solid red curve shows the surface density profile at the beginning of the binary inspiral, while the solid black curve shows the surface density profile at $t \sim t_{disk}$ after the merger. We see clear evidence that the bulk of the disk moves outward, although we suspect that this effect may be altered by the inclusion of viscosity.

In Paper I, we demonstrated that shocks near the BH horizons increased in strength throughout the merger as the BHs move more supersonically through the surrounding gas. This shock strengthening leads to a temperature increase in the inner region, which in turn gives rise to an increasing luminosity peaking at the moment of merger. Such a temperature increase is largely absent in the disklike accretion case treated here, as can be seen by comparing temperature contours at the beginning of the late inspiral and merger epochs simulation and at $t \sim t_{merge} - 50M$, as displayed in Fig. 6.30. As such, we do not expect to see significant increase in luminosity during the post-decoupling inspiral phase, even at high-frequency components of the spectrum. We note that this contrasts the conclusions of the Newtonian calculation in [15], where a brightening of the precursor light curve before merger is found. However, these results do not necessarily contradict one another, as [15] consider geometrically thin, optically thick disks around non-equal-mass BHBH binaries. This is a very different scenario from the geometrically thick, optically thin disks surrounding equal-mass binaries that we consider in this paper.

To highlight the role that shock heating plays in our simulations, we also plot contours of K/K_0. Here $K \equiv P/\rho_0^{\Gamma}$ and K_0 is the initial value of K everywhere. The quantity $K = K(s)$, where s is the specific gas entropy, remains constant in the absence of shocks; shock heating yields $K/K_0 > 1$ (see Appendix B of [104]). As expected, we see that K/K_0 increases steeply near the BHs, where the binary torque-induced spiral arms are strongest (see Fig. 6.31). Following the merger, binary torques are no longer present and we find that K/K_0 is dramatically reduced in the cavity region. While we do find that a small region near the remnant continues to have K/K_0 long after the merger (see Fig. 6.31), we note that the gas in this region

is of very low density and carries a relatively insignificant amount of thermal energy.

We also note that the shocks are confined to the inner region and do not propagate into the bulk of the disk. While it has been proposed that changes in the potential due to mass loss and/or BH kicks following merger can give rise to shocks throughout the disk [118, 11], we do not observe such behavior in our simulations. However, this is expected, as it has been noted that a condition for shocks to form due to mass loss is that $\epsilon > H/R$, where $\epsilon \equiv (M_i - M_f)/M_i$ is the fractional mass loss due to gravitational wave emission [11]. Comparing the fractional mass loss for an equal-mass merger, for which $\epsilon \approx 0.05$, to the estimates of H/R measured at the moment of binary merger (see Table 6.4), we find that the above condition is never satisfied. The criteria above for shocks to form is derived from the condition that the radial velocity must exceed the sound speed $c_s \equiv (\Gamma P/\rho_0 h)^{1/2}$ near the inner edge of the disk. We have also checked this directly and have found that the condition is never met in our simulations - our disks are too hot, hence too geometrically thick, to trigger this effect.

6.2.3 Scaling and detectability

In quoting values for the accretion rate $\dot{M}_0$, we normalize by the quantity $\rho_{max} M^2 = 0.2 n_{12} M_8^2 M_\odot \mathrm{yr}^{-1}$, which allows for easy scaling to arbitrary disk density and binary mass. It is also possible to derive simple scaling relations for the luminosities. The dominant region of emission differs for bremsstrahlung and synchrotron radiation. Because of the stronger dependence of synchrotron emissivity on temperature (see Appendix B of [16]), we find that the synchrotron emission originates chiefly from the hot gas near the BHs, while the majority of bremsstrahlung emission originates from the cooler, denser gas in the bulk of the disk. In each simulation, we find that the temperature is maximum near the BHs, typically reaching $kT_h \approx 100\mathrm{MeV}$ at the horizon. In the high-temperature limit ($kT > m_e c^2$) the synchrotron emissivity given in Appendix B of [16] scales with temperature and density according to

$$q_{\mathrm{syn}} \propto n_h^2 T_h^3 \beta^{-1} \ . \tag{6.39}$$

By contrast, the temperature in the bulk of the disk where the majority of the bremsstrahlung emission originates is nonrelativistic ($kT_{disk} < m_e c^2$) so that the bremsstrahlung emissivity scales according to

$$q_{ff} \propto n_{disk}^2 T_{disk}^{1/2} \ . \tag{6.40}$$

Here n_h and T_h refer to the density and temperature at the horizon, and n_{disk} and T_{disk} refer to the density and temperature at R_{disk}, and $\beta \equiv 8\pi P/B^2$ sets the strength of the assumed turbulent magnetic

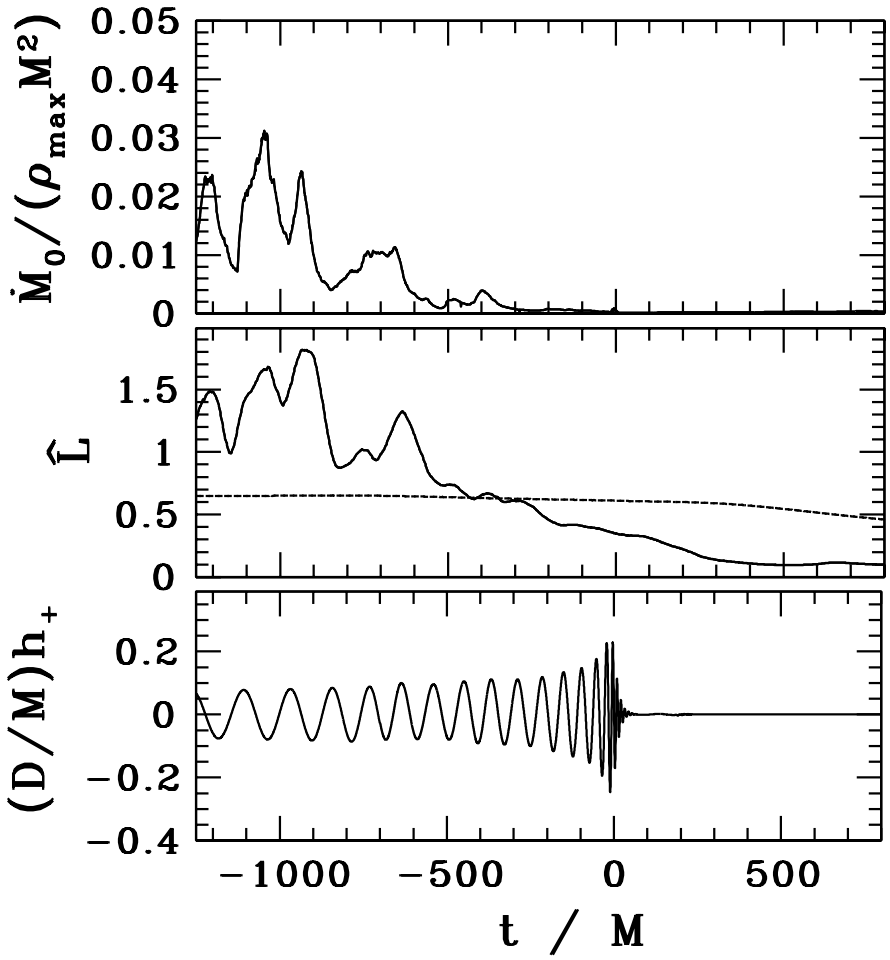

Figure 6.29: Time evolution of total BH accretion rate across the BH horizons $\dot{M}_0$, luminosity $\hat{L}$ and waveform Dh_+ for a circumbinary prograde disk with $\Gamma = 5/3$. The initial binary separation is $d = 10M$ and the BHs evolve to merger. $\dot{M}_0/(\rho_{max}M^2)$ is the dimensionless accretion rate. Here, $\rho_{max}M^2 = 0.2n_{12}M_8^2M_\odot \mathrm{yr}^{-1}$. $\hat{L} \equiv L/[10^{46}M_8^3n_{12}^2 \text{ erg s}^{-1}]$ is the total luminosity due to bremsstrahlung (dashed line) and synchrotron (solid line) emission. For synchrotron emission, we assume $\beta = 10$. h_+ is the + polarization of the gravitational wave signal as measured by an observer looking down the polar axis at a distance D from the binary. BHBH merger occurs at $t = 0$.

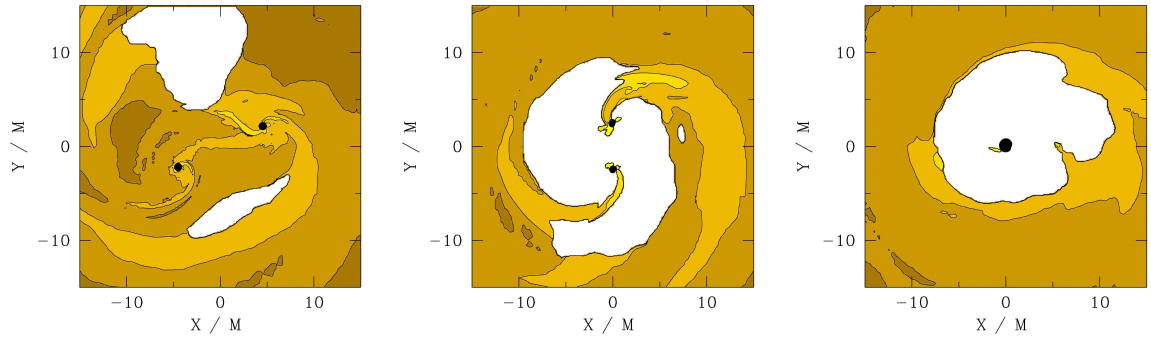

Figure 6.30: Contours of temperature kT $(= m_B P/\rho_0)$ at select times for prograde disk with $\Gamma = 5/3$. Contours correspond to $kT = 940 \times 10^{-5+0.33j} MeV \quad (j = 1, 2, ..., 6)$. Frames correspond to the beginning of the late inspiral and merger epochs phase at $t \approx t_{merge} - 1250M$ (top), $t \sim t_{merge} - 50M$ (middle), and $t \sim t_{merge} + t_{disk}$ (bottom). Regions with density less than $\rho_0/\rho_{0,max} < 10^{-4.5}$ are left white. Lighter shading denotes higher kT.

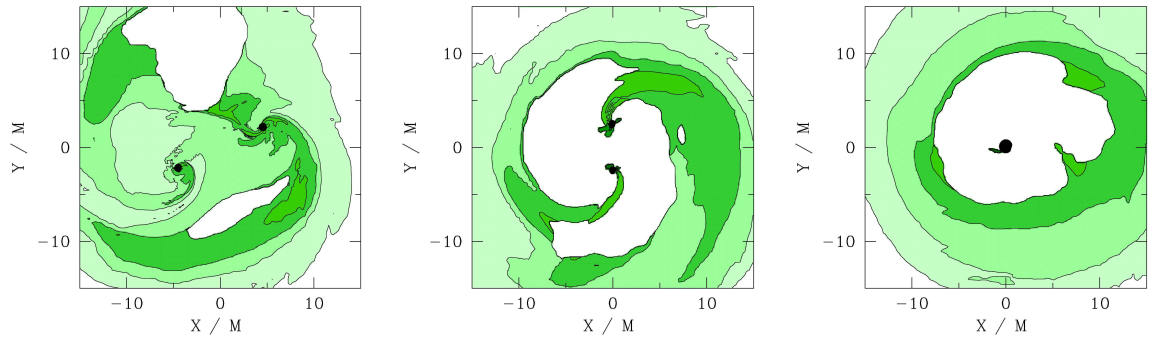

Figure 6.31: Contours of entropy parameter K $(= P/\rho_0^{\Gamma})$ at select times for prograde disk with $\Gamma = 5/3$. Contours correspond to $K/K_0 = 10^{0.1+0.3j} \quad (j = 1, 2, ..., 6)$. Frames correspond to the beginning of the late inspiral and merger epochs phase at $t \approx t_{merge} - 1250M$ (top), $t \sim t_{merge} - 50M$ (middle), and $t \sim t_{merge} + t_{disk}$ (bottom). Regions with density less than $\rho_0/\rho_{0,max} < 10^{-4.5}$ are left white. Darker shading denotes higher K.

field responsible for synchrotron emission. As in Paper I, we choose $\beta = 10$ so that the magnetic field is assumed to reach a fraction of its equipartition value consistent with MHD simulations [102].

Integrating Eqs. (6.39) and (6.40), we find

$$L_{syn} \approx \int dV q_{syn} \propto n_h^2 T_h^3 \beta^{-1} M^3 \ , \tag{6.41}$$

$$L_{ff} \approx \int dV q_{ff} \propto n_{disk}^2 T_{disk}^{1/2} R_{disk}^3 (H/R) \ , \tag{6.42}$$

where the factor of M^3 comes from the volume element.

Because we ignore self-gravity in the disk, our scaling results apply for arbitrary density. Accordingly, as the density at the horizon is varied, its value is simply proportional to the maximum density in the disk, $n_h \propto n_{disk} \propto \rho_{max}$.

Consider the onset of the binary decoupling (late inspiral) phase. The spiral arms through which the gas enters the disk cavity are shock heated. The gas in any shocked region will be heated to $kT \sim m_B v^2$. Since $v \lesssim c$ near the horizon, shock heating guarantees that $kT_h \lesssim m_B c^2 \sim 10^3$ MeV, independent of the temperature in the bulk of the disk (in fact KT_h is closer to 100 MeV). Scaling for synchrotron luminosity then simplifies to

$$L_{syn} \propto \rho_{max}^2 \beta^{-1} M^3 \ . \tag{6.43}$$

While the bremsstrahlung luminosity does depend on T_{disk}, we note that for the fixed values of q, $l(R_{in})$, and R_{in}/M, the enthalpy profile h, and therefore $kT_{disk} = m_B(h_{disk} - 1)(\Gamma - 1)/\Gamma$, is uniquely specified. We therefore regard T_{disk} as a fixed parameter, so that

$$L_{ff} \propto \rho_{max}^2 M^3 \ . \tag{6.44}$$

Using these scaling relations, along with the results of our simulations, we estimate the average luminosity when the binary separation is $a = 10M$, the adopted onset of the late inspiral and merger epochs. Results are given in Table 6.5.

In calculating the luminosity, we have assumed that the gas is optically thin. We can verify that this is a good assumption by estimating the optical depth. Taking the dominant opacity source to be electron scattering, we find

$$\tau_{es} \approx n_h \sigma_T R \sim 0.2 n_{12} M_8 \tag{6.45}$$

where R is the characteristic size of the emission region that we have set to $R \approx 2M$. Thus, we see that our assumption of an optically thin gas is valid for our canonical parameters, although it begins to break down

Table 6.5: Electromagnetic emission at beginning of late inspiral and merger epoch and shortly before merger

Case	Time	$^a\dot{M}_0/(\rho_{max}M^2)$	$^bL_{ff}/L_{46}$	L_{syn}/L_{46}
B1	$t_{merge}-1250M$	0.02	0.65	$1.2\beta_1^{-1}$
B2		0.003	0.16	$0.05\beta_1^{-1}$
B3		0.0005	0.003	$2\times10^{-5}\beta_1^{-1}$
B4		0.01	0.15	$0.5\beta_1^{-1}$
B1	$t_{merge}-50M$	0.0003	0.60	$0.3\beta_1^{-1}$
B2		0.0005	0.14	$0.008\beta_1^{-1}$
B3		0.0001	0.002	$2.0\times10^{-6}\beta_1^{-1}$
B4		0.0005	0.13	$0.0002\beta_1^{-1}$

$^a\rho_{max}M^2 = 0.2n_{12}M_8^2M_\odot\mathrm{yr}^{-1}$, $n_{12}\equiv n/10^{12}\mathrm{cm}^{-3}$, $M_8\equiv M/10^8M_\odot$.
$^bL_{46} = 10^{46}n_{12}^2M_8^3\mathrm{erg\ s}^{-1}$

when we consider denser disks and/or more massive binaries.

For bremsstrahlung emission originating at R_{disk}, the characteristic observed frequency of the emission is given by

$$h\nu_{ff}\sim kT_{disk}/(1+z) \tag{6.46}$$

for a source at redshift z. We measure the temperature at R_{disk} for each of our cases, and report the estimated characteristic frequencies in Table 6.6. For canonical parameters, bremsstrahlung emission will be predominantly in γ rays. Based on our measured luminosities, we estimate that the observed flux from this emission will be in the range of $\sim 10^{-15}-10^{-14}n_{12}^2M_8^3\mathrm{erg\ cm}^{-2}\ \mathrm{s}^{-1}$ for a source at $z=1$. Unfortunately, it is unlikely that this emission is strong enough to be detectable. We note that the bremsstrahlung emission we measure is actually dominated by emission from the bulk of the disk rather than the heated gas near the BHs. This makes the emission even less likely to be detectable, as it exhibits only a small amount of variability.

In contrast, the synchrotron emission is predominantly produced near the BHs. We can estimate the characteristic frequency of the synchrotron emission by noting that Eq. (B10) of [16] is maximized when $x_M\equiv 2\nu/3\nu_0\theta^2\approx 1.09$. Here, $\nu_0\equiv eB/2\pi m_ec$ is the cyclotron frequency and $\theta\equiv kT/m_ec^2$. The corresponding observed frequency is

$$h\nu_{syn} = \frac{1.09}{1+z}\frac{3ehB}{4\pi m_ec}\left(\frac{kT}{m_ec^2}\right)^2\ . \tag{6.47}$$

We can use this expression, along with measured values of density and temperature in the vicinity of the horizon, to estimate characteristic values of $h\nu_{syn}$. Values for each case at the moment of decoupling and shortly before merger are given in Table 6.6, and typically fall in the infrared range. We estimate that in each case, the synchrotron emission should be observable by the proposed Wide Field Infrared Survey

Table 6.6: Characteristic frequencies at beginning of late inspiral and merger epoch and shortly before merger

Case	Time	$^c h\nu_{ff}$ $[(1+z)^{-1}\mathrm{MeV}]$	$^d h\nu_{syn}$ $[(1+z)^{-1} n_{12}^{1/2} \beta_1^{-1/2} \mathrm{eV}]$
B1	$t_{merge} - 1250M$	0.3	2.5
B2		0.2	0.6
B3		0.08	0.01
B4		0.2	1.6
B1	$t_{merge} - 50M$	0.3	1.7
B2		0.2	1.5
B3		0.08	1.7
B4		0.2	1.4

$^c h\nu_{ff} = kT_{disk}$
$^d \beta_1 \equiv \beta/10$, $\beta \equiv 8\pi P/B^2$.

Telescope (WFIRST) [119], and possibly by the Large Synoptic Survey Telescope instrument (LSST) [112]. Our simulations follow the late stage of the inspiral in which the binary separation decreases from $d = 10M$ to merger. This corresponds to a time scale of $\delta t \sim 100 M_8$ hrs during which the gradual decline in emission should be observed.

6.3 Magnetized binary disk accretion

Here we report the first fully GRMHD simulation of a magnetized, circumbinary BHBH accretion disk. The effective viscosity driving accretion arises from MHD turbulence triggered by the magnetorotational instability (MRI) [80]. This effective viscosity competes with the tidal torques exerted by the binary, so that a quasi-stationary state is reached prior to binary-disk decoupling [7, 74]. This state has been simulated both in Newtonian [7] and in Post-Newtonian [81] gravitation. Typically, the computational domain excludes the region near the BHs and artificial inner boundary conditions are imposed. Recent Newtonian studies [82] make clear the importance of imposing the correct boundary conditions on the flow inside the central disk hollow and near the BHs, further motivating a treatment in full, dynamical GR whereby BH horizons can be modeled reliably.

The basic evolution of the system is as follows: For large binary separations d, the inspiral time due to GW emission is much longer than the viscous time ($t_{\rm GW} \gtrsim t_{\rm vis}$), so that the disk settles into a quasi-stationary state. For equal-mass BHs, the binary tidal torques carve out a partial hollow in the disk [33, 7, 36, 78] of radius $\sim 2a$ and excite spiral density waves throughout the disk, that dissipate and heat the gas. However, gas can penetrate the hollow in response to the time-varying tidal torque [36, 83, 78, 81]. At sufficiently small

separations $t_{\rm GW} \lesssim t_{\rm vis}$, and the BHBH *decouples* from the disk. The disk structure at decoupling crucially determines its subsequent evolution and the EM emission. GW emission close to merger leads to mass loss [11, 10] and may induce remnant BH recoil [40], which give rise to further characteristic EM signatures. Here we simulate the system in two different epochs: (I) The pre-decoupling phase ($t_{\rm GW} > t_{\rm vis}$) and (II) the post-decoupling phase ($t_{\rm GW} < t_{\rm vis}$), including the inspiral and merger of the BHBH. We consider equal-mass, nonspinning binaries. While the BH mass scales out, we are primarily interested in total (ADM) masses $M \gtrsim 10^6 M_\odot$ and low density disks for which the tidally-induced binary inspiral and the disk self-gravity are negligible.

We use the Illinois numerical relativity code to carry out our simulations. The code has been extensively tested [89, 120] and used in our earlier BHBH simulations in gaseous media [16, 83]. For details and equations see [89, 120, 121]. The main new feature concerns our vector potential ($\mathcal{A}_\mu = \Phi n_\mu + A_\mu$) formulation for the magnetic induction equation, where n^μ is the future-directed timelike unit vector normal to a t =const. slice and $n^\mu A_\mu = 0$. We introduce a new generalized Lorenz gauge condition $\nabla_\mu \mathcal{A}^\mu = \xi n_\mu \mathcal{A}^\mu$, where ξ is a parameter (typically $\xi = 4/M$) and M is the total BHBH (ADM) mass. This condition results in damped traveling EM gauge modes, preventing the spurious emergence of B-fields associated with refinement boundaries [122].

The disk initial data represent an equilibrium disk orbiting a single Schwarzschild BH [93, 83] with an inner disk edge at $R_{\rm in} = 18M = 1.8a$, where the specific angular momentum $\ell_{\rm in} = 5.15M$ at $R_{\rm in}$, and a nearly Keplerian rotation profile parameter $q = 1.7$. We adopt a Γ-law equation of state with $\Gamma = 5/3$, appropriate for a disk composed of an ideal, nonrelativistic gas. We seed the disk with a weak poloidal B-field as described in [121]. The maximum relative strength of the initial B-field in the equatorial plane is $(P_M/P)_{max} = 0.025$. Here $P_M \equiv B^2/8\pi$ is magnetic pressure, P is gas pressure, and B^μ is the magnetic field measured in the comoving frame of the fluid.

Prior to decoupling we can neglect the slow BHBH inspiral. We model the spacetime during this epoch by adopting the BHBH metric derived in the conformal thin-sandwich (CTS) formalism [76], whereby the spacetime is stationary in the corotating frame (see [83] for details). The inner part of the disk settles into a quasiequilibrium state on a "viscous" time scale

$$\frac{t_{\rm vis}}{M} = \frac{2R_{\rm in}^2}{3\nu M} \sim 6500 \left(\frac{R_{\rm in}}{18M}\right)^{3/2} \left(\frac{\alpha}{0.13}\right)^{-1} \left(\frac{H/R}{0.3}\right)^{-2}, \tag{6.48}$$

Here R is the disk radius and ν is the effective viscosity induced by MHD turbulence [80]. This viscosity

can be fit (approximately) to an 'α-disk' law for purposes of analytic estimates.

$$\begin{aligned} \nu(R) &\equiv (2/3)\alpha(P/\rho_0)\Omega_K^{-1} \\ &\approx (2/3)\alpha(R/M)^{1/2}(H/R)^2 M \end{aligned} \tag{6.49}$$

where H is the disk scale height, and we have assumed vertical hydrostatic equilibrium to derive an approximate relationship between P/ρ_0 and H/R (see [65]). Equating the viscous time scale and the GW inspiral time scale yields the decoupling separation

$$\frac{d_d}{M} \approx 13 \left(\frac{\alpha}{0.13}\right)^{-2/5} \left(\frac{H/R}{0.3}\right)^{-4/5}, \tag{6.50}$$

where the normalizations give the typical parameters our simulations obtain for the relaxed state. Note, that for the geometrically thick, magnetic disks we treat, the expected decoupling radius is an order of magnitude smaller than typical thin-disk cases [7, 13]. We thus set our initial binary separation at $d/M = 10$ (orbital period $2\pi/\Omega = 225M$).

We evolve the system using the CTS spacetime for ~ 45 binary orbits (10,000 M) to allow the inner parts of the disk to settle into a quasistationary state. This epoch (1) models the pre-decoupling phase and (2) provides realistic, relaxed disk initial data for the post-decoupling inspiral phase. We model the post-decoupling phase by continuing the GRMHD evolution in the dynamical spacetime of the inspirational and merging BHBH binary. We treat two extreme opposite limiting cases: "no-cooling", which allows for gas heating via shocks induced by tidal torques and MHD turbulence, and "cooling", which removes all the heat generated via an effective local emissivity Λ of the form $T^{\mu\nu}{}_{;\nu} = -\Lambda u^\mu$ as in [123]. Our "cooling" case, though artificial, provides a representative example of the effects of cooling and has been adopted in previous work (e.g. [124, 81]). The particular "cooling" prescription we use drives the gas to isentropic behavior, i.e. $P/\rho_0^\Gamma = const.$ The cooling timescale is set to the local, Keplerian orbital period. Our simulations resolve the BH horizons and we impose *no inner boundary conditions*. In the pre-decoupling phase our grid consists of a hierarchy of 6 refinement levels with (coarsest, finest) resolution of $(5.33M, 0.16M)$ and outer boundary at $250M$. We resolve the fastest-growing MRI mode by at least 10 grid points in the bulk of the inner disk. We add two extra levels centered on each BH in the post-decoupling phase, increasing the (coarsest, finest) resolution to $(4M, M/32)$. After merger and ringdown we freeze the spacetime evolution, but continue to evolve the plasma. Equatorial symmetry is imposed throughout. We normalize results to those for a single BH that we evolved with the same initial magnetized disk and BH mass equal to M.

The initial disk (see Fig. 6.32) is not in equilibrium around the binary as it is perturbed by the binary

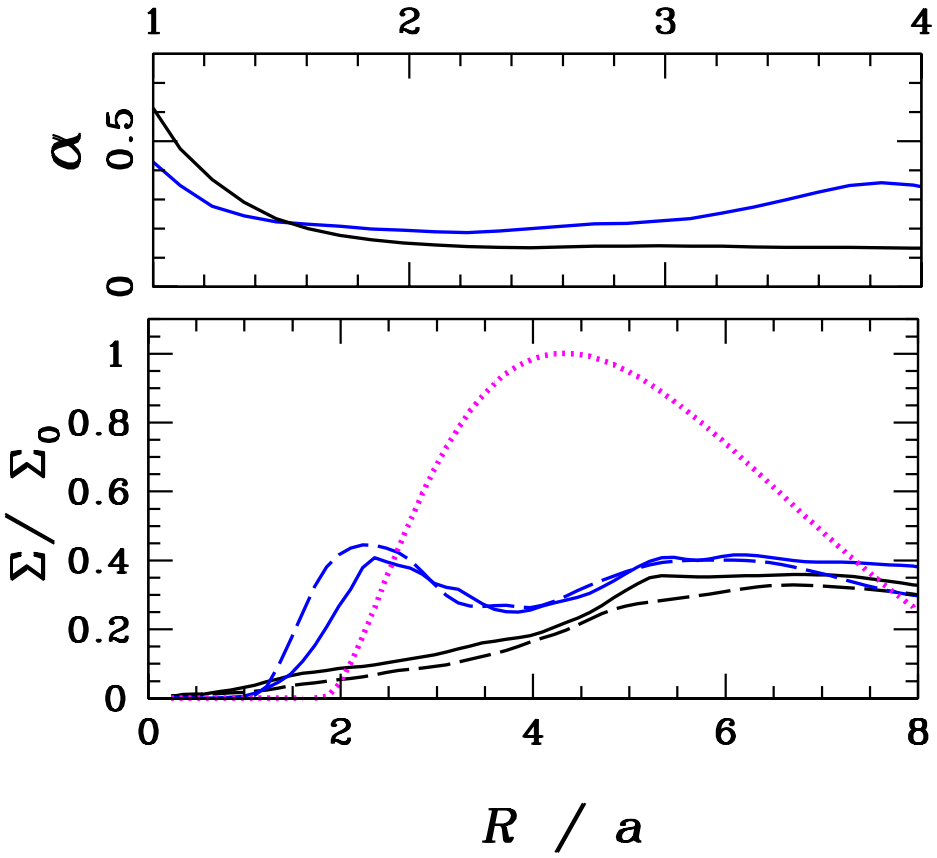

Figure 6.32: The disk α parameter and surface-density Σ profiles. Σ_0 is the maximum surface density at $t = 0$. Dotted magenta line is the initial data, solid lines are at decoupling, and dashed lines are at merger. Black lines are from the "no-cooling" case, and blue lines are from the "cooling" case.

torques. This leads to spiral density waves in the disk which dissipate and heat the gas. The gas gains angular momentum and the surface density profile moves slightly outward. Magnetic winding converts the poloidal field into one with a large toroidal component. MRI is induced, resulting in turbulent flow. After about 20 binary orbits ($\sim 4-5$ disk orbits at the pressure maximum) the MRI saturates, driving disk accretion onto the BHBH. In the relaxed disk prior to decoupling we measure a time-averaged Maxwell-stress as in [125] at $20M < R < 30M$, and find $\alpha = 0.13$ for the "no-cooling" (see Fig. 6.32) and $\alpha = 0.2$ for the "cooling" case. The magnetic-to-gas-pressure ratio $1/\beta$ ranges from 0.1 to 5 in the bulk of the disk.

Cooling influences the global disk structure. In particular, we observe matter pile-up near the inner disk edge only with cooling (see Fig. 6.32), as has previously been found in [36, 74, 126, 81]. The binary maintains a partial hollow in the disk (see Fig. 6.32) by exerting torques on the plasma, while the MRI-induced effective viscosity drives matter inward. Cooling leads to smaller scale height and lower ν, which explains the enhanced pile-up at R_{in}. We confirm the result in [36, 83, 126, 81] that non-negligible amounts

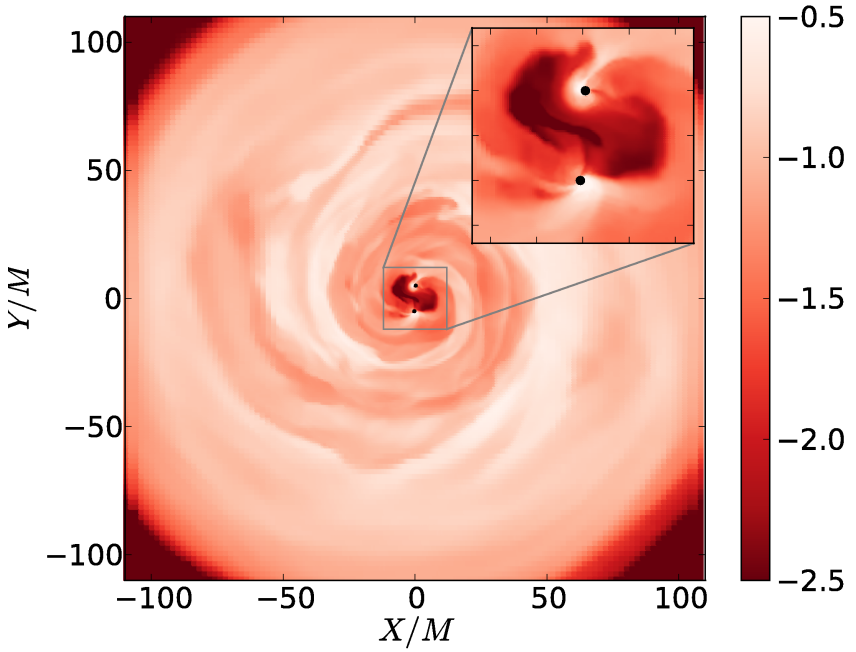

Figure 6.33: Orbital plane snapshot of rest-mass density $\log(\rho_0/\rho_{0,max})$ from the "no-cooling" simulation at $t \sim 10000M$ in the relaxed disk, prior to decoupling. The inset zooms in on the region close to the BHs.

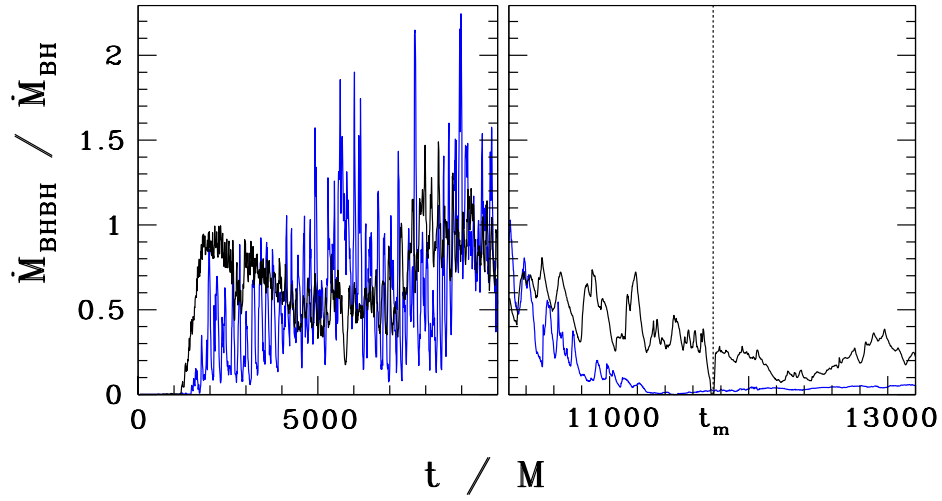

Figure 6.34: Time-averaged binary accretion rate $\dot{M}_{BHBH}$, normalized to the average value for a single BH $\dot{M}_{BH}$, versus time. Colors have the same meaning as in Fig. 6.32. Left panel: pre-decoupling (d =const) phase. Right panel: post-decoupling (inspiral) phase. $\dot{M}_{\rm BH} = 0.45 n_{12} M_8^2 M_\odot {\rm yr}^{-1}$ where $M_8 \equiv M/10^8 M_\odot$ and $n_{12} \equiv n/10^{12}{\rm cm}^{-3}$ is the initial maximum gas particle number density.

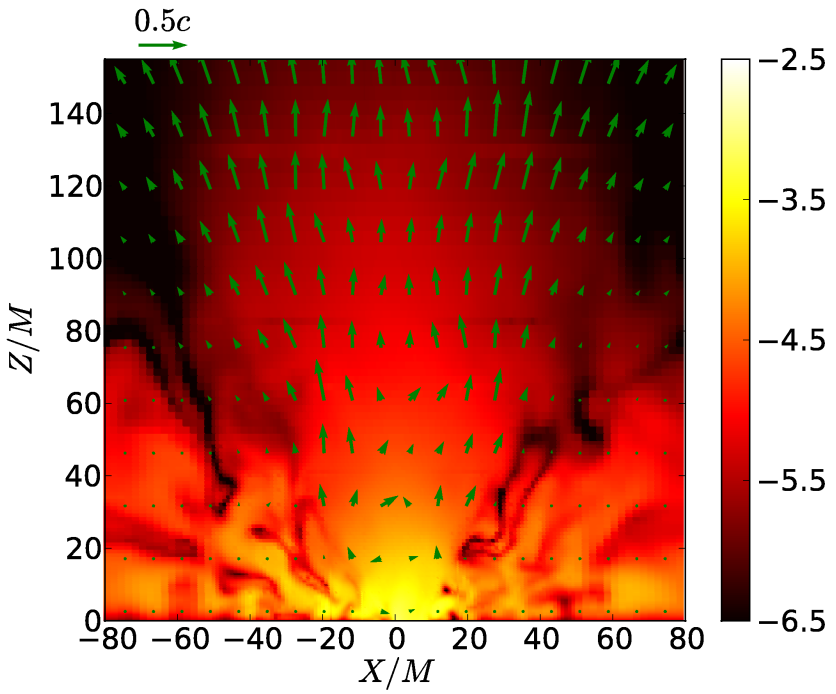

Figure 6.35: Meridional snapshot of magnetic pressure $\log(P_M/\rho_{0,max})$ and fluid velocity vectors at $t \sim 10000M$ for the "no-cooling" case.

of gas are present inside the cavity.

Accretion occurs predominantly via two spiral density streams inside the cavity (see Fig. 6.33). We find that accretion exhibits an alternating pattern by accreting primarily on one of the BHs for about half a binary orbit. This is similar to flow features observed in [126]. The behavior has been attributed to a gradual increase of disk-eccentricity [36], which weakens one of the two streams when the BHs pass near the disk-apocenter and strengthens the other stream at pericenter.

Prior to decoupling, but after an initial transient phase ($5000M \lesssim t \lesssim t_{\rm vis}(R_{\rm in})$), the accretion rate $\dot{M}_{\rm BHBH}$ settles to values comparable to those onto a single BH of mass M (see Fig. 6.34). We perform a Fourier analysis of $\dot{M}_{BHBH}$ and find that the strongest contributions arise at $f \sim 2/3\Omega$ in both of our cases. This is likely associated with the dominant (2,3) Lindblad resonance [36]. During the early inspiral the inward drift of the disk edge lags behind the binary orbital decay, decreasing $\dot{M}_{BHBH}$. In contrast to the magnetic-free case [83], the accretion streams *remain present* until merger at t_m for the "no-cooling" case and up until $t - t_m \gtrsim -400M$ for the "cooling" case. At merger $\dot{M}_{\rm BHBH}$ decreases gradually to about 30% of the single, quasi-stationary BH accretion rate, $\dot{M}_{\rm BH}$ (see Fig. 6.34).

The remnant BH settles down via quasi-normal mode ringing to a Kerr-like BH with mass $M_f \sim 0.95M$ and dimensionless spin $s = J_f/M_f^2 = 0.68$. In the "cooling" case the inner disk edge reaches $R_{\rm in}(t_m) \sim 10M$

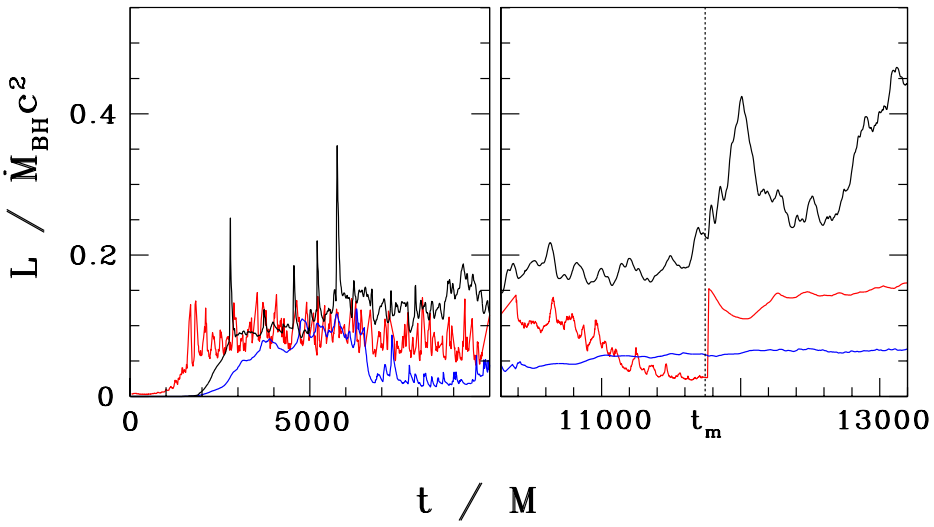

Figure 6.36: The Poynting luminosity L_{EM} measured at $R = 100M$ as a function of time (blue line for "cooling", black line for "no-cooling"). The cooling luminosity L_{cool} from the "cooling" case (red line). $\dot{M}_{\rm BH}c^2 = 2.58 \cdot 10^{46}{\rm ergs}^{-1} n_{12} M_8^2$.

at merger, while the edge is more dispersed in the "no-cooling" case (see Fig. 6.32).

Prior to decoupling we detect persistent, magnetized, mildly relativistic ($v \gtrsim 0.5c$) collimated outflows in the polar regions (see Fig. 6.35) in both cases. After merger there is an increase of the velocities in the outflow reaching Lorentz factors $W \lesssim 4$ for the "no-cooling" case, while the outflow in the "cooling" case remains relatively unchanged. These properties persist throughout the postmerger evolution. After merger the effective, turbulent viscous torque will cause the gas to refill the cavity and accrete on the merger remnant. Thus, brightening crucially depends on the surface density at decoupling. If there is only a small pile-up and the majority of gas lies at radii $R \gtrsim 40M$, then a significant brightening will take $t_{\rm vis}(R \gtrsim 40M) > \mathcal{O}(10^4 M)$ following merger. Using Eq. (6.48) we estimate $t_{\rm vis} \gtrsim 22000M$ ($\alpha \sim 0.13, H/R \sim 0.3$) for the "no-cooling" case and $t_{\rm vis} \gtrsim 6800M$ ($\alpha \sim 0.27, H/R = 0.17$) for the "cooling" case, respectively. We observe the surface density profile diffusing inward, but we have not followed the evolution for this long. The Poynting luminosity ($L_{\rm EM} \equiv \int -T^r_{t\,({\rm EM})} \sqrt{-g} dS$) across a sphere at $R = 100M$ and the (approximate) luminosity from disk cooling ($L_{cool} \equiv \int \Lambda u_t \sqrt{-g} d^3x$) are shown as functions of time in Fig. 6.36. We find a sudden enhancement in the Poynting luminosity for the "no-cooling" case beginning at merger and growing for $\lesssim 200M$. This enhancement originates from shocked gas in the immediate vicinity of the binary and escapes mainly through the polar regions. It is absent for the "cooling" case, for which there is less gas near the binary prior to merger. Heat generated by shocks is also removed in the cooling case, leaving less energy available for conversion to a Poynting flux. In Fig. (6.36) we also plot the cooling luminosity for the "cooling"

case, for which we also observe a sudden jump at merger. We find that the outward flux of kinetic energy is much smaller in both cases. Total efficiencies $\epsilon \equiv L/\dot{M}_{BH}c^2$ increase to $\epsilon = 0.25$ at merger. The Poynting luminosity is presumably reprocessed at larger distance from the remnant. The characteristic frequencies of the total emitted EM radiation will depend on the BH masses, disk densities and dominant cooling mechanisms.

Chapter 7

Summary, Discussion, and Future Work

In this thesis, we study merging black hole binaries in gaseous environments using fully relativistic (magneto)hydrodynamic simulations. This work is motivated by promise of multi-messenger astronomy, i.e. systems which may be observed in both electromagnetic and gravitational waves. We have restricted our attention to accretion onto equal-mass, nonspinning BH binaries, although our methods may be extended to other binary configurations.

As a first step, we focus on the limit in which the angular momentum of the gas can be neglected. We consider unmagnetized gas clouds which are asymptotically uniform and either at rest (BHBH Bondi accretion), or moving (BHBH BHL accretion) with respect to the binary center of mass. We perform "prototype" high-temperature ($T_\infty \sim 10^{11}$ K) simulations in order to gain a qualitative understanding of the different flow regimes characterizing such systems. In these simulations, the accretion radius R_a is placed within the computational domain, which allows us to sample all the various regimes, studying how the luminosity and accretion rate change when the binary separation d goes from $d > R_a$ to $d < R_a$. We also performed "realistic" simulations with astrophysically plausible asymptotic temperatures ($T_\infty = 10^6 K$) to identify observable electromagnetic signals. For each simulation, we calculatedthe time-varying rest-mass accretion rate, as well as the electromagnetic luminosity due to bremsstrahlung and synchrotron emission. We also derive scaling relations for the luminosity for the realistic cases, enabling our results to be used for different asymptotic gas parameters and BH masses. In each case, we find evidence for a time-varying electromagnetic signature accompanying the BHBH binary merger. For our "realistic" temperature simulations, we find that during the final inspiral from separation $d = 10M$ to merger, there is an enhancement in the total luminosity of $\sim 1 - 2$ orders of magnitude. This is followed by a sharp drop in the luminosity by a factor of $\sim 2 - 5$ orders of magnitude immediately following the merger. We find that the luminosity is dominated by the synchrotron component, and that this signature should be detectable by the proposed LSST instrument.

By solving the BHBH binary analogs of the classic Bondi and BHL accretion problems we have sought to lay a natural and rigorous foundation for our future simulations involving BHBH mergers in gaseous environments. Our focus here was to perform "prototype" simulations to identify the different regimes

characterizing the gas flow in these classic scenarios and then to perform a "realistic" simulation for a merger occuring in an astrophysically plausible gaseous setting. For the latter case we also determined the scaling behavior of the gas dynamical parameters, emitted luminosities and characteristic frequencies so that they could be used to apply our results to other environments.

As a next step, we consider unmagnetized disklike accretion flows in which the angular momentum of the disk plays an important role. We exploit the approximate helical Killing symmetry to determine the binary spacetime for widely separated BHBHs. The disk we evolve in this early inspiral spacetime relaxes to near quasiequilibrium. Our late inspiral and merger simulations begin with such a quasistationary disk. We then evolve the field as well as the matter. This epoch corresponds to the post disk-binary decoupling phase, terminating after merger, but before viscosity fills in the hollow.

For each simulation, we have calculated the time-varying rest-mass accretion rate, as well as the electromagnetic luminosity due to bremsstrahlung and synchrotron emission. We also derive scaling relations for the luminosity, enabling our results to be applied to a range of gas parameters and BH masses.

In each case, we find evidence for a time-varying electromagnetic signature accompanying the BHBH binary merger. The synchrotron emission is the most easily detectable component, and we observe a steady decline in synchrotron luminosity throughout the post-decoupling binary inspiral. This change serves as a characteristic precursor of a binary merger, and should be detectable by the proposed WFIRST and possibly by the LSST instrument.

It is instructive to compare the electromagnetic signatures associated with binary Bondi accretion with the signatures from disklike accretion discussed in this paper. In the binary Bondi case, there is a steady supply of gas accreting onto the binary at all stages of the merger. In this case, the evolution of the luminosity is determined by the strength of shock heating near the BHs. As the separation decreases, the BHs orbit more rapidly, and the shock-heated temperature of the gas increases. This increase leads to a luminosity that increases throughout the inspiral, then drops precipitously following the merger as the shocks dissipate. This scenario is quite different from the case of disklike accretion, in which binary torques create a hollow region around the binary as well as a small amount of matter that leaks into the hollow in the form of spiral arms. Because the torques decrease throughout the inspiral as the BH separation decreases, we find that the accretion rate and luminosity decrease steadily over the course of our inspiral simulations.

By introducing magnetic fields into our BHBH+disk simulations, we have been able to probe the pre-decoupling epoch of the binary inspiral. We have found that significant gas enters the cavity along a two stream accretion flow and that the quasistationary rest-mass accretion rate is comparable to that of a single BH+disk system. We find that following decoupling, the accretion rate is reduced, while the EM luminosities

peak near merger due to shock heating. We have also compared simulations with and without cooling and found significant modifications in the accretion flow. In future work, we intend to study the role of cooling in more detail, and to incorporate more realistic cooling prescriptions. We also intend to study other precursor (e.g. twin jets) and afterglow effects, different mass ratios, and different BH spins more thoroughly in future work. Finally, we plan to incorporate more advanced tools for accurately modeling the electromagnetic signatures of these systems (i.e. ray-tracing techniques).

Appendix A

Disk initial data

Our formulation for an equilibrium stationary disk around a *single* Kerr BH follows closely that of [93, 94].

From the conservation of the stress-energy equation, we find

$$0 = T^{\beta}{}_{\alpha;\beta} = \frac{1}{\alpha\sqrt{\gamma}}\left(\alpha\sqrt{\gamma}T_{\alpha}{}^{\beta}\right)_{,\beta} - \Gamma^{\lambda}_{\alpha\mu}T_{\lambda}{}^{\mu} \tag{A.1}$$

$$= \frac{1}{\alpha\sqrt{\gamma}}\left(\alpha\sqrt{\gamma}\rho_0 h u_{\alpha}u^{\beta}\right)_{,\beta} + P_{,\alpha} + \frac{1}{2}(g^{\mu\nu}{}_{,\alpha}\rho_0 h u_{\mu}u_{\nu}) \ . \tag{A.2}$$

Since we are seeking a solution for a stationary torus in Kerr spacetime for a single BH, we can now impose time independence, axisymmetry, and no poloidal or radial motion:

$$\partial_t(\ldots) = \partial_{\phi}(\ldots) = 0 \ , \tag{A.3}$$

$$u^r = u^{\theta} = 0 \ . \tag{A.4}$$

In Boyer-Lindquist and Kerr-Schild coordinates, these constraints imply that $u_r = u_{\theta} = 0$.

We may now simplify Eq. (A.2) according to

$$0 = \frac{h_{,j}}{h} - \frac{1}{2}u_t^2(u_t^{-2})_{,j} - \frac{\Omega}{1-l\Omega}l_{,j} \ . \tag{A.5}$$

Here we have also assumed constant entropy, and we have introduced the specific angular momentum $l \equiv -u_{\phi}/u_t$. We have also used the fact that $u^{\mu}u_{\mu} = -1$ to show that

$$u_t^{-2} = -(g^{tt} - 2lg^{t\phi} + l^2 g^{\phi\phi}) \ , \tag{A.6}$$

and have defined

$$\Omega \equiv u^{\phi}/u^t = (g^{t\phi} - lg^{\phi\phi})/(g^{tt} - lg^{t\phi}) \ . \tag{A.7}$$

We now follow [93, 94] and assume the disk has a power-law rotation dependence, whereby Ω takes the form

$$\Omega = \eta \lambda^{-q} \ , \tag{A.8}$$

where

$$\lambda^2 \equiv \frac{l}{\Omega} = l \frac{g^{tt} - l g^{t\phi}}{g^{t\phi} - l g^{\phi\phi}} \ . \tag{A.9}$$

Combining Eq. (A.8) and Eq. (A.9), we find that

$$\Omega = k l^{\alpha} \ , \tag{A.10}$$

where $\alpha \equiv q/(q-2)$ and $k = \eta^{-2/(q-2)}$.

It is now straightforward to show that Eq. (A.5) is satisfied by

$$h(r,\theta) = \frac{u_{t,in} f(l_{in})}{u_t(r,\theta) f(l(r,\theta))} \ , \tag{A.11}$$

where $f(l) = |1 - k l^{\alpha+1}|^{1/(\alpha+1)}$. A disk solution is uniquely determined for fixed R_{in}, $l(R_{in})$, and q.

While the solution described above applies to equilibrium disks in general Kerr spacetimes, we assume a Schwarzschild geometry for the purposes of this study.

In the Newtonian limit, we know that $l = \Omega r^2$, so $\lambda^2 = l/\Omega = r^2$, whereby

$$\Omega \propto \lambda^{-q} \propto r^{-q} \ . \tag{A.12}$$

Thus we can see that asymptotically,

$$q = 0 \quad \Rightarrow \quad \Omega = \text{const} \ , \tag{A.13}$$

$$q = 2 \quad \Rightarrow \quad l = \text{const} \ , \tag{A.14}$$

$$q = 1.5 \quad \Rightarrow \quad \text{Keplerian} \ . \tag{A.15}$$

Appendix B

Derivation of the torque density dT/dR

If we consider a four vector $\vec{j}$ that is not necessarily conserved, then we must generalize Eq. (4.4) to

$$\frac{dq}{dt} = -\mathcal{F}_H + \mathcal{F}_L + \int \sqrt{-g}\nabla_\mu j^\mu d^3x \tag{B.1}$$

If we choose to set H and L to be two concentric cylinders of infinite extent, centered around the z axis and of radius R and $R+\delta R$ respectively, we can rewrite Eq. (B.1) as

$$\frac{d}{dt}(q(R+\delta R) \quad - \quad q(R)) = -\mathcal{F}(R) + \mathcal{F}(R+\delta R) + \int \sqrt{-g}\nabla_\mu j^\mu R\ dR\ dz\ d\phi$$

taking the limit $\delta R \to 0$, we therefore find that

$$\frac{d}{dR}\left(\frac{dq}{dt}\right) = \frac{d\mathcal{F}}{dR} + \int \sqrt{-g}\nabla_\mu j^\mu R\ dz\ d\phi\ . \tag{B.2}$$

We can consider the specific case where $j^\mu = T^\mu{}_\nu \phi^\nu$, and $\phi^\nu \equiv (\partial_\phi)^\mu = (0, -y, x, 0)$, so that Eq. (B.2) becomes

$$\begin{aligned} \frac{d}{dR}\left(\frac{dJ}{dt}\right) &\equiv \frac{dT_{tot}}{dR} \\ &= \frac{d\mathcal{F}^{(J)}}{dR} + \int \sqrt{-g}T^{\mu\nu}\nabla_\mu \phi_\nu R dz d\phi\ . \end{aligned} \tag{B.3}$$

We interpret the first term on the right-hand side of Eq. (B.3) as arising from the net outflow of angular momentum carried by matter across the surfaces at R and $R+\delta R$, while the second term is the torque due to the gravitational field. Because we are most interested in the torque from the gravitational field of the binary, we define

$$\frac{dT}{dR} \equiv \frac{dT_{tot}}{dR} - \frac{d\mathcal{F}^{(J)}}{dR} = \int \sqrt{-g}T^{\mu\nu}\nabla_\mu \phi_\nu R\ dz\ d\phi\ . \tag{B.4}$$

Note that in an axisymmetric spacetime in which ϕ_ν is a Killing vector field, $T^{\mu\nu}\nabla_\mu\phi_\nu = T^{\mu\nu}\nabla_{(\mu}\phi_{\nu)} = 0$, hence $dT/dR = 0$ as expected.

In order to compute Eq. (B.4) numerically, it is convenient to transform the expression into Cartesian coordinates. Note that

$$\begin{aligned} T^{\mu\nu}\nabla_\mu\phi_\nu &= T^\mu{}_\nu\nabla_\mu\phi^\nu \\ &= T^\mu{}_\nu(\phi^\nu_{,\mu} + \Gamma^\nu{}_{\sigma\mu}\phi^\sigma) \\ &= T^\mu{}_\nu\phi^\nu_{,\mu} + \frac{1}{2}T^{\mu\nu}g_{\mu\nu,\sigma}\phi^\sigma \\ &= -T^\mu{}_x\ y_{,\mu} + T^\mu{}_y\ x_{,\mu} + \frac{1}{2}T^{\mu\nu}\left(-g_{\mu\nu,x}y + g_{\mu\nu,y}x\right) \\ &= -T^y{}_x + T^x{}_y - \frac{1}{2}yT^{\mu\nu}g_{\mu\nu,x} + \frac{1}{2}xT^{\mu\nu}g_{\mu\nu,y} \end{aligned} \tag{B.5}$$

Inserting Eq. (B.5) into Eq. (B.4), we find

$$\begin{aligned} \frac{dT}{dR} &= \int R\ d\phi\ dz\sqrt{-g}\left(-T^y{}_x + T^x{}_y\right) \\ &\quad + \frac{1}{2}\int R\ d\phi\ dz\sqrt{-g}\left(-yT^{\mu\nu}g_{\mu\nu,x} + xT^{\mu\nu}g_{\mu\nu,y}\right)\ . \end{aligned} \tag{B.6}$$

Eq. (B.6) is integrated numerically at a number of different radii, so that we can compute profiles of dT/dR.

B.1 Newtonian limit

We can check that Eq. (B.6) reduces to the correct expression in the Newtonian limit. If we let $T^{00} \approx \rho_0$, $|T^{0i}/T^{00}| \ll 1$, and $|T^{ij}/T^{00}| \ll 1$, we find

$$\begin{aligned} \frac{dT}{dR} &\approx \frac{1}{2}\int R\ d\phi\ dz\ T^{00}(-yg_{00,x} + xg_{00,y}) \\ &= \frac{1}{2}\int R\ d\phi\ dz\ T^{00}g_{00,\phi} \\ &= -\int R\ d\phi\ dz\ \rho_0\Phi_{,\phi} \\ &= -2\pi R\left\langle\Sigma\Phi_{,\phi}\right\rangle \end{aligned} \tag{B.7}$$

where angled brackets indicate angle averaging, and Φ is the Newtonian gravitational potential. Eq. (B.7) matches the expression given in Eq. (14) of [36].

Appendix C

Derivation of $\dot{M}$ Expression

Consider a 3D hypersurface F given by $f(t,x,y,z) = constant$ in a spacetime diagram (see Fig. C.1). The intersection of F with a t = constant time slice is a 2-surface $S(t)$. Below we will identify $S(t)$ to be the apparent horizon of a black hole at time t. Let L be a 3D hypersurface which is a worldtube enclosing F. Let us further define Σ_t to be the 3D region on the time slice t between the surface $S(t)$ and $\Omega(t)$, the 2D cross section of L on the time slice t. We can imagine a 4-volume $\mathcal{V}$ to be the region bounded by the hypersurfaces $\Sigma_{t_0}, \Sigma_{t_0+\delta t}, L$, and F. Consider a 4-vector flux j^μ with a vanishing divergence, $\nabla_\mu j^\mu = 0$. At a given time t, define the function $q(t)$ according to

$$q(t) = \int_{\Sigma_t} j^\mu d^3\Pi_\mu \tag{C.1}$$

From Gauss's law,

$$\begin{aligned} 0 &= \int_{\mathcal{V}} \nabla_\mu j^\mu d\mathcal{V} = \int_{\partial\mathcal{V}} j^\mu d^3\Pi_\mu \\ &= q(t_0+\delta t) - q(t_0) + \int_F j^\mu d^3\Pi_\mu - \int_L j^\mu d^3\Pi_\mu \ . \end{aligned} \tag{C.2}$$

To evaluate the integral on F, it is convenient to introduce a coordinate system (t, f, a, b), where $a =$

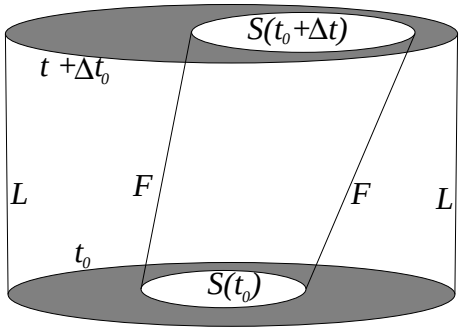

Figure C.1: Spacetime diagram depicting the hypersurfaces relevant to calculating the mass accretion rate. The 2D hypersurface $S(t_0)$ and $S(t_0+\Delta t)$ (white regions) represent BH horizons on neighboring time slices. They are enclosed by spacelike 3D hypersurfaces Σ_{t_0} and $\Sigma_{t_0+\Delta t}$ (shaded region) on these slices.

$a(t,x,y,z)$ and $b=b(t,x,y,z)$ are two other coordinates. We may write

$$\begin{aligned}\int_F j^\mu d^3\Pi_\mu &= \frac{1}{3!}\int j^\mu \epsilon_{\mu\nu\rho\sigma} dx^\nu dx^\rho dx^\sigma \\ &= \frac{1}{3!}\int j^f \epsilon_{ftab}\ dt\wedge da\wedge db \\ &= -\int \sqrt{-g'} j^f\ dtdadb \\ &= -\int \sqrt{-g} j^\mu \partial_\mu f J\ dtdadb\ , \end{aligned} \tag{C.3}$$

where g' is the determinant of the metric in the (t,f,a,b) coordinate system, g is the determinant in the (t,x,y,z) coordinate system, J is the Jacobian

$$J=\left|\frac{\partial(t,f,a,b)}{\partial(t,x,y,z)}\right|^{-1}=\left|\frac{\partial(f,a,b)}{\partial(x,y,z)}\right|^{-1}\ , \tag{C.4}$$

and $j^f=j^\mu\partial_\mu f$ follows from the usual transformation formula for a vector field between the (t,f,a,b) and (t,x,y,z) coordinate systems. Similarly, if L is given by $l(t,x,y,z)=0$, then

$$\int_L j^\mu d^3\Pi_\mu = -\int \sqrt{-g} j^\mu \partial_\mu l J_l\ dtdadb\ , \tag{C.5}$$

where $J_l=|\partial(l,a,b)/\partial(x,y,z)|^{-1}$. Taking the limit $\delta t\to 0$, we obtain

$$\frac{dq}{dt}=-\mathcal{F}_F+\mathcal{F}_L\ , \tag{C.6}$$

where

$$\mathcal{F}_F = -\int_F \sqrt{-g} j^\mu \partial_\mu f J\ dadb\ , \tag{C.7}$$

$$\mathcal{F}_L = -\int_L \sqrt{-g} j^\mu \partial_\mu l J_l\ dadb\ . \tag{C.8}$$

Consider a fluid accreting onto a BH. Let F be the BH horizon world tube. At any given time t, consider the fluid in the region Σ_t between the BH (apparent) horizon $S(t)$ and a distant 2-surface $\Omega(t)$ surrounding the BH. Let L be the 3D hypersurface formed by stacking Ω with time. The continuity equation gives $\nabla_\mu(\rho_0 u^\mu)=0$. Setting $j^\mu=\rho_0 u^\mu$, we have

$$q(t)=\int_{\Sigma_t}\rho_0 u^\mu d^3\Pi_\mu=\int_{\Sigma_t}\rho_* d^3x = M_0(t) \tag{C.9}$$

is the rest mass bounded by the surface Ω and the horizon, where $\rho_* = \sqrt{-g}\,\rho_0 u^0$. Hence we have

$$\frac{dM_0}{dt} = \mathcal{F}_L - \mathcal{F}_F \ . \tag{C.10}$$

This equation states that the rate of change of the rest mass is equal to the amount of rest mass flowing into Ω per unit time ($\mathcal{F}_L$) minus the amount of rest mass flowing into the horizon per unit time ($\mathcal{F}_F$). Hence we define the rest-mass accretion rate onto the BH according to

$$\dot{M} \equiv \mathcal{F}_F = -\int_F \alpha\sqrt{\gamma}\rho_0 u^\mu \partial_\mu f J d\theta d\phi \ , \tag{C.11}$$

Here we have used the identity $\sqrt{-g} = \alpha\sqrt{\gamma}$, and choose a and b to be the spherical angular coordinates θ and ϕ with the origin at the BH center.

It is apparent from the definition that in general $\dot{M}$ depends on how the spacetime is sliced near the horizon. However, in some cases $\dot{M}$ may be time independent. Consider the cases where the fluid's mass is negligible compared to the BH's mass and there exists a timelike Killing vector $\boldsymbol{\xi} = \partial/\partial\lambda$ in the vicinity of a BH. This Killing vector could be the time Killing vector describing a stationary BH, or a helical Killing vector which approximates the BHBH spacetime in the inspiral phase. One might choose to measure $\dot{M}$ using a coordinate system in which $t = \lambda$ (at least locally). In this case,

$$\dot{M} \equiv \dot{M}_\lambda = -\int_F \sqrt{-g_\lambda}\rho_0 u^f d\theta d\phi \ , \tag{C.12}$$

where g_λ is the determinant of the spacetime metric in the $(\lambda, f, \theta, \phi)$ coordinate system. Suppose the flow of the fluid also achieves a stationary state near the horizon in which $\partial_\lambda(\rho_0 u^f) = 0$ everywhere on F, i.e. $\rho_0 u^f = \rho_0 u^f(\theta, \phi)$ on F. Since $\partial_\lambda g_\lambda = 0$, $\dot{M}_\lambda$ is a constant independent of the coordinate time λ. On the other hand, in a coordinate system in which λ is not the time coordinate, we have

$$\dot{M} = -\int_F \sqrt{-g'}\rho_0 u^f d\theta d\phi = -\int_F (\xi^t)^{-1}\sqrt{-g_\lambda}\rho_0 u^f d\theta d\phi \ , \tag{C.13}$$

where $g' = g_\lambda/(\xi^t)^2$ is the determinant of the spacetime metric in the (t, f, θ, ϕ) coordinate system, and ξ^t is the time component of the Killing vector $\boldsymbol{\xi}$. Note that both g_λ and $\rho_0 u^f$ are still time independent on F, but $\dot{M}$ is time dependent if ξ^t is time dependent. The accretion rate $\dot{M}$ is time independent only if a gauge is chosen so that $\partial_t \xi^t = 0$ on F. Furthermore, if ξ^t is constant everywhere on F, then $\dot{M} = \dot{M}_\lambda/\xi^t_h$, where ξ^t_h is the value of ξ^t on F. As an example, consider a stationary accretion flow onto a Kerr BH. In

the boosted Kerr-Schild coordinates, we have $\xi^t = \gamma_b = 1/\sqrt{1-v_b^2}$ everywhere in the spacetime, where v_b is the boost velocity. Hence we have $\dot{M} = \dot{M}_\lambda/\gamma_b$ in the boosted Kerr-Schild coordinates.

We point out that in a numerical simulation, even if a Killing vector exists, the adopted gauge (i.e. time slicing) may not correspond to the gauge in which $\partial/\partial t$ is the Killing vector. However, in some situations there exists a gauge in which a (quasi)stationary flow is expected. Such situations include the Bondi accretion onto a BHBH binary in the inspiring phase and the Bondi accretion onto a single BH following the binary merger. In these situations, the mass accretion rate onto a distant, fixed surface Ω (i.e. $\mathcal{F}_L$) is time independent for any gauge choices that give rise to a spacetime that is asymptotically Minkowsky. A "well-behaved" gauge should give a $\mathcal{F}_F$ (or the sum of two $\mathcal{F}_F$'s in the BHBH case) equal to $\mathcal{F}_L$ (when averaged over time); otherwise, Eq. (C.10) implies that there will be an accumulation (if $\mathcal{F}_F < \mathcal{F}_L$) or depletion (if $\mathcal{F}_F > \mathcal{F}_L$) of rest mass in the interior of Ω as a result of a pure gauge effect. In our numerical simulations, we do not see such a gauge effect. We compute $\mathcal{F}_L$ on spherical surfaces of various radii. We find that after the flow reaches a (quasi)stationary state, $\mathcal{F}_L$ is slowly changing with time in the binary inspirling phase and is approximately time independent after merger. The computed fluxes at various radii are also the same. Moreover, the sum of the computed fluxes at the BH horizons agree with the value $\mathcal{F}_L$, indicating that our adopted puncture gauge conditions are well-behaved.

Appendix D

Emissivities

D.1 Bremsstrahlung emissivity

In order to estimate the electromagnetic emission due to bremsstrahlung, we use the following expressions for electron-ion, and electron-electron cooling rates given in [127]

$$q_{ff} = q_{ei} + q_{ee} \tag{D.1}$$

$$q_{ei} = n^2 \frac{8\pi}{3} (\alpha_f r_e^2 c)\ (m_e c^2) F_{ei}(\theta)\ \text{ergs cm}^{-3}\ \text{s}^{-1} \tag{D.2}$$

$$q_{ee} = n^2 (\alpha_f r_e^2 c)(m_e c^2) F_{ee}(\theta)\ \text{ergs cm}^{-3}\ \text{s}^{-1} \tag{D.3}$$

Here, $\alpha_f = e^2/\hbar c$ is the fine structure constant, $r_e = e^2/m_e c^2$ is the classical electron radius, $\theta \equiv kT/m_e c^2$, $n = \rho_0/m_B$ is the baryon number density, and

$$F_{ei}(\theta) = \begin{cases} 4\left(\dfrac{2\theta}{\pi^3}\right)^{1/2} (1 + 1.781\ \theta^{1.34}) & \theta < 1 \\ \dfrac{9\theta}{2\pi}[\ln(1.123\theta + 0.48) + 1.5] & \theta > 1 \end{cases} \tag{D.4}$$

$$F_{ee}(\theta) = \begin{cases} \dfrac{20}{9\pi^{1/2}}(44 - 3\pi^2)\theta^{3/2} \\ \times(1 + 1.1\theta + \theta^2 - 1.25\ \theta^{5/2}) & \theta < 1 \\ 24\theta(\ln\ 1.123\theta + 1.28) & \theta > 1\ . \end{cases} \tag{D.5}$$

D.2 Synchrotron emissivity

We use the estimates for synchrotron cooling rates given by [128]:

$$q_{\nu,\text{S}} = \frac{4\pi n e^2 \nu}{\sqrt{3} c K_2(1/\theta)} I\left(\frac{x_M}{\sin\theta}\right) \text{ergs cm}^{-3}\ \ \text{s}^{-1}\ \ \text{Hz}^{-1}\ , \tag{D.6}$$

where

$$\nu_0 = \frac{eB}{2\pi m_e c} = \text{cyclotron frequency} \tag{D.7}$$

$$x_M = \frac{2\nu}{3\nu_0\theta^2} \ . \tag{D.8}$$

From [129], we get the following approximation for $I(x_M)$.

$$I(x_M) = 2.561\left(1+\frac{1.92}{x_M^{1/3}}+\frac{0.9977}{x_M^{2/3}}\right)\exp(-1.8899x_M^{1/3}) \ , \tag{D.9}$$

and the angle averaged version,

$$I'(x_M) = \frac{4.0505}{x_M^{1/6}}\left(1+\frac{0.40}{x_M^{1/4}}+\frac{0.5316}{x_M^{1/2}}\right)\exp(-1.8899x_M^{1/3}) \ . \tag{D.10}$$

We integrate over frequency to get the total cooling rate.

Let us denote,

$$A = 4.0505\frac{4\pi ne^2}{\sqrt{3}cK_2(1/(\theta))} \tag{D.11}$$

$$a_1 = \frac{2}{3\nu_0\theta^2} \tag{D.12}$$

$$a_2 = 1.8899 \ . \tag{D.13}$$

Thus, we see,

$$\begin{aligned}\int_0^\infty q_{\nu,\mathrm{S}}d\nu &= \frac{A}{a_1^2}\int_0^\infty x_M^{5/6}\left(1+\frac{0.4}{x_M^{1/4}}+\frac{0.5316}{x_M^{1/2}}\right) \\ &\qquad \times \exp\left(-a_2x_M^{1/3}\right)dx_M \\ &= \frac{3AC}{a_1^2}\end{aligned} \tag{D.14}$$

Where

$$C \equiv \frac{\Gamma(11/2)}{a_2^{11/2}}+\frac{0.4\ \Gamma(19/4)}{a_2^{19/4}}+\frac{0.5316\ \Gamma(4)}{a_2^4} = 2.151889 \tag{D.15}$$

Thus, we find

$$q_{\mathrm{S}} = \int_0^\infty q_{\nu,\mathrm{S}}d\nu = 4.0505\ C\frac{108n^2e^4c}{\sqrt{3}K_2(1/\theta)}\frac{\theta^5}{\beta m_e c^2} \ . \tag{D.16}$$

Here we have used

$$P = \beta P_M \equiv \beta \frac{B^2}{8\pi} \ . \tag{D.17}$$

As discussed in Sec. 4, we have chosen $\beta = 10$ for our simulations based on simulations of magnetized accretion flows which have demonstrated that the magnetic fields do not typically reach their full equipartition value [102]. We further assume that the hydrodynamic flow is turbulent due to the magneto-rotational instability (MRI), causing the frozen-in field lines to be tangled, and randomly oriented [108]. This justifies our use of the angle averaged function in Eq. (D.10). Note that for $x \ll 1$, $K_2(x) \approx 2/x^2$, so that for sufficiently large temperatures we may approximate:

$$q_{\rm S} \approx \int_0^\infty q_{\nu,{\rm S}} d\nu = 4.0505 \ C \frac{54 n^2 e^4 c}{\sqrt{3}} \frac{\theta^3}{\beta m_e c^2} \ . \tag{D.18}$$

References

[1] D. Richstone, E. A. Ajhar, R. Bender, G. Bower, A. Dressler, S. M. Faber, A. V. Filippenko, K. Gebhardt, R. Green, L. C. Ho, J. Kormendy, T. R. Lauer, J. Magorrian, and S. Tremaine. Supermassive black holes and the evolution of galaxies. *Nature*, 395:A14+, October 1998.

[2] B. M. Peterson and A. Wandel. Evidence for Supermassive Black Holes in Active Galactic Nuclei from Emission-Line Reverberation. *Astrophys. J. Lett.* , 540:L13–L16, September 2000.

[3] L. Ferrarese and H. Ford. Supermassive Black Holes in Galactic Nuclei: Past, Present and Future Research. *Space Science Reviews*, 116:523–624, February 2005.

[4] M. C. Begelman, R. D. Blandford, and M. J. Rees. Massive black hole binaries in active galactic nuclei. *Nature*, 287:307–309, September 1980.

[5] N. Roos. Galaxy mergers and active galactic nuclei. *Astron. and Astrophys.* , 104:218–228, December 1981.

[6] D. Merritt and M. Milosavljević. Massive Black Hole Binary Evolution. *Living Reviews in Relativity*, 8:8–+, November 2005.

[7] M. Milosavljević and E. S. Phinney. The Afterglow of Massive Black Hole Coalescence. *Astrophys. J. Lett.* , 622:L93–L96, April 2005.

[8] E. M. Rossi, G. Lodato, P. J. Armitage, J. E. Pringle, and A. R. King. Black hole mergers: the first light. *Mon. Not. R. Astron. Soc.* , pages 1726–+, November 2009.

[9] J. D. Schnittman and J. H. Krolik. The Infrared Afterglow of Supermassive Black Hole Mergers. *Astrophys. J.*, 684:835–844, September 2008.

[10] L. R. Corrales, Z. Haiman, and A. MacFadyen. Hydrodynamical response of a circumbinary gas disc to black hole recoil and mass loss. *Mon. Not. R. Astron. Soc.* , 404:947–962, May 2010.

[11] S. M. O'Neill, M. C. Miller, T. Bogdanović, C. S. Reynolds, and J. D. Schnittman. Reaction of Accretion Disks to Abrupt Mass Loss During Binary Black Hole Merger. *Astrophys. J.*, 700:859–871, July 2009.

[12] S. L. Shapiro. Filling the disk hollow following binary black hole merger: The transient accretion afterglow. *Phys. Rev. D*, 81(2):024019–+, January 2010.

[13] T. Tanaka and K. Menou. Time-dependent Models for the Afterglows of Massive Black Hole Mergers. *Astrophys. J.*, 714:404–422, May 2010.

[14] P. J. Armitage and P. Natarajan. Accretion during the Merger of Supermassive Black Holes. *Astrophys. J. Lett.* , 567:L9–L12, March 2002.

[15] P. Chang, L. E. Strubbe, K. Menou, and E. Quataert. Fossil gas and the electromagnetic precursor of supermassive binary black hole mergers. *Mon. Not. R. Astron. Soc.* , 407:2007–2016, September 2010.

[16] B. D. Farris, Y. T. Liu, and S. L. Shapiro. Binary black hole mergers in gaseous environments: "Binary Bondi" and "binary Bondi-Hoyle-Lyttleton" accretion. *Phys. Rev. D*, 81(8):084008–+, April 2010.

[17] H. L. Maness, G. B. Taylor, R. T. Zavala, A. B. Peck, and L. K. Pollack. Breaking All the Rules: The Compact Symmetric Object 0402+379. *Astrophys. J.*, 602:123–134, February 2004.

[18] C. Rodriguez, G. B. Taylor, R. T. Zavala, A. B. Peck, L. K. Pollack, and R. W. Romani. A Compact Supermassive Binary Black Hole System. *Astrophys. J.*, 646:49–60, July 2006.

[19] C. Rodriguez, G. B. Taylor, R. T. Zavala, Y. M. Pihlström, and A. B. Peck. H I Observations of the Supermassive Binary Black Hole System in 0402+379. *Astrophys. J.*, 697:37–44, May 2009.

[20] H. J. Lehto and M. J. Valtonen. OJ 287 Outburst Structure and a Binary Black Hole Model. *Astrophys. J.*, 460:207–+, March 1996.

[21] M. J. Valtonen, H. J. Lehto, A. Sillanpää, K. Nilsson, S. Mikkola, R. Hudec, M. Basta, H. Teräsranta, S. Haque, and H. Rampadarath. Predicting the Next Outbursts of OJ 287 in 2006-2010. *Astrophys. J.*, 646:36–48, July 2006.

[22] M. J. Valtonen et al. A massive binary black-hole system in OJ287 and a test of general relativity. *Nature*, 452:851–853, April 2008.

[23] T. Bogdanović, M. Eracleous, and S. Sigurdsson. SDSS J092712.65+294344.0: Recoiling Black Hole or a Subparsec Binary Candidate? *Astrophys. J.*, 697:288–292, May 2009.

[24] M. Dotti, C. Montuori, R. Decarli, M. Volonteri, M. Colpi, and F. Haardt. SDSSJ092712.65+294344.0: a candidate massive black hole binary. *Mon. Not. R. Astron. Soc.* , 398:L73–L77, September 2009.

[25] S. Komossa, H. Zhou, and H. Lu. A Recoiling Supermassive Black Hole in the Quasar SDSS J092712.65+294344.0? *Astrophys. J. Lett.* , 678:L81–L84, May 2008.

[26] T. A. Boroson and T. R. Lauer. A candidate sub-parsec supermassive binary black hole system. *Nature*, 458:53–55, March 2009.

[27] X. Liu, Y. Shen, and M. A. Strauss. Cosmic Train Wreck by Massive Black Holes: Discovery of a kpc-Scale Triple Active Galactic Nucleus. *ArXiv e-prints*, April 2011.

[28] B. Kocsis, Z. Haiman, and K. Menou. Premerger Localization of Gravitational Wave Standard Sirens with LISA: Triggered Search for an Electromagnetic Counterpart. *Astrophys. J.*, 684:870–887, September 2008.

[29] C. Deffayet and K. Menou. Probing Gravity with Spacetime Sirens. *Astrophys. J. Lett.* , 668:L143–L146, October 2007.

[30] D. E. Holz and S. A. Hughes. Using Gravitational-Wave Standard Sirens. *Astrophys. J.*, 629:15–22, August 2005.

[31] B. Kocsis, Z. Frei, Z. Haiman, and K. Menou. Finding the Electromagnetic Counterparts of Cosmological Standard Sirens. *Astrophys. J.*, 637:27–37, January 2006.

[32] T. Tanaka, Z. Haiman, and K. Menou. Witnessing the Birth of a Quasar. *Astron. J. Supp.* , 140:642–651, August 2010.

[33] P. Artymowicz and S. H. Lubow. Dynamics of binary-disk interaction. 1: Resonances and disk gap sizes. *Astrophys. J.*, 421:651–667, February 1994.

[34] R. Günther and W. Kley. Circumbinary disk evolution. *Astron. and Astrophys.* , 387:550–559, May 2002.

[35] A. Escala, R. B. Larson, P. S. Coppi, and D. Mardones. The Role of Gas in the Merging of Massive Black Holes in Galactic Nuclei. II. Black Hole Merging in a Nuclear Gas Disk. *Astrophys. J.*, 630:152–166, September 2005.

[36] A. I. MacFadyen and M. Milosavljević. An Eccentric Circumbinary Accretion Disk and the Detection of Binary Massive Black Holes. *Astrophys. J.*, 672:83–93, January 2008.

[37] M. Megevand, M. Anderson, J. Frank, E. W. Hirschmann, L. Lehner, S. L. Liebling, P. M. Motl, and D. Neilsen. Perturbed disks get shocked: Binary black hole merger effects on accretion disks. *Phys. Rev. D*, 80(2):024012–+, July 2009.

[38] M. Campanelli, C. O. Lousto, Y. Zlochower, and D. Merritt. Maximum Gravitational Recoil. *Physical Review Letters*, 98(23):231102–+, June 2007.

[39] T. Bogdanović, C. S. Reynolds, and M. C. Miller. Alignment of the Spins of Supermassive Black Holes Prior to Coalescence. *Astrophys. J. Lett.* , 661:L147–L150, June 2007.

[40] M. Anderson, L. Lehner, M. Megevand, and D. Neilsen. Post-merger electromagnetic emissions from disks perturbed by binary black holes. *Phys. Rev. D*, 81(4):044004–+, February 2010.

[41] G. A. Shields and E. W. Bonning. Powerful Flares from Recoiling Black Holes in Quasars. *Astrophys. J.*, 682:758–766, August 2008.

[42] Z. Lippai, Z. Frei, and Z. Haiman. Prompt Shocks in the Gas Disk around a Recoiling Supermassive Black Hole Binary. *Astrophys. J. Lett.* , 676:L5–L8, March 2008.

[43] O. Zanotti, L. Rezzolla, L. Del Zanna, and C. Palenzuela. Electromagnetic counterparts of recoiling black holes: general relativistic simulations of non-Keplerian discs. *Astron. and Astrophys.* , 523:A8+, November 2010.

[44] J. R. van Meter, J. H. Wise, M. C. Miller, C. S. Reynolds, J. Centrella, J. G. Baker, W. D. Boggs, B. J. Kelly, and S. T. McWilliams. Modeling Flows around Merging Black Hole Binaries. *Astrophys. J. Lett.* , 711:L89–L93, March 2010.

[45] P. Mösta, C. Palenzuela, L. Rezzolla, L. Lehner, S. Yoshida, and D. Pollney. Vacuum electromagnetic counterparts of binary black-hole mergers. *Phys. Rev. D*, 81(6):064017–+, March 2010.

[46] C. Palenzuela, L. Lehner, and S. L. Liebling. Dual Jets from Binary Black Holes. *Science*, 329:927–930, August 2010.

[47] T. Bode, R. Haas, T. Bogdanović, P. Laguna, and D. Shoemaker. Relativistic Mergers of Supermassive Black Holes and Their Electromagnetic Signatures. *Astrophys. J.*, 715:1117–1131, June 2010.

[48] T. Bogdanovic, T. Bode, R. Haas, P. Laguna, and D. Shoemaker. Properties of Accretion Flows Around Coalescing Supermassive Black Holes. *ArXiv e-prints*, October 2010.

[49] T. Bode, T. Bogdanovic, R. Haas, J. Healy, P. Laguna, and D. Shoemaker. Mergers of Supermassive Black Holes in Astrophysical Environments. *ArXiv e-prints*, January 2011.

[50] Masaru Shibata and Takashi Nakamura. Evolution of three-dimensional gravitational waves: Harmonic slicing case. *Phys. Rev. D*, 52(10):5428–5444, Nov 1995.

[51] Thomas W. Baumgarte and Stuart L. Shapiro. On the numerical integration of einstein's field equations. *Physical Review D*, 59:024007, 1999.

[52] H. Friedrich. On the hyperbolicity of Einstein's and other gauge field equations. *Communications in Mathematical Physics*, 100:525–543, December 1985.

[53] D. Garfinkle. Harmonic coordinate method for simulating generic singularities. *Phys. Rev. D*, 65(4):044029–+, February 2002.

[54] F. Pretorius. Numerical relativity using a generalized harmonic decomposition. *Classical and Quantum Gravity*, 22:425–451, January 2005.

[55] F. Pretorius. Evolution of Binary Black-Hole Spacetimes. *Physical Review Letters*, 95(12):121101–+, September 2005.

[56] M. Campanelli, C. O. Lousto, P. Marronetti, and Y. Zlochower. Accurate Evolutions of Orbiting Black-Hole Binaries without Excision. *Physical Review Letters*, 96(11):111101–+, March 2006.

[57] J. G. Baker, J. Centrella, D.-I. Choi, M. Koppitz, and J. van Meter. Gravitational-Wave Extraction from an Inspiraling Configuration of Merging Black Holes. *Physical Review Letters*, 96(11):111102–+, March 2006.

[58] L. Blanchet, G. Faye, B. R. Iyer, and S. Sinha. The third post-Newtonian gravitational wave polarizations and associated spherical harmonic modes for inspiralling compact binaries in quasi-circular orbits. *Classical and Quantum Gravity*, 25(16):165003–+, August 2008.

[59] B. Aylott et al. Testing gravitational-wave searches with numerical relativity waveforms: results from the first Numerical INJection Analysis (NINJA) project. *Classical and Quantum Gravity*, 26(16):165008–+, August 2009.

[60] I. D. Novikov and K. S. Thorne. Astrophysics of black holes. In *Black Holes (Les Astres Occlus)*, pages 343–450, 1973.

[61] P. E. J. Nulsen and A. C. Fabian. Fuelling quasars with hot gas. *Mon. Not. R. Astron. Soc.* , 311:346–356, January 2000.

[62] H. Bondi. On spherically symmetrical accretion. *Mon. Not. R. Astron. Soc.* , 112:195–+, 1952.

[63] F. C. Michel. Accretion of Matter by Condensed Objects. *Astrophys. Space Sci.* , 15:153–160, January 1972.

[64] S. L. Shapiro. Accretion onto Black Holes: the Emergent Radiation Spectrum. *Astrophys. J.*, 180:531–546, March 1973.

[65] S. L. Shapiro and S. A. Teukolsky. *Black holes, white dwarfs, and neutron stars: The physics of compact objects*. Wiley, New York, 1983.

[66] F. Hoyle and R. A. Lyttleton. The effect of interstellar matter on climatic variation. In *Proceedings of the Cambridge Philosophical Society*, volume 35 of *Proceedings of the Cambridge Philosophical Society*, pages 405–+, 1939.

[67] H. Bondi and F. Hoyle. On the mechanism of accretion by stars. *Mon. Not. R. Astron. Soc.* , 104:273–+, 1944.

[68] L. I. Petrich, S. L. Shapiro, R. F. Stark, and S. A. Teukolsky. Accretion onto a moving black hole - A fully relativistic treatment. *Astrophys. J.*, 336:313–349, January 1989.

[69] R. Hunt. A fluid dynamical study of the accretion process. *Mon. Not. R. Astron. Soc.* , 154:141–+, 1971.

[70] E. Shima, T. Matsuda, H. Takeda, and K. Sawada. Hydrodynamic calculations of axisymmetric accretion flow. *Mon. Not. R. Astron. Soc.* , 217:367–386, November 1985.

[71] J. A. Font and J. M. A. Ibanez. A Numerical Study of Relativistic Bondi-Hoyle Accretion onto a Moving Black Hole: Axisymmetric Computations in a Schwarzschild Background. *Astrophys. J.*, 494:297–+, February 1998.

[72] J. D. Larwood and J. C. B. Papaloizou. The hydrodynamical response of a tilted circumbinary disc: linear theory and non-linear numerical simulations. *Mon. Not. R. Astron. Soc.* , 285:288–302, February 1997.

[73] P. B. Ivanov, J. C. B. Papaloizou, and A. G. Polnarev. The evolution of a supermassive binary caused by an accretion disc. *Mon. Not. R. Astron. Soc.* , 307:79–90, July 1999.

[74] Y. T. Liu and S. L. Shapiro. Accretion disks around binary black holes: A quasistationary model. *Phys. Rev. D*, 82(12):123011–+, December 2010.

[75] H. P. Pfeiffer and J. W. York. Extrinsic curvature and the Einstein constraints. *Phys. Rev. D*, 67(4):044022–+, February 2003.

[76] G. B. Cook and H. P. Pfeiffer. Excision boundary conditions for black-hole initial data. *Phys. Rev. D*, 70(10):104016–+, November 2004.

[77] T. W. Baumgarte and S. L. Shapiro. *Numerical Relativity: Solving Einstein's Equations on the Computer*. Cambridge University Press, Cambridge, 2010.

[78] B. Kocsis, Z. Haiman, and A. Loeb. Gas pile up and overflow in circumbinary accretion disks: Type-I.5 migration. *ArXiv e-prints*, May 2012.

[79] R. R. Rafikov. Structure and evolution of circumbinary disks around supermassive black hole (SMBH) binaries. *eprint arXiv:1205.5017*, May 2012.

[80] S. A. Balbus and J. F. Hawley. Instability, turbulence, and enhanced transport in accretion disks. *Reviews of Modern Physics*, 70:1–53, January 1998.

[81] S. C. Noble, B. C. Mundim, H. Nakano, J. H. Krolik, M. Campanelli, Y. Zlochower, and N. Yunes. Circumbinary MHD Accretion into Inspiraling Binary Black Holes. *ArXiv e-prints*, April 2012.

[82] C. Roedig, A. Sesana, M. Dotti, J. Cuadra, P. Amaro-Seoane, and F. Haardt. Evolution of binary black holes in self gravitating discs: dissecting the torques. *ArXiv e-prints*, February 2012.

[83] B. D. Farris, Y. T. Liu, and S. L. Shapiro. Binary black hole mergers in gaseous disks: Simulations in general relativity. *Phys. Rev. D*, 84(2):024024, July 2011.

[84] R. Arnowitt, S. Deser, and C. W. Misner. Republication of: The dynamics of general relativity. *General Relativity and Gravitation*, 40:1997–2027, September 2008.

[85] J. R. van Meter, J. G. Baker, M. Koppitz, and D.-I. Choi. How to move a black hole without excision: Gauge conditions for the numerical evolution of a moving puncture. *Phys. Rev. D*, 73(12):124011–+, June 2006.

[86] Z. B. Etienne, J. A. Faber, Y. T. Liu, S. L. Shapiro, and T. W. Baumgarte. Filling the holes: Evolving excised binary black hole initial data with puncture techniques. *Phys. Rev. D*, 76(10):101503–+, November 2007.

[87] G. Tóth. The del.B=0 Constraint in Shock-Capturing Magnetohydrodynamics Codes. *Journal of Computational Physics*, 161:605–652, July 2000.

[88] M. Anderson, E. W. Hirschmann, S. L. Liebling, and D. Neilsen. Relativistic MHD with adaptive mesh refinement. *Classical and Quantum Gravity*, 23:6503–6524, November 2006.

[89] M. D. Duez, Y. T. Liu, S. L. Shapiro, and B. C. Stephens. Relativistic magnetohydrodynamics in dynamical spacetimes: Numerical methods and tests. *Phys. Rev. D*, 72(2):024028–+, July 2005.

[90] M. Ansorg, B. Brügmann, and W. Tichy. Single-domain spectral method for black hole puncture data. *Phys. Rev. D*, 70(6):064011–+, September 2004.

[91] W. Tichy and B. Brügmann. Quasiequilibrium binary black hole sequences for puncture data derived from helical Killing vector conditions. *Phys. Rev. D*, 69(2):024006–+, January 2004.

[92] W. Tichy and P. Marronetti. Final mass and spin of black-hole mergers. *Phys. Rev. D*, 78(8):081501–+, October 2008.

[93] S. K. Chakrabarti. The natural angular momentum distribution in the study of thick disks around black holes. *Astrophys. J.*, 288:1–6, January 1985.

[94] J.-P. De Villiers, J. F. Hawley, and J. H. Krolik. Magnetically Driven Accretion Flows in the Kerr Metric. I. Models and Overall Structure. *Astrophys. J.*, 599:1238–1253, December 2003.

[95] `http://www.cactuscode.org/`.

[96] E. Schnetter, S. H. Hawley, and I. Hawke. Evolutions in 3D numerical relativity using fixed mesh refinement. *Classical and Quantum Gravity*, 21:1465–1488, March 2004.

[97] J. Thornburg. A fast apparent horizon finder for three-dimensional Cartesian grids in numerical relativity. *Classical and Quantum Gravity*, 21:743–766, January 2004.

[98] P. Colella and P. R. Woodward. The Piecewise Parabolic Method (PPM) for Gas-Dynamical Simulations. *Journal of Computational Physics*, 54:174–201, September 1984.

[99] A. Harten, P. D. Lax, and van Leer. B. J. On Upstream Differencing and Godunov-Type Schemes for Hyperbolic Conservation Laws. *SIAM Rev.*, 25:35, 1983.

[100] Z. B. Etienne, J. A. Faber, Y. T. Liu, S. L. Shapiro, K. Taniguchi, and T. W. Baumgarte. Fully general relativistic simulations of black hole-neutron star mergers. *Phys. Rev. D*, 77(8):084002–+, April 2008.

[101] M. Shibata, M. D. Duez, Y. T. Liu, S. L. Shapiro, and B. C. Stephens. Magnetized Hypermassive Neutron-Star Collapse: A Central Engine for Short Gamma-Ray Bursts. *Physical Review Letters*, 96(3):031102–+, January 2006.

[102] J. C. McKinney and C. F. Gammie. A Measurement of the Electromagnetic Luminosity of a Kerr Black Hole. *Astrophys. J.*, 611:977–995, August 2004.

[103] Y. T. Liu, S. L. Shapiro, and B. C. Stephens. Magnetorotational collapse of very massive stars to black holes in full general relativity. *Phys. Rev. D*, 76(8):084017–+, October 2007.

[104] Z. B. Etienne, Y. T. Liu, S. L. Shapiro, and T. W. Baumgarte. General relativistic simulations of black-hole-neutron-star mergers: Effects of black-hole spin. *Phys. Rev. D*, 79(4):044024–+, February 2009.

[105] J. A. Faber, T. W. Baumgarte, Z. B. Etienne, S. L. Shapiro, and K. Taniguchi. Relativistic hydrodynamics in the presence of puncture black holes. *Phys. Rev. D*, 76(10):104021–+, November 2007.

[106] B. D. Farris, T. K. Li, Y. T. Liu, and S. L. Shapiro. Relativistic radiation magnetohydrodynamics in dynamical spacetimes: Numerical methods and tests. *Phys. Rev. D*, 78(2):024023–+, July 2008.

[107] M. Campanelli, C. O. Lousto, and Y. Zlochower. Last orbit of binary black holes. *Phys. Rev. D*, 73(6):061501–+, March 2006.

[108] S. L. Shapiro. Accretion onto Black Holes: the Emergent Radiation Spectrum. II. Magnetic Effects. *Astrophys. J.*, 185:69–82, October 1973.

[109] S. L. Shapiro. Accretion onto Black Holes: the Emergent Radiation Spectrum. III. Rotating (kerr) Black Holes. *Astrophys. J.*, 189:343–352, April 1974.

[110] T. W. Baumgarte. Innermost stable circular orbit of binary black holes. *Phys. Rev. D*, 62(2):024018–+, July 2000.

[111] L. D. Landau and E. M. Lifshitz. *Fluid mechanics*. Elsevier, Oxford, 1959.

[112] `http://www.lsst.org`.

[113] K. Hayasaki, S. Mineshige, and H. Sudou. Binary Black Hole Accretion Flows in Merged Galactic Nuclei. *PASJ*, 59:427–441, April 2007.

[114] C. Roedig, M. Dotti, A. Sesana, J. Cuadra, and M. Colpi. Limiting eccentricity of sub-parsec massive black hole binaries surrounded by self-gravitating gas discs. *ArXiv e-prints*, April 2011.

[115] D. N. C. Lin, J. C. B. Papaloizou, and G. J. Savonije. Wave propagation in gaseous accretion disks. *Astrophys. J.*, 364:326–334, November 1990.

[116] D. N. C. Lin, J. C. B. Papaloizou, and G. J. Savonije. Propagation of tidal disturbance in gaseous accretion disks. *Astrophys. J.*, 365:748–756, December 1990.

[117] N. I. Shakura and R. A. Sunyaev. Black holes in binary systems. Observational appearance. *Astron. and Astrophys.* , 24:337–355, 1973.

[118] N. Bode and S. Phinney. Variability in Circumbinary Disks Following Massive Black Hole Mergers. *APS Meeting Abstracts*, pages 1010–+, April 2007.

[119] `http://wfirst.gsfc.nasa.gov/`.

[120] Z. B. Etienne, Y. T. Liu, and S. L. Shapiro. Relativistic magnetohydrodynamics in dynamical spacetimes: A new adaptive mesh refinement implementation. *Phys. Rev. D*, 82(8):084031, October 2010.

[121] Z. B. Etienne, Y. T. Liu, V. Paschalidis, and S. L. Shapiro. General relativistic simulations of black-hole-neutron-star mergers: Effects of magnetic fields. *Phys. Rev. D*, 85(6):064029, March 2012.

[122] Zachariah B. Etienne, Vasileios Paschalidis, Yuk Tung Liu, and Stuart L. Shapiro. Relativistic MHD in dynamical spacetimes: Improved EM gauge condition for AMR grids. *Phys.Rev.*, D85:024013, 2012.

[123] V. Paschalidis, Y. T. Liu, Z. Etienne, and S. L. Shapiro. Merger of binary white dwarf-neutron stars: Simulations in full general relativity. *Phys. Rev. D*, 84(10):104032, November 2011.

[124] R. F. Penna, J. C. McKinney, R. Narayan, A. Tchekhovskoy, R. Shafee, and J. E. McClintock. Simulations of magnetized discs around black holes: effects of black hole spin, disc thickness and magnetic field geometry. *Mon. Not. R. Astron. Soc.* , 408:752–782, October 2010.

[125] A. K. Kulkarni, R. F. Penna, R. V. Shcherbakov, J. F. Steiner, R. Narayan, A. Sä Dowski, Y. Zhu, J. E. McClintock, S. W. Davis, and J. C. McKinney. Measuring black hole spin by the continuum-fitting method: effect of deviations from the Novikov-Thorne disc model. *Mon. Not. R. Astron. Soc.* , 414:1183–1194, June 2011.

[126] J.-M. Shi, J. H. Krolik, S. H. Lubow, and J. F. Hawley. Three-dimensional Magnetohydrodynamic Simulations of Circumbinary Accretion Disks: Disk Structures and Angular Momentum Transport. *Astrophys. J.*, 749:118, April 2012.

[127] R. Narayan and I. Yi. Advection-dominated Accretion: Underfed Black Holes and Neutron Stars. *Astrophys. J.*, 452:710–+, October 1995.

[128] A. G. Pacholczyk. *Radio astrophysics. Nonthermal processes in galactic and extragalactic sources.* Series of Books in Astronomy and Astrophysics, San Francisco: Freeman, 1970, 1970.

[129] R. Mahadevan, R. Narayan, and I. Yi. Harmony in Electrons: Cyclotron and Synchrotron Emission by Thermal Electrons in a Magnetic Field. *Astrophys. J.*, 465:327–+, July 1996.